2021

The Development of Structural Hollow Carbon Fibers from a Multifilament Segmented Arc Spinneret: Precursors, Oxidation, and Carbonization

Elizabeth Ashley Morris
University of Kentucky, ashley.morris@uky.edu
Author ORCID Identifier:
https://orcid.org/0000-0002-9711-9512
Digital Object Identifier: https://doi.org/10.13023/etd.2021.427

STUDENT AGREEMENT:

I represent that my thesis or dissertation and abstract are my original work. Proper attribution has been given to all outside sources. I understand that I am solely responsible for obtaining any needed copyright permissions. I have obtained needed written permission statement(s) from the owner(s) of each third-party copyrighted matter to be included in my work, allowing electronic distribution (if such use is not permitted by the fair use doctrine) which will be submitted to UKnowledge as Additional File.

I hereby grant to The University of Kentucky and its agents the irrevocable, non-exclusive, and royalty-free license to archive and make accessible my work in whole or in part in all forms of media, now or hereafter known. I agree that the document mentioned above may be made available immediately for worldwide access unless an embargo applies.

I retain all other ownership rights to the copyright of my work. I also retain the right to use in future works (such as articles or books) all or part of my work. I understand that I am free to register the copyright to my work.

REVIEW, APPROVAL AND ACCEPTANCE

The document mentioned above has been reviewed and accepted by the student's advisor, on behalf of the advisory committee, and by the Director of Graduate Studies (DGS), on behalf of the program; we verify that this is the final, approved version of the student's thesis including all changes required by the advisory committee. The undersigned agree to abide by the statements above.

Elizabeth Ashley Morris, Student

Dr. Rodney Andrews, Major Professor

Dr. Matthew Beck, Director of Graduate Studies

THE DEVELOPMENT OF STRUCTURAL HOLLOW CARBON FIBERS FROM A MULTIFILAMENT SEGMENTED ARC SPINNERET: PRECURSORS, OXIDATION, AND CARBONIZATION

DISSERTATION

A dissertation submitted in partial fulfillment of the
requirements for the degree of Doctor of Philosophy in the
College of Engineering
at the University of Kentucky

By

Elizabeth Ashley Morris

Lexington, Kentucky

Co- Directors: Dr. Rodney Andrews, Professor of Chemical and Materials Engineering and Director of the Center for Applied Energy Research

and Dr. Matthew Weisenberger, Adjunct Assistant Professor of Materials Engineering and Associate Director of the Center for Applied Energy Research

Lexington, Kentucky

2021

https://orcid.org/0000-0002-9711-9512

ABSTRACT OF DISSERTATION

THE DEVELOPMENT OF STRUCTURAL HOLLOW CARBON FIBERS FROM A MULTIFILAMENT SEGMENTED ARC SPINNERET: PRECURSORS, OXIDATION, AND CARBONIZATION

Carbon fiber is an ideal material for structural applications requiring high strength and stiffness and low weight. Yet it has seen only incremental improvements in properties over the last few decades. Carbon fibers remain limited in attaining their theoretical tensile strength and modulus, largely due to defects in their structure, some of which stem from the fiber production process itself. Through the mitigation of defect formation as well as approaches to decrease fiber linear density, it is hypothesized that carbon fiber with enhanced specific properties, including specific strength and modulus, could be produced which would significantly propel its unique capabilities.

One approach to produce high specific property carbon fibers is the development of hollow carbon fibers. The development of hollow carbon fibers for use in structural applications has not been widely explored. The most successful methods to date rely on multicomponent spinning with sacrificial polymers and complex spinneret geometries. A more simplistic, scalable, and economical approach is the use of a segmented arc - shaped spinneret. Traditionally, segmented arc spinnerets have been used for melt or dry spinning hollow fibers. To the author's knowledge, only three references exist describing its use in a solution spinning process for the production of hollow fiber precursors from polyacrylonitrile (PAN). The development of structural hollow carbon fibers from such precursors represents a new technology requiring extensive research in the development of the hollow fiber precursors, as well as their subsequent oxidation and carbonization.

In this work, a method for the multifilament spinning of hollow PAN fibers using a segmented arc spinneret is described. This includes the coagulation, washing, drawing, and spooling of PAN hollow fiber and the effect of each on hollow fiber formation, structure, and properties. In particular, the impact of the coagulation bath composition is explored. Here, the resultant hollow fibers approached the specific tensile performance of traditional solid precursors.

Utilizing these continuous tows of multifilament PAN hollow fibers, oxidation studies were undertaken to determine the capability of the hollow filaments, aided by oxidation from the interior, to oxidize at an increased rate compared to traditional solid fibers. The impact of open interior volume as a percent of the total fiber volume on oxidation was studied. In addition, the mechanisms behind the development of a skin-core structure in the hollow fiber wall are explored and mitigation methods proposed.

The final part of the work focuses on the carbonization of oxidized hollow fibers. The structural parameters of hollow carbon fibers are compared to commercially available solid carbon fibers, with their resulting specific tensile properties compared. A direct comparison is made between hollow fibers and solid fibers with similar outer diameter with regard to their oxidation, carbonization, and resulting morphology and tensile performance. Finally, recommendations are made for continued improvement of the precursor, oxidized, and carbonized hollow filaments to achieve smaller precursor dimensions, faster oxidation rates, less skin-core formation, and higher specific tensile properties.

KEYWORDS: Carbon Fiber, Polyacrylonitrile, Hollow Carbon Fiber, Segmented Arc Spinneret, Solution Spinning

Elizabeth Ashley Morris

11/30/2021

THE DEVELOPMENT OF STRUCTURAL HOLLOW CARBON FIBERS FROM A MULTIFILAMENT SEGMENTED ARC SPINNERET: PRECURSORS, OXIDATION, AND CARBONIZATION

By
Elizabeth Ashley Morris

Dr. Rodney Andrews
Co-Director of Dissertation

Dr. Matthew Weisenberger
Co-Director of Dissertation

Dr. Matthew Beck
Director of Graduate Studies

11/30/2021

To my family and friends, who encourage, love, and support me in each of my pursuits. I am continually blessed by their presence in my life.

ACKNOWLEDGMENTS

I would first like to acknowledge my advisors, Dr. Rodney Andrews and Dr. Matthew Weisenberger, with whom I have worked so closely for over a decade. They have provided me with invaluable insights and encouragement throughout my career. I am incredibly grateful for the continued mentorship provided by Dr. Weisenberger. Matt first hired me as an undergraduate student, trained me as a scientist, and has been in every way the definition of a selfless mentor.

I would further like to acknowledge the carbon materials group at UK's Center for Applied Energy Research. Having worked in the group for so many years, I have been blessed to collaborate daily with a multitude of brilliant and humorous minds. My group members and the research environment we have cultivated under Matt's leadership make it a pleasure to come to work every day.

Last but certainly not least, none of this would have been possible without the unwavering love and support provided by my family and friends. My husband, Jad, has always supported my wildest ideas, one of which was to write and defend this dissertation while pregnant with our first child. My mother, Kim, and my siblings, Tyler and Anna, are continual inspirations to me. I am so thankful for my family's fierce love and belief in me even in times when I may have doubted myself. They have made me the person I am today.

Financial support for this work was provided by the Department of Energy Office of Energy Efficiency and Renewable Energy Hydrogen and Fuel Cell Technologies Office (award number DE-EE0008095).

TABLE OF CONTENTS

LIST OF TABLES

LIST OF FIGURES

CHAPTER 1. INTRODUCTION

1.1 Overview of carbon fibers

Carbon is a unique element. When asked why she chose to study carbon, Professor Mildred S. Dresselhaus (lovingly dubbed the Queen of Carbon) remarked that, in the 1960s, carbon was relatively unpopular and a difficult study. Today, carbon is anything but unpopular. Carbon has unique abilities to form multiple bonds, not only with itself, but with other atoms as well. It can form chains, branches, and rings, resulting in millions of complex molecular possibilities. Amorphous carbons are common (Figure 1.1b), but carbon is also able to form a number of distinct crystalline forms, or allotropes. More exotic allotropes such as fullerenes and carbon nanotubes have recently been discovered (Figure 1.1c and d), while the more commonly known allotropes of carbon are diamond and graphite (Figure 1.1a and e). When oriented parallel to one another, graphitic crystallites form the basis for carbon fiber (CF), an extremely strong and lightweight material. Carbon fibers are commonly combined with resins to produce carbon fiber reinforced polymer (CFRP) composites and have become a highly desired material for structural applications requiring high strength, stiffness, and low weight. Carbon fibers are currently used in composites for a variety of applications in the aerospace, wind energy, automotive, and sporting goods industries.

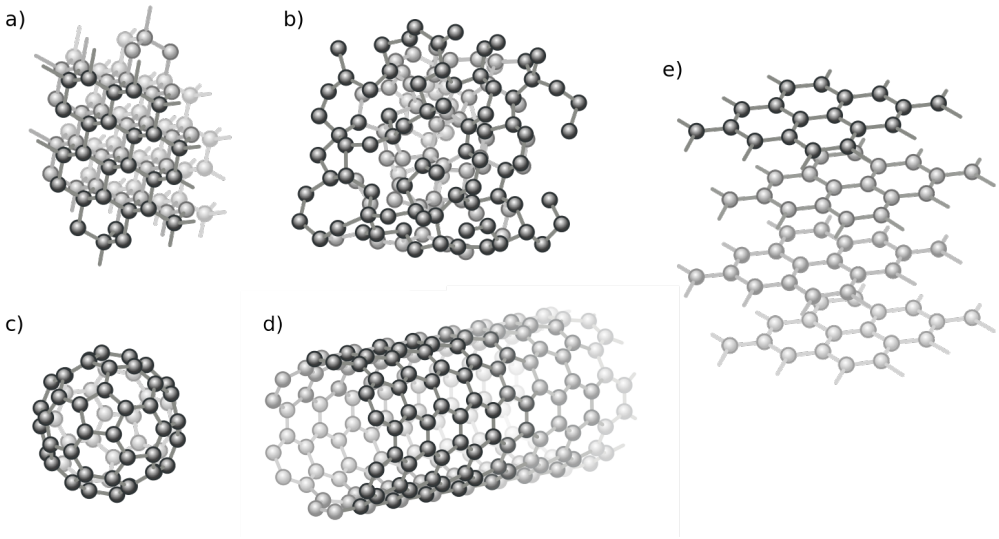

Figure 1.1. Allotropes of carbon, including a) diamond, b) amorphous carbon which has nonregular recurring bonding structures of both graphite and diamond, c) fullerene, a C60 bucky-ball, d) single walled carbon nanotube and e) graphite. Adapted from [1]. Licensed under CC BY-SA 4.0.

1.1.1 Carbon fiber precursors

Carbon fibers are traditionally manufactured from polyacrylonitrile (PAN), pitch or rayon precursor fibers. However, PAN-based CFs dominate the market due to their combined strength and modulus properties [2]. The development of high tensile strength and modulus CF is directly dependent on the quality of the precursor fiber [3-6]. High quality PAN precursors are known to have fewer voids, smaller diameter (approximately 10-12 μm), low comonomer content, >50% carbon yield, and high tensile strength and modulus [5, 7-9]. Research and development of PAN precursor fiber requires extensive experimentation to determine their process-structure-property relationships. This is not arbitrary and involves the cooperation of hundreds of dependent and independent variables, each of which impacts the resultant fiber.

To produce high quality PAN precursors, solution spinning is the method of choice. Alternative production methods have been studied, such as electrospinning [10] or melt spinning of PAN [11], however, the resulting carbon fibers lack the properties required to

produce CF for structural applications. As a result, solution spinning is widely used to produce CF precursors. Solution spinning relies on the solubility of the PAN polymer in a solvent. This spinning solution, or "dope", is then extruded through a spinneret containing numerous capillaries to produce a filament tow. The nascent fibers enter a coagulation bath, typically containing a mixture of solvent and non-solvent (often water). Coagulation of the forming filaments occurs due to solvent diffusing out of the polymer solution and non-solvent diffusing into the forming fiber [3, 9, 12], leading to precipitation of the polymer into fibrillar form [13].

There are generally two types of solution spinning: wet-jet and dry-jet (or air gap) solution spinning. During wet-jet spinning, the spinneret is partially submerged in the coagulation bath, so that the exiting filaments immediately enter the coagulation bath liquid. On the contrary, during air gap spinning, the filaments exit the spinneret and pass through an air gap measuring several millimeters before entering the coagulation bath, as shown in Figure 1.2. Utilizing air gap spinning allows for increased draw ratio on the filaments within the air gap and can result in better molecular alignment compared to wet-jet spinning. The air gap spun filaments traditionally have a smoother surface compared to wet-jet spun filaments, as a small amount of solvent evaporates from the filament surface as they pass through the air gap. This smoother surface has been suggested to produce higher tensile strength fibers [14]. In addition, air gap spinning allows for faster line speeds compared to wet jet spinning stemming from the drawdown filaments experience in the air gap. Despite these advantages, air gap spinning requires precise rheological formulation of the spinning solution to withstand tensile forces within the air gap and filament failure often results in cascading wipeout of the remaining filaments. Air gap solution spinning is therefore a highly desired method for the production of high-quality precursors but requires more precise control of spinning variables to prevent failure.

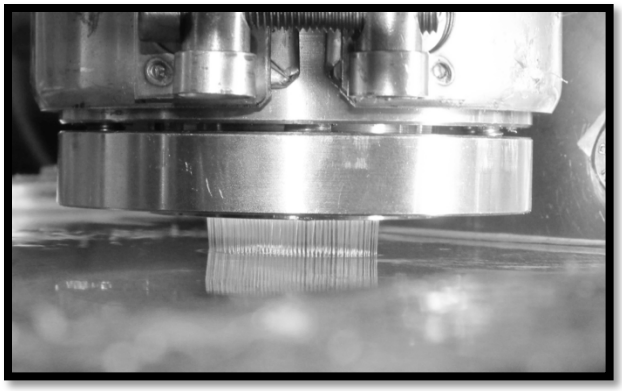

Figure 1.2. Multi-filament air gap (5 mm gap) solution spinning of PAN polymer solution into a coagulation bath at the University of Kentucky Center for Applied Energy Research. Reprinted with permission from [15]. Copyright 2014 American Chemical Society.

As stated previously, coagulation of the forming filaments exiting the spinneret is dependent upon solvent diffusing out of the polymer solution and non-solvent diffusing in. Control over the rate of coagulation is vital to produce round precursor fibers. It has been shown that precursor fibers with non-round cross-section cannot withstand a high draw ratio during subsequent spinning, stabilization, and carbonization due to stress concentration [16]. Circular fibers, on the other hand, experience a homogeneous Poisson's contraction (within the elastic strain range) when exposed to tensile forces. Control over the rate of coagulation is largely determined by the composition and temperature of the coagulation bath. When the flux of solvent outward is less than the non-solvent inward flux, the filament swells and a circular cross-section can be expected. This swelling occurs at high coagulation bath temperatures and high solvent content in the coagulating bath [17]. For this reason, cross sections are characteristically round at 50 °C or above. However, high bath temperatures have also been attributed to an increase in void content and subsequent decrease in fiber density, resulting in poor fiber properties [18-20] and therefore lower bath temperatures are preferred. In contrast, at lower solvent concentrations, the outward diffusion of solvent dominates, but the perimeter of the filament in contact with non-solvent is solidified early, resulting in a thin polymer cuticle exterior. As outward diffusion of solvent continues, the filament collapses, resulting in non-round (often bean-shaped) cross-sectional shape [16, 20, 21]. As a result, higher coagulation bath

compositions (>70 wt.% but <80 wt.% solvent/non-solvent) and typical bath temperatures (~20 °C) have been found to produce fibers that are more circular in cross section, smaller in diameter, higher in density, higher in orientation, and higher in tensile strength and modulus [22]. It is also important to note that the cross sectional shape of the precursor fiber is fixed during coagulation [4], and therefore coagulated fibers are often carefully studied to ensure the target cross section is achieved prior to continuation of the spinning process.

Following coagulation, PAN precursor filaments proceed through washing and stretching/drawing baths, with spin finishes added. Finally, the precursor fiber experiences a drying, collapsing (of porosity), and heat setting process prior to final collection on a traversing takeup roller. Fiber washing (typically with water) following coagulation is of particular importance to remove residual solvent from within the fiber porosity. Residual solvent leads to a swelling effect during drying operations and creates voids within the fiber, compromising mechanical properties [23] and acts as an impurity during thermal treatment, contributing to discontinuity in ladder formation [24], imperfect crystalline structure [25], and fiber breakage. A slow washing procedure is preferred for producing filaments with dense structures with negligible void content [23, 26], with a target residual solvent content of < 0.5 wt.% [24].

Once the fiber has been properly washed for removal of residual solvent, the fiber is then stretched to increase molecular alignment and reduce fiber diameter. The stretching process is vital for ordering the fiber structure and enhancing the fiber properties. To enable stretching, the fiber is heated above the glass transition temperature (T_g), and drawn between godets of varying linear speeds, often using hot water, steam, and/or oil as the heating medium [27]. Stretching above the T_g not only orients the fibrils in the direction of the fiber axis but also stretches the individual fibrils [19]. In addition, as both the amorphous and crystalline regions are oriented in the direction of the fiber axis, pores within the fiber are elongated. When high draw is applied above the glass transition temperature [28], molecular chains slip, resulting in desirable pore collapse [29]. As a result, stretching reduces the number of pores within the fiber through pore collapse,

increasing molecular alignment, and reduces fiber diameter, all of which are necessary to produce high strength, high modulus CF.

During the drawing process, spin finishes are often applied. A primary spin finish can be applied either prior to or following the first drawing step. This primary finish typically consists of a silicone emulsion whose purpose is to decrease friction between the fiber strands and facilitate subsequent drawing. In addition, this finish remains on the precursor fiber through oxidation and aids in preventing the fusion of fiber strands while remaining permeable to oxygen. Following the second drawing step, a secondary spin finish can be applied which is typically an alkyl ester emulsion or ethylene oxide/propylene oxide (EO/PO) copolymer. This secondary finish imparts cohesiveness to the precursor fiber strands, increasing handleability. Overall, spin finishes facilitate fiber processing in the subsequent collapse and drying steps [30]. The fiber is finally dried and spooled for further thermal processing.

1.1.2 Oxidative stabilization

Following spinning, the precursor fiber is subjected to specific controlled temperature, time, and strain pathways to produce a final carbon fiber. Initial heat treatments are necessary to render the fiber thermally infusible, or stable, referred to as stabilization. Stabilization in air, also known as oxidative stabilization or oxidation, has been shown to be a prerequisite for the production of high performance CF [31] and must be carefully controlled. Once thermally stable, the fiber is carbonized to produce the final carbon fiber. During stabilization, which typically occurs between 200 and 300 °C in an air atmosphere, three major reactions occur: cyclization, dehydrogenation, and oxidation. The general chemistry for PAN oxidative stabilization is presented in Figure 1.3, where cyclization and dehydrogenation occur, followed by a proposed oxidized PAN structure.

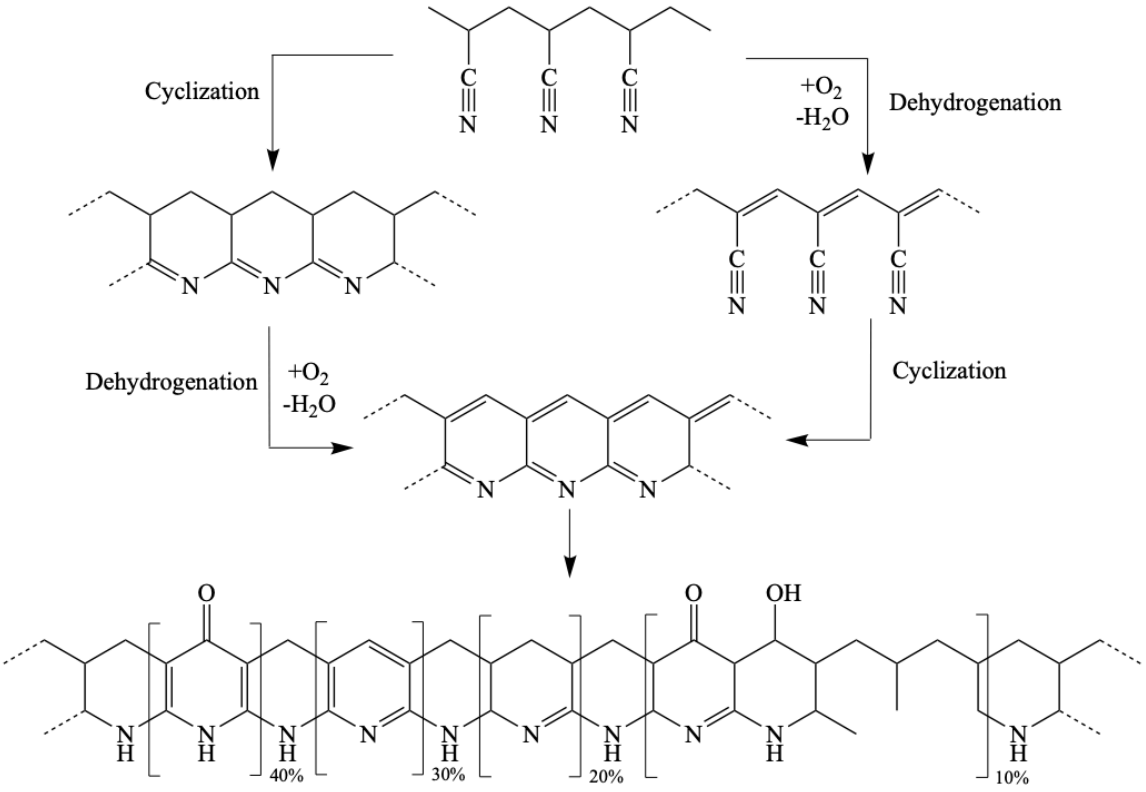

Figure 1.3. The general chemistry of PAN stabilization in air. Adapted from [32].

In general, cyclization is responsible for the conversion of the PAN chain to a ladder polymer during heat treatment, converting C≡N nitrile bonds to C=N bonds, and providing positions at which the oxidation reaction can occur [33-35]. Cyclization alone, however, cannot completely stabilize the filaments. Cyclized segments are not aromatic because in each ring several carbon remain as sp^3 atoms bearing hydrogens. Thus, bond energies in the ring are lower and chain scission is more likely [36]. Dehydrogenation and oxidation must also occur to stabilize the filaments, both of which require the presence of oxygen. Oxygen is essential to stabilizing the structure for further thermal conversion [36-40]. In fact, fibers stabilized in N_2 alone often do not survive the carbonization process. In the presence of oxygen, dehydrogenation is responsible for the elimination hydrogen from the ladder structure in the form of H_2O. This results in the formation of C=C bonds and is a vital step in the creation of stabilized structures [41-44].

Cyclization and dehydrogenation are responsible for the formation of the polycyclic aromatic structure shown in Figure 1.3, which again would not be possible in the absence

of oxygen [45]. Further oxidation results in the incorporation of oxygen into the structure. The chemical structure of oxidized PAN fiber has been studied for numerous years, and many chemical structures for oxidized PAN fiber have been suggested. However, the exact mechanism responsible to produce high-quality CF remains up for debate. The presence of oxygen in properly oxidized and stabilized PAN has been suggested to appear in the form of carbonyl groups [46], imine groups donating lone pair electrons to oxygen atoms [47], bridging ether type groups [48], or a mix of hydroxyl and carbonyl groups [32], similar to that shown in the last structure of Figure 1.3. Each of these structures are presented in Figure 1.4.

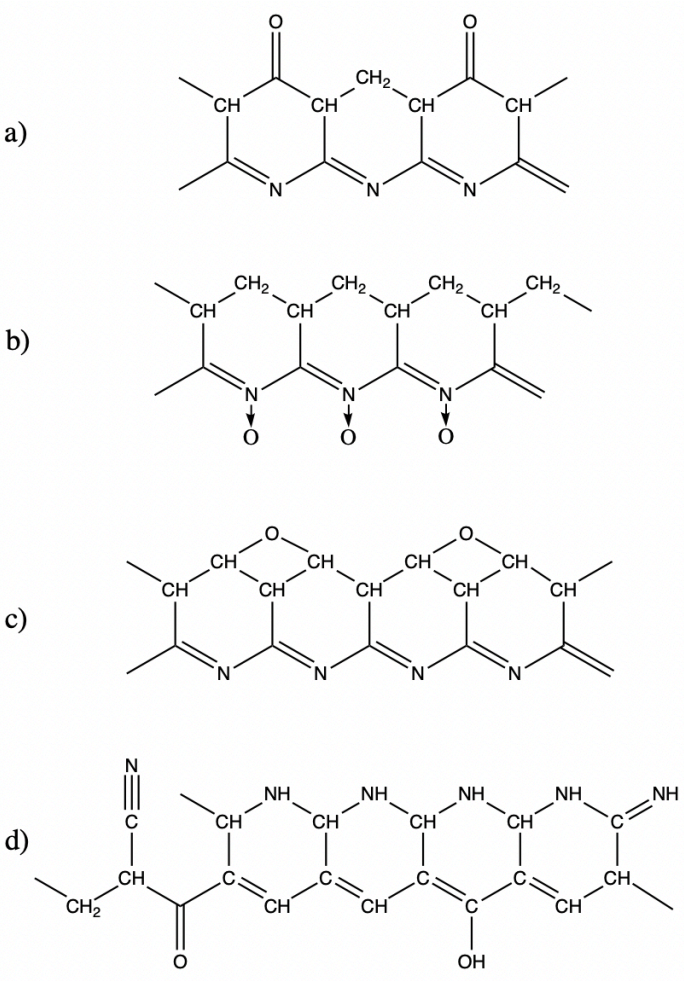

Figure 1.4. Proposed structures of oxidized PAN. (a) carbonyl groups; (b) imine groups donating lone pair electrons to oxygen atoms; (c) bridging ether type groups; (d) a mix of hydroxyl and carbonyl groups. Adapted from [32] with permission from Elsevier.

Researchers have found that when oxygen in the oxidized fiber is present as hydroxyl and carbonyl groups, the chain chemistry of the resulting oxidized molecule consists of stiff, planar, cyclized rings connected by relatively mobile linear segments [36], as shown in Figure 1.4d. When this structure is heated during the early stages of carbonization, the linear segments twist to allow cyclized sequences to become planar with other neighboring cyclized sequences, laying the foundation for the graphitic structure of the resulting CF. The driving force for this alignment has been proposed to be a condensation reaction between the hydroxyl groups, as water has been found in gases evolved during early carbonization [36, 49]. This suggests an optimal oxygen content should be present in the stabilized fibers for these condensation reactions to occur and the graphitic structure to form. In fact, multiple references report the desired oxygen level in fully stabilized fiber ranges from 10-12 wt.% oxygen [2, 31, 50-53].

1.1.3 Carbonization

Carbonization of oxidized PAN fiber is typically performed under an inert atmosphere by heating the fiber to temperatures between 1200 and 1800 °C. The goal of carbonization is the removal of non-carbon elements to produce a filament containing >95% carbon. In industrial practice, carbonization can be completed in two steps, low temperature (LT) and high temperature (HT) carbonization. During LT carbonization, the oxidatively stabilized fiber is heated gradually through several zones to approximately 1000 °C. Multiple gases are evolved, including HCN, CO_2, H_2O, CO, NH_3, N_2, and H_2, as shown in Table 1.1, and crosslinking occurs. During HT carbonization, final non-carbon elements are removed and the final structure is set. A maximum carbonization temperature of 1500 °C has been found to be beneficial to produce high tensile strength and modulus fibers. For example, a turbostratic carbon phase is formed with temperature up to 1600 °C, which has been found to be responsible for high tensile strength [54]. In addition, tensile strength is determined by flaws in the volume and on the fiber surface up to 1500 °C and the relationship between Young's modulus and tensile strength is linear up to that point [55], with a maximum tensile strength obtained at about 1500 °C [56-58]. For the purposes of this study, carbonization will take place at or below 1500 °C.

Table 1.1. Carbonization products of oxidized PAN fiber. Adapted with permission of Taylor & Francis Group LLC, from [2]; permission conveyed through Copyright Clearance Center, Inc.

Temperature (°C)	Observation	Interpretation
220	HCN evolved and O_2 chemically bonded	Ladder polymer formation and oxidation of polymer
260	Little change. No modulus increase	No chain scission
300	Large CO_2 and H_2O evoluation, also CO, HCN and some nitriles. No modulus increase	CO_2 from -COOH groups in oxidized polymer
400	CO_2, H_2O, CO, HCN and NH_3 evolved. Small evolution of C3 hydrocarbons and nitriles. Modulus increase	No cross-linking
500	Increased H_2 evolution. Some NH_3 and HCN evolved. Modulus increase.	Cross-linking by intramlolecular H_2O elimination
600	Reduced H_2 evolution. HCN and trace N_2	Cross-linking by dehydrogenation
700	N_2, HCN and H_2 evolution. Modulus increase.	Cross-linking by dehydrogenation and evolution of N_2
800	Large increase in N_2, H_2 and HCN still evolved. Modulus increase.	Cross-linking by evolution of N_2
900	Maximum evolution of N_2, some H_2, traces HCN. Modulus increase.	Cross-linking by N_2 elimination
1000	N_2 evolution decreases to about the same as at 800 °C. Trace H_2 evolved. Modulus increase.	Cross-linking by N_2 elimination

Notes: Fiber yield 53.6%, 5.0% nitrogen content

1.1.4 Mechanical properties and morphology

Carbon fiber (CF) is a highly desired material for structural applications requiring high strength, stiffness, and low weight. Typical PAN precursor and PAN-derived CF tensile properties are shown in Table 1.2. The PAN-based CF values referenced are based on Toray's T700S CF, which is a high strength, standard modulus fiber widely used in the CF industry due to its outstanding processability. One factor limiting the widespread use of CF and CF composites is the high cost associated with its production, particularly when compared to more traditional materials such as glass fiber and metals. However, the specific properties (material property per unit density) of CF are the driving force behind its use despite its higher initial cost. For example, the specific strengths of common metals (copper, 304 stainless steel, and aluminum 7075) are shown in Figure 1.5 and are well below 0.5 N/tex (equivalent units of GPa/g/cm^3). However, the specific strengths of common CF types (T700S, IM7, and T1000G) are well above 2.5 N/tex. The specific properties for PAN precursor and PAN-based CF are listed in Table 1.3. Carbon fiber is

chosen to supplant aluminum and steel, particularly in weight critical applications, because of this high *specific* strength and modulus. Glass fibers are also often used in composites, similarly to CF, and are a cheaper alternative to CF. However, as shown in Figure 1.5, E-glass fiber specific strength remains much lower than T700S CF, at approximately 1.3 N/tex. Dyneema UHMWPE is of similar specific modulus to T700S but with higher specific strength (3.7 N/tex). However, UHMWPE cannot be used for extended periods above 80-100 °C, which limits its applications in high performance composites. Also listed in Figure 1.5 is another CF type, Toray T1100G, which has the highest specific properties of any material listed. However, these impressively high specific properties come at a cost, with T1100G costing 10-20x as much as T700S for only a 43% and 30% increase in specific strength and modulus, respectively [59]. It is for this reason that T700S is the more commonly utilized CF. The data presented here demonstrates the incredible capabilities of CF in providing high performance at low weight. Further increases in CF specific properties would propel its unique capabilities, particularly if those improvements could be made without increasing the cost of production. Unfortunately, the CF industry has seen only incremental improvements in CF properties over the last few decades, and a major breakthrough is needed.

Table 1.2. Typical tensile properties of PAN precursor and PAN-derived CF. The PAN-based CF reference is T700S [60].

	Diameter (μm)	Density (g/cc)	Tensile Strength (MPa)	Tensile Modulus (GPa)	Strain to Break (%)
PAN precursor	12 to 14	1.18	700	12	8 to 10
PAN-based CF	7	1.8	4900	230	2.1

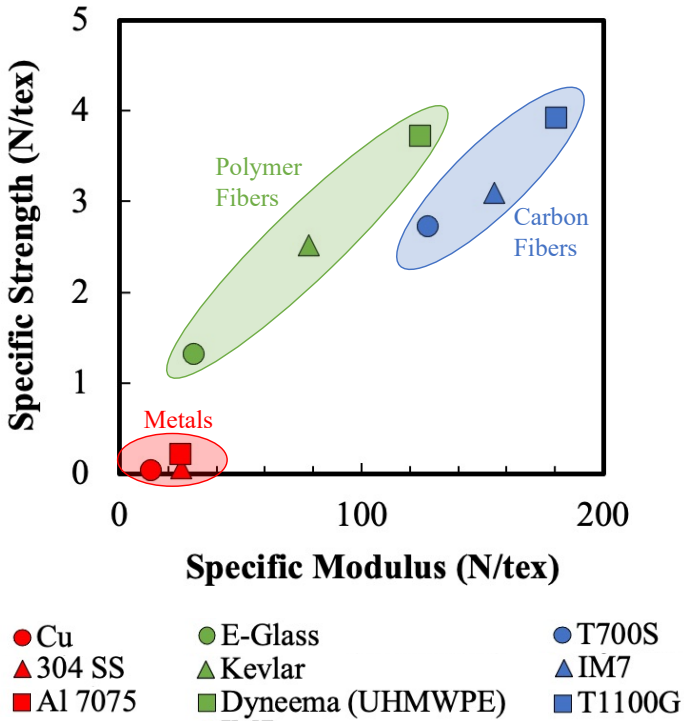

Figure 1.5. Specific strength and modulus of common structural materials.

Table 1.3. Specific tensile strength and tensile modulus of PAN precursor and PAN-derived CF. The PAN-based CF reference is T700S [60].

	Specific Tensile Strength (N/tex)	Specific Tensile Modulus (N/tex)
PAN precursor	593	10
PAN-based CF	2722	128

Numerous factors must be controlled throughout the production process to produce CF with high specific properties such as T700S and T1100G. Careful control of the morphology development must be executed to prevent the introduction of defects to the fiber which are detrimental to CF tensile performance. In general, the fine structure of CF consists of basic structural units (BSU) of turbostratic (disordered) planes [61], with disordered regions interspersed with ordered zones [2]. While the distance between perfect graphite planes is 0.3345 nm (d_{002}), the distance between turbostratic planes in CF is typically > 0.34 nm [62] and these planes are formed by ribbons of sp^2 carbon which form fibrils and microfibrils oriented along the fiber axis [63]. Several models have been developed to illustrate the CF structure, with the microcrystalline structures incorporating

packing, orientation, extent of long-range order, interweaving, folding, imperfect stacking, voids, twisting and dislocations [63]. A few models are shown in Figure 1.6. In Figure 1.6a, a CF ribbon is depicted, which is believed to be a columnar arrangement of misoriented turbostratic graphite crystallites. There is slight misorientation between crystals along the fiber axis, creating voids [64]. In high modulus fibers, surface crystallites are large, well-perfected, and templated parallel to the fiber surface, becoming more disordered to the core of the fiber, as shown in Figure 1.6b.

Multiple defects are present, including pockets of short-range materials, voids, and cracks. In Figure 1.6c, a magnified view of the skin and core region of a CF are illustrated, where (A) is the skin and consists of ordered BSU aligned with the fiber axis and (B) is the core, consisting of disordered BSU. The model also presents other defects, including (C) hairpin defects and (D) wedge disclinations.

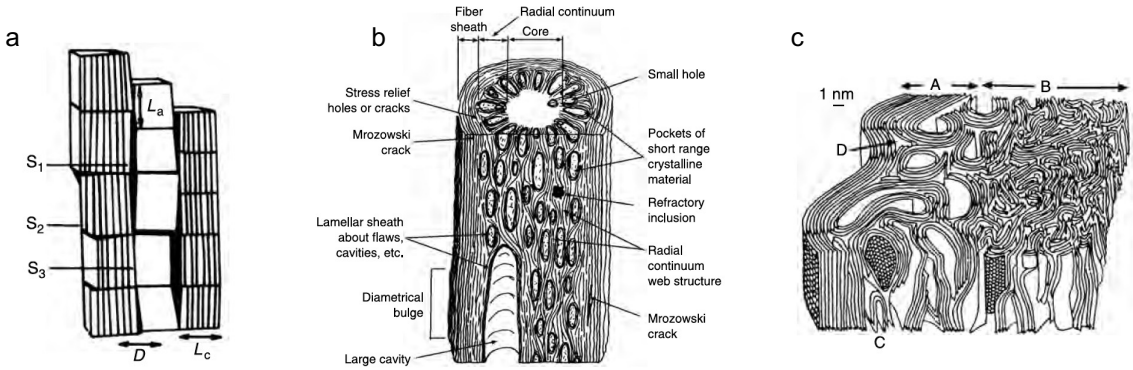

Figure 1.6. Carbon fiber models. (a) Idealized structure of CF. S_1, void; S_2, subgrain twist boundary; S_3, intercrystalline boundary. L_c and L_a are thickness and diameter of carbon layer stacks and D is the distance between them. Republished with permission of IOP Publishing, Ltd, from [64]; permission conveyed through Copyright Clearance Center, Inc. (b) A three dimensional model for a PAN-based CF. Reprinted from [63] with permission from Elsevier. (c) Microstructure schematic of PAN-based CF basic structural units combined into microdomains, where (A) is the skin region, (B) is the core region, (C) is a hairpin defect, and (D) is a wedge disclination. Reprinted from [65] by permission from Springer.

The microcrystalline structures and defects presented previously and in Figure 1.6 are artifacts of the CF development process, stemming from precursor spinning, oxidative stabilization, and/or carbonization. Defects within the structure are detrimental to both the

precursor and CF tensile properties. The tensile strength tends to be greatly impacted by flaws in the long-range order. The probability of flaw occurrence can be reduced by reducing the fiber diameter, which results in a corresponding increase in tensile strength [2]. This can be explained using the Griffith fracture theory, which states that a single molecular chain would possess the highest tensile strength because such a structure could tolerate no defects [66], ultimately resulting in fewer defects per unit length. The tensile elastic modulus, on the other hand, is largely dependent on the orientation of the fibrils with respect to the fiber axis. Given that the core of the CF consists of disordered structures, and these disordered structures can give rise to voids, the core of the fiber has been found to be detrimental to the overall properties of the CF, which will be discussed further.

1.1.4.1 Skin-core structure

The skin-core structure of the fiber is known to be the result of insufficient oxidative stabilization of the fiber core. As stated previously, oxygen incorporation into the cyclized PAN ladder structure is pertinent to the later formation of graphitic structures during carbonization [36] and an optimum oxygen content of 10-12 wt.% is desired in the oxidized fiber [2, 31, 50-53]. Atmospheric oxygen must diffuse from the exterior of the fiber toward the interior and react with the stabilizing chains for oxygen to reach the desired levels during oxidative stabilization.

Warner et al. described two different limiting conditions during stabilization: diffusion-limited and reaction-limited [67]. In the reaction limited case, a thin stabilized skin forms at the fiber surface, but once oxygen permeates the skin, it is free to diffuse throughout the unreacted regions, resulting in a homogeneous fiber cross section. On the contrary, in the diffusion-limited scenario, a two-zone morphology, or skin-core structure, forms due to an increasingly impermeable oxidized outer layer, which hinders further oxygen diffusion. Under this condition, the increase in oxygen weight percent was found to vary with the square root of time. The diffusion coefficient of oxygen through PAN was estimated to be approximately 300% higher compared to the diffusion coefficient of oxygen through an oxidized PAN layer [67]. An initial assumption could be made that a reaction-limited stabilization process, which is favored by low temperatures and tends to produce homogeneous CF, would be preferred. However, Yu et al. found that at low

stabilization temperatures (210 °C, for example), the rate of oxygen uptake is very low at the beginning of the heat treatment, and decreases slowly [68]. Therefore, at low temperatures, the rate of oxygen uptake will tend toward zero with time. As a result, obtaining stabilized fibers with the recommended 10-12 wt.% oxygen content to produce high-quality CF is not possible. Therefore, stabilization must take place at higher temperatures (250 °C, for example) to achieve an initial high rate of oxygen uptake and, as a result, oxidation will occur via a diffusion-limited process and often results in a skin-core structure observed in current commercially available CF such as the T700S CF shown in Figure 1.7.

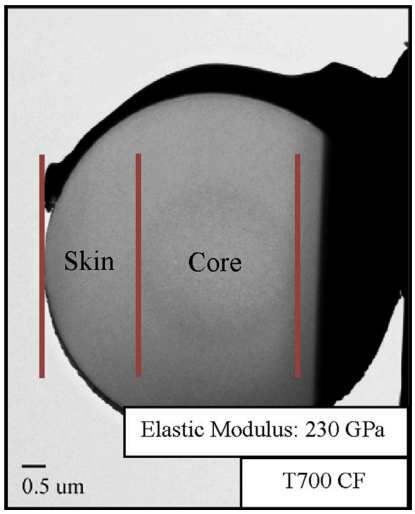

Figure 1.7. Prominent skin-core structure of T700S CF. Reprinted with permission from [69].

This inhomogeneous oxygen diffusion results in poor crosslinking, as would be expected in anaerobic stabilization, which hinders graphite sheet formation [70]. As a result, the core of the stabilized and resulting CF is less dense than the skin. Nunna et al. provided possible chemical structures highlighting the differences between the skin and core in oxidized PAN fiber. It is best to keep in mind, however, that numerous chemical structures have been hypothesized, and each is highly dependent upon starting polymer (particularly types and amounts of comonomers), fiber morphology and dimension, and time-temperature-strain pathways during oxidative stabilization. Despite these inherent differences, chemical structures provided by other authors, such as Nunna et al., can

provide some general insights into possible mechanisms responsible for structural differences in the fiber cross section, which ultimately impact the final CF properties [71].

Shown in Figure 1.8, Nunna et al. proposed that the cyclized ladder structures present in the fiber skin are attacked by oxygen, forming carbonyl and hydroxyl groups [72]. Carbonyl groups are not generated until approximately 200 °C and their concentrations increase gradually with temperature [40]. According to Figure 1.3, properly oxidized fiber contains more carbonyl groups than hydroxyl groups, however, the opposite has also been found, where adequately oxidized fiber possessed a small concentration of carbonyl groups with significant hydroxyl formation [33]. In general, however, Nunna et al. proposed that the presence of the carbonyl and carboxyl groups in the backbone promote cross-linking by elimination of H_2O. This crosslinking created conjugated planar structures in the skin and served as the basis for the development of pseudo graphitic structures in later stages of the carbonization process. The amount of crosslinking occurring during oxidative stabilization will, again, be highly dependent on the system under study. Some authors have noted crosslinking does not significantly occur until 400 °C, which is beyond typical stabilization temperatures [2], whereas Nunna et al. are discussing crosslinking at 240 °C [72]. Oxygen remaining in the chemical structure may be indicative of the amount of crosslinking (or lack thereof) that has occurred, as the crosslinking reaction is known to liberate oxygen in the form of H_2O.

Nunna et al. proposed a corresponding chemical structure for the fiber core. Here, heat transferred from the surface of the fibers triggers partial dehydrogenation in the core [72]. In addition, cyclization is known to occur to a higher extent in the core of the fiber than the skin, attributed to heat accumulation in the core following the onset of the exothermic cyclization and oxidation reactions in the skin [41, 72-74]. The promotion of core cyclization leads to a disoriented ladder polymer structure in the core [75], as C≡N are converted not only to C=N bonds, but also to other chemical species without double bonds [41]. Chemical structures such a C – NH – C are likely candidates [76].

As atmospheric oxygen diffuses to the core over time, the initiation of oxidative dehydrogenation reactions occurs, resulting in the evolution of two possible core structures. Bridging oxygen atoms are proposed to occur where partial dehydrogenation is dominant.

In the second possible structure, carboxyl and carbonyl groups form. However, due to the presence of the bridging oxygen atoms, the cross linking mechanism will not be as efficient in the skin of the fiber [72]. Evidence for this inefficiency was supported by the presence of higher concentrations of C=O, CH functional groups, and sp^3 hybridized carbon atoms in the core [72].

The structures presented by Nunna et al. and others describe possible mechanisms behind the formation of skin-core differences in oxidative PAN fiber. While the precise reactions are difficult to pinpoint despite extensive fiber analysis, it is well known that differences in oxidized PAN fiber chemical structures have significant impacts on the tensile properties of the resulting CF and any such differences should be minimized to attain maximum tensile properties [77-83].

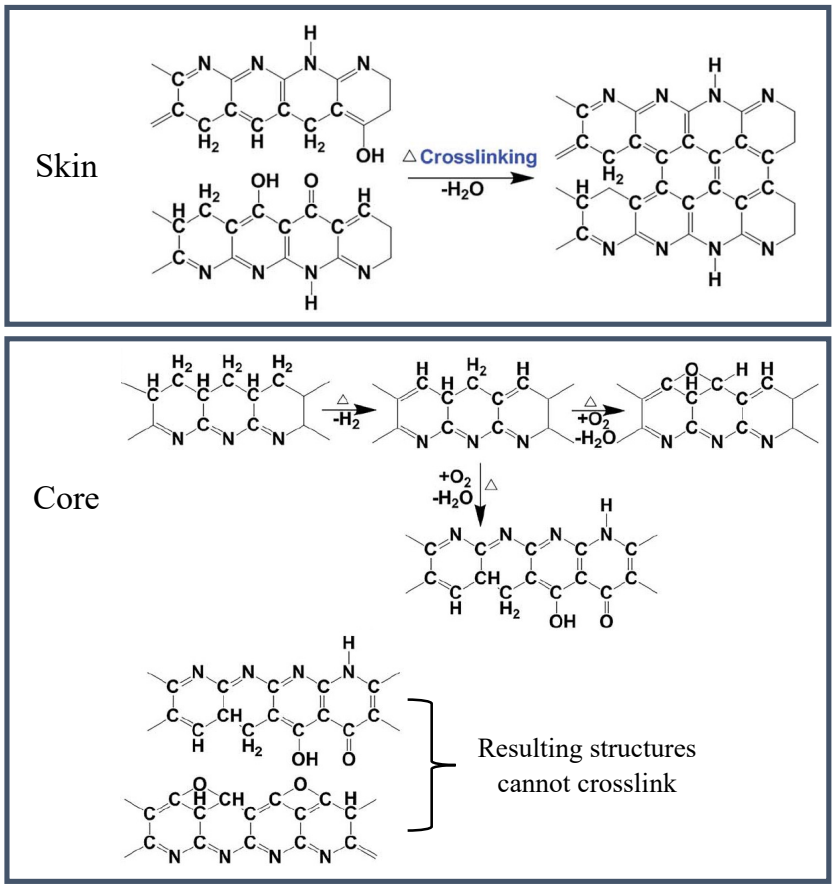

Figure 1.8. Proposed changes during the thermal stabilization of PAN fibers, indicating differences in crosslinking and reaction mechanisms between the skin and core of the fibers. Reprinted with permission from the Royal Society of Chemistry, from [72]; permission conveyed through Copyright Clearance Center, Inc.

1.1.4.2 Fiber strength impact

The presence of a skin-core structure in CF has been shown to be non-ideal in the production of CF. The tensile strength of CF is known to be negatively impacted by the presence of flaws such as foreign particles, voids, or other imperfections (as shown in Figure 1.6b) [58, 84], which result in stress concentrations that ultimately lead to fiber failure. Interestingly, variations in stress concentration between the skin and core of a CF have been shown as well. Kobayashi et al. [77] utilized a synchrotron generated X-ray beam measuring 1 μm in diameter to determine crystalline strain via peak shift of X-ray diffraction profiles, as well as Raman spectroscopy, to develop stress concentration models

for the skin and core of a CF held under varying tensile stresses. The model indicated that the skin carried 10 times the stress compared to the core. Given that stress concentration occurs preferentially on the skin, mitigation of surface flaws has been found to be highly impactful for increasing fiber tensile strength [78, 79]. Reducing or eliminating the skin-core structure, which would allow for homogeneous stress distribution along the fiber cross section, will lead to improved tensile properties as well [80, 81]. However, flaws alone may not explain CF tensile strength. Loidl et al. [85] hypothesized that it is the arrangement of the crystallites and their interlinking responsible for failure (as has been suggested previously [86]). Similarly, it has been found that for fiber carbonized above 1250 °C, defects other than surface flaws govern the strength, which may include shearing inside the crystallites causing stress concentrations [84]. Therefore, mitigation of the skin-core effect, fiber defects and preferential crystallite arrangement and size [87] are all pivotal for the production of high tensile strength CF.

1.1.4.3 Fiber modulus impact

The skin-core structure negatively impacts not only the tensile strength, but also the tensile modulus. The basal plane preferred-axial orientation in the core is known to be lower than the skin [81, 88]. Further, Gu et al. [82] found that the external skin of a T700 CF was of higher storage modulus than the core, as shown in Figure 1.9a and b, by approximately 50%. Additionally, Liu et al. also found the storage modulus to differ between the skin and core of a PAN based CF, in this case by approximately 18% using nanoscale dynamic mechanical analysis [83]. Additionally, Chen et al. measured the radial distribution of tensile modulus for several commercial CF by measuring the electrical conductivity following varying levels of plasma etching [14], shown in Figure 1.9c. Their results also indicated a drop in modulus from skin to core for T700S, as well as other commercially available fibers. The higher modulus skin of the CF has been attributed to an increased degree of graphitization on the surface of the CF compared to the core [81]. In order to reduce the impact of a skin-core structure, reduction in precursor fiber diameter (and therefore reduction in the oxygen characteristic diffusion length during oxidation) has been shown to reduce and even eliminate the skin-core structure [70] and to greatly increase the tensile Young's modulus of the resulting carbon fiber [69]. However, Kong et al. found

that the skin-core structure did not disappear until a precursor diameter of 6.1 mm, which produced CF diameters of 4 mm [70]. Morris et al. found similar [69]. Not only are such small diameter filaments difficult to produce, but CF of such small diameter lie on the respirable limit of concern of 3 mm [89] and exhibit poor compressive properties in composites, being particularly prone to micro-buckling [90]. Therefore, they not commercially produced. However, the results presented by Kong point to the importance of a reduced oxygen characteristic diffusion length in mitigating the development of a skin-core structure and encouraging the formation of homogeneous, mechanically robust fibers.

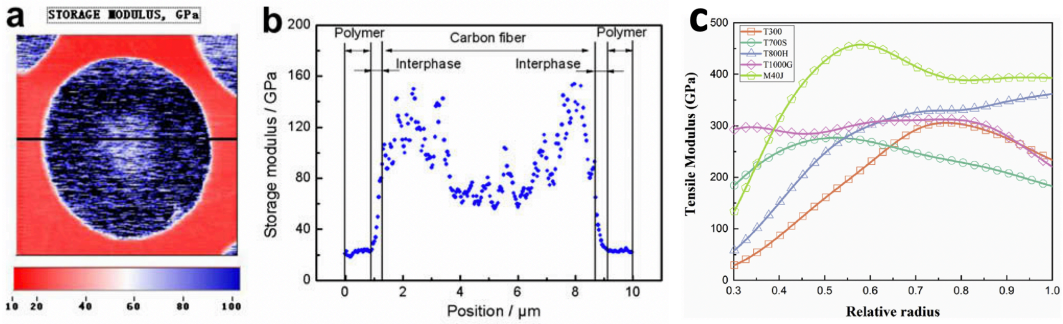

Figure 1.9. (a) A storage modulus map of a T700 carbon fiber and (b) a line scan showing a storage modulus gradient between the skin and the core of the fiber. Reprinted from [82] with permission from Elsevier. (c) Radius distribution of tensile modulus for several commercial CF. Reprinted from [14] with permission from Elsevier.

1.2 References

1. Sivek, J. *Creative commons carbon allotropes*. 2015 [cited 2021; CC BY-SA 4.0]. Available from: https://commons.wikimedia.org/wiki/File:Carbon_allotropes.svg.
2. Morgan, P., *Carbon fibers and their composites*. 2005, Boca Raton, LA: Taylor & Francis Group.
3. Masson, J.C., *Acrylic Fiber Technology and Applications.* 1995.
4. Gong-qiu Peng, Y.-f.W., Yong-gang Yang, and Lang Liu, *A Novel Method for Investigating the Structural Uniformity of Polyacrylonitrile Nascent Fibers.* International Journal of Polymer Anal. Charact., 2008. **13**: p. 369-375.
5. M.A. Rahman, A.F.I., A. Mustafa, B.C. Ng, H. Hasbullah, M.S.A. Rahaman and M.S. Abdullah, *The Effect of Coagulation Bath Temperature on the Mechanical Properties of PAN-based Carbon Fiber.* p. 169-179.
6. R.B. Mathur, O.P.B., and J. Mittal, *Advances in the Development of High-Performance Carbon Fibres from PAN Precursor.* Composites Science and Technology, 1993. **51**: p. 223-230.
7. S.J. Law, S.K.M., *Investigation of Wet-Spun Acrylic Fiber Morphology by Membrane Technology Techniques.* Journal of Applied Polymer Science, 1996.

8. Juan Chen, C.W., Heyi Ge, Yujun Bai, Yanxiang Wang, *Effect of Coagulation Temperature on the Properties of Poly(acrylonitrile-itaconic acd) Fibers in Wet Spinning.* J. Polym. Res., 2007. **14**: p. 223-228.
9. A.K. Gupta, D.K.P., Pushpa Bajaj, *Acrylic Precursors for Carbon Fibers.* Journal of Macromolecular Science, 1991. **C31**(1): p. 1-89.
10. Zussman, E., X. Chen, W. Ding, L. Calabri, D.A. Dikin, J.P. Quintana, and R.S. Ruoff, *Mechanical and structural characterization of electrospun PAN-derived carbon nanofibers.* Carbon, 2005. **43**(10): p. 2175-2185.
11. Grove, D., P. Desai, and A.S. Abhiraman, *Exploratory experiements in the conversion of plasticized melt spun PAN-based precursors to carbon fibers.* Carbon, 1988. **26**(3): p. 403 - 411.
12. Lewin, M., *Handbook of Fiber Chemistry.* 2007.
13. Juan Chen, C.-g.W., Xing-guang Dong, Huan-zhang Liu, *Study on the Coagulation Mechanism of Wet-Spinning PAN Fibers.* Journal of Polymer Research, 2006. **13**: p. 515-519.
14. Chen, L., L. Hao, S. Liu, G. Ding, X. Sun, W. Zhang, F. Li, W. Jiao, F. Yang, Z. Xu, R. Wang, and X. He, *Modulus distribution in polyacrylonitrile-based carbon fiber monofilaments.* Carbon, 2020. **157**: p. 47-54.
15. Morris, E.A. and M.C. Weisenberger, *Solution Spinning of PAN-Based Polymers for Carbon Fiber Precursors*, in *Polymer Precursor-Derived Carbon*, A.K. Naskar and W.P. Hoffman, Editors. 2014, ACS Books. p. 189-213.
16. Chen, J., C. Wang, H. Ge, Y. Bai, and Y. Wang, *Effect of Coagulation Temperature on the Properties of Poly(acrylonitrile-itaconic acd) Fibers in Wet Spinning.* Journal of Polymer Research, 2007. **14**(3): p. 223-228.
17. Tsai, J.-S. and W.-C. Su, *Control of cross-section shape for polyacrylonitrile fibre during wet-spinning.* Journal of Materials Science Letters, 1991. **10**(21): p. 1253-1256.
18. Law, S.J. and S.K. Mukhopadhyay, *Investigation of Wet-Spun Acrylic Fiber Morphology by Membrane Technology Techniques.* Journal of Applied Polymer Science, 1996. **62**: p. 32-47.
19. Craig, J.P., J.P. Knudsen, and V.F. Holland, *Characterization of Acrylic Fiber Structure.* Textile Research Journal, 1962. **32**(6): p. 435-448.
20. Bell, J.P. and J.H. Dumbleton, *Changes in the Structure of Wet-Spun Acrylic Fibers During Processing.* Textile Research Journal, 1971. **41**: p. 196-203.
21. Knudsen, J., *The Influence of Coagulation Variables on the Structure and Physical Properties of an Acrylic Fiber.* Textile Research Journal, 1963. **33**(1): p. 13-20.
22. Morris, E.A., M.C. Weisenberger, and G.W. Rice, *Properties of PAN fibers solution spun into a chilled coagulation bath at high solvent compositions.* Fibers, 2015. **3**(4): p. 560-574.
23. Wang, Y.X., C.G. Wang, Y.J. Bai, and Z. Bo, *Effect of the Drawing Process on the Wet Spinning of Polyacrylonitrile Fibers in a System of Dimethyl Sulfoxide and Water.* Journal of Applied Polymer Science, 2007. **104**: p. 1026-1037.
24. Rajalingam, P. and G. Radhakrishxan, *Polyacrylonitrile Precursor for Carbon Fibers.* Journal of Macromolecular Science, Part C: Polymer Reviews, 1991. **31**(2-3): p. 301-310.

25. Wang, M., Y. Xiao, W. Cao, N. Jiao, W. Chen, and L. Xu, *SAXS and WAXD study of periodical structure for polyacrylonitrile fiber during coagulation.* Polymers for Advanced Technologies, 2015. **26**(2): p. 136-141.
26. Wang, C.G., X.G. Dong, and Q.F. Wang, *Effect of Coagulation on the Structure and Property of PAN Nascent Fibers during Dry Jet Wet-Spinning.* Journal of Polymer Research, 2009. **16**: p. 719-724.
27. Masson, J.C., *Acrylic Fiber Technology and Applications*. 1995, New York, NY: Marcel Dekker, Inc.
28. Arbab, S., P. Noorpanah, N. Mohammadi, and A. Zeinolebadi, *Simultaneous Effects of Polymer Concentration, Jet-Stretching, and Hot-Drawing on Microstructural Development of Wet-Spun Poly(acrylonitrile) Fibers.* Polymer Bulletin, 2011. **66**(9): p. 1267-1280.
29. Junjie, H., L. Chunxiang, Z. Pucha, and L. Denghua, *Pore Structure Development of Polyacrylonitrile Nascent Fibers in Water Stretching Process.* Thermochimica Acta, 2013. **569**: p. 42-47.
30. Postman, W., *Spin Finishes Explained.* Textile Research Journal, 1980. **50**: p. 444-453.
31. Gupta, A.K., D.K. Paliwal, and P. Bajaj, *Acrylic Precursors for Carbon Fibers.* Polymer Reviews, 1991. **31**(1): p. 1-89.
32. Rahaman, M.S.A., A.F. Ismail, and A. Mustafa, *A review of heat treatment on polyacrylonitrile fiber.* Polymer Degradation and Stability, 2007. **92**(8): p. 1421-1432.
33. Ge, Y., Z. Fu, Y. Deng, M. Zhang, and H. Zhang, *The effects of chemical reaction on the microstructure and mechanical properties of polyacrylonitrile (PAN) precursor fibers.* Journal of Materials Science, 2019. **54**(19): p. 12592-12604.
34. Houtz, R., *"Orlon" Acrylic Fiber: Chemistry and Properties.* Textile Research Journal, 1950. **20**(11): p. 786-801.
35. Devasia, R., C.P.R. Nair, P. Sivadasan, B.K. Katherine, and K.N. Ninan, *Cyclization reaction in poly(acrylonitrile/itaconic acid) copolymer: An isothermal differential scanning calorimetry kinetic study.* Journal of Applied Polymer Science, 2003. **88**(4): p. 915-920.
36. Clarke, A. and J. Bailey, *Oxidation of acrylic fibres for carbon fibre formation.* Nature, 1973. **243**(5403): p. 146.
37. Gupta, A. and I. Harrison, *New aspects in the oxidative stabilization of PAN-based carbon fibers.* Carbon, 1996. **34**(11): p. 1427-1445.
38. Ouyang, Q., L. Cheng, H. Wang, and K. Li, *Mechanism and kinetics of the stabilization reactions of itaconic acid-modified polyacrylonitrile.* Polymer Degradation and Stability, 2008. **93**(8): p. 1415-1421.
39. Wang, P., *Aspects on prestretching of PAN precursor: Shrinkage and thermal behavior.* Journal of applied polymer science, 1998. **67**(7): p. 1185-1190.
40. Xiao, S., B. Wang, C. Zhao, L. Xu, and B. Chen, *Influence of oxygen on the stabilization reaction of polyacrylonitrile fibers.* Journal of applied polymer science, 2013. **127**(3): p. 2332-2338.
41. Kikuma, J., T. Warwick, H.-J. Shin, J. Zhang, and B.P. Tonner, *Chemical state analysis of heat-treated polyacrylonitrile fiber using soft X-ray spectromicroscopy.* Journal of electron spectroscopy and related phenomena, 1998. **94**(3): p. 271-278.

42. Nunna, S., C. Creighton, N. Hameed, M. Naebe, L.C. Henderson, M. Setty, and B.L. Fox, *Radial structure and property relationship in the thermal stabilization of PAN precursor fibres.* Polymer Testing, 2017. **59**: p. 203-211.
43. Sun, T., Y. Hou, and H. Wang, *Mass DSC/TG and IR ascertained structure and color change of polyacrylonitrile fibers in air/nitrogen during thermal stabilization.* Journal of Applied Polymer Science, 2010. **118**(1): p. 462-468.
44. Arbab, S. and A. Zeinolebadi, *A procedure for precise determination of thermal stabilization reactions in carbon fiber precursors.* Polymer Degradation and Stability, 2013. **98**(12): p. 2537-2545.
45. Choi, J., S.-S. Kim, Y.-S. Chung, and S. Lee, *Evolution of structural inhomogeneity in polyacrylonitrile fibers by oxidative stabilization.* Carbon, 2020.
46. Watt, W., *Pyrolysis of polyacrylonitrile.* Nature, 1969. **222**(5190): p. 265-266.
47. Friedlander, H.N., L.H. Peebles, J. Brandrup, and J.R. Kirby, *On the Chromophore of Polyacrylonitrile. VI. Mechanism of Color Formation in Polyacrylonitrile.* Macromolecules, 1968. **1**(1): p. 79-86.
48. Standage, A.E. and R. Prescott, *High Elastic Modulus Carbon Fibre.* Nature, 1966. **211**(5045): p. 169-169.
49. Bailey, J. and A. Clarke, *Carbon fibre formation—the oxidation treatment.* Nature, 1971. **234**(5331): p. 529-531.
50. Ogawa, H. and K. Saito, *Oxidation behavior of polyacrylonitrile fibers evaluated by new stabilization index.* Carbon, 1995. **33**(6): p. 783-788.
51. Jain, M.K. and A.S. Abhiraman, *Conversion of acrylonitrile-based precursor fibres to carbon fibres.* Journal of Materials Science, 1987. **22**(1): p. 278-300.
52. Damodaran, S., P. Desai, and A.S. Abhiraman, *Chemical and physical aspects of the formation of carbon fibres from PAN-based precursors.* The Journal of The Textile Institute, 2008. **81**(4): p. 384-420.
53. Lv, M.-Y., H.-Y. Ge, and J. Chen, *Study on the chemical structure and skin-core structure of polyacrylonitrile-based fibers during stabilization.* Journal of Polymer Research, 2008. **16**(5): p. 513-517.
54. Bhat, G., *Structure and properties of high-performance fibers*. 2016: Woodhead Publishing.
55. Jones, W. and J. Johnson, *Intrinsic strength and non-Hookean behaviour of carbon fibres.* Carbon, 1971. **9**(5): p. 645-655.
56. Minus, M. and S. Kumar, *The processing, properties, and structure of carbon fibers.* Jom, 2005. **57**(2): p. 52-58.
57. Sauder, C., J. Lamon, and R. Pailler, *Thermomechanical properties of carbon fibres at high temperatures (up to 2000 C).* Composites Science and Technology, 2002. **62**(4): p. 499-504.
58. Moreton, R., W. Watt, and W. Johnson, *Carbon fibres of high strength and high breaking strain.* Nature, 1967. **213**(5077): p. 690-691.
59. Confidential carbon fiber consultant, *Personal Communication*. 2021.
60. Toray Composite Materials America Inc. *T700S standard modulus carbon fiber*. 2020 [cited 2020 November 19]; Available from: https://www.toraycma.com/wp-content/uploads/T700S-Technical-Data-Sheet-1.pdf.pdf.
61. Kim, P., L. Shi, A. Majumdar, and P.L. McEuen, *Thermal transport measurements of individual multiwalled nanotubes.* Phys Rev Lett, 2001. **87**(21): p. 215502.

62. Hoffman, W., W. Hurley, P. Liu, and T. Owens, *The surface topography of non-shear treated pitch and PAN carbon fibers as viewed by the STM.* Journal of materials research, 1991. **6**(8): p. 1685-1694.
63. Barnet, F.R. and M.K. Norr, *A three-dimensional structural model for a high modulus pan-based carbon fibre.* Composites, 1976. **7**(2): p. 93-99.
64. Johnson, D. and C. Tyson, *The fine structure of graphitized fibres.* Journal of Physics D: Applied Physics, 1969. **2**(6): p. 787.
65. Bennett, S.C., D.J. Johnson, and W. Johnson, *Strength-structure relationships in PAN-based carbon fibres.* Journal of Materials Science, 1983. **18**(11): p. 3337-3347.
66. Griffith, A.A., *The Phenomena of Rupture and Flow in Solids.* Philosophical Transactions of the Royal Society of London, Series A, 1921. **221**: p. 163-198.
67. Warner, S.B., L.H. Peebles, and D.R. Uhlmann, *Oxidative stabilization of acrylic fibres.* Journal of Materials Science, 1979. **14**(3): p. 556-564.
68. Yu, M.-J., C.-G. Wang, Y.-J. Bai, Y. Xu, and B. Zhu, *Effect of oxygen uptake and aromatization on the skin–core morphology during the oxidative stabilization of polyacrylonitrile fibers.* Journal of Applied Polymer Science, 2008. **107**(3): p. 1939-1945.
69. Morris, E.A., M.C. Weisenberger, M.G. Abdallah, F. Vautard, H. Grappe, S. Ozcan, F.L. Paulauskas, C. Eberle, D. Jackson, S.J. Mecham, and A.K. Naskar, *High performance carbon fibers from very high molecular weight polyacrylonitrile precursors.* Carbon, 2016. **101**: p. 245-252.
70. Kong, L., H. Liu, W. Cao, and L. Xu, *PAN fiber diameter effect on the structure of PAN-based carbon fibers.* Fibers and Polymers, 2015. **15**(12): p. 2480-2488.
71. Sun, L., M. Li, L. Shang, L. Xiao, Y. Liu, M. Zhang, and Y. Ao, *The influence of oxygen on skin-core structure of polyacrylonitrile-based precursor fibers.* Polymer, 2020: p. 122516.
72. Nunna, S., C. Creighton, B.L. Fox, M. Naebe, M. Maghe, M.J. Tobin, K. Bambery, J. Vongsvivut, and N. Hameed, *The effect of thermally induced chemical transformations on the structure and properties of carbon fibre precursors.* Journal of materials chemistry A, 2017. **5**(16): p. 7372-7382.
73. Layden, G., *Retrograde core formation during oxidation of polyacrylonitrile filaments.* Carbon, 1972. **10**(1): p. 59-63.
74. Kikuma, J., T. Konishi, and T. Sekine, *Polymer analysis by Auger electron spectroscopy using sectioning and cryogenic cooling.* Journal of electron spectroscopy and related phenomena, 1994. **69**(2): p. 141-147.
75. Karacan, I. and G. Erdoğan, *A study on structural characterization of thermal stabilization stage of polyacrylonitrile fibers prior to carbonization.* Fibers and Polymers, 2012. **13**(3): p. 329-338.
76. Morita, K., Y. Murata, A. Ishitani, K. Murayama, T. Ono, and A. Nakajima, *Characterization of commercially available PAN (polyacrylonitri1e)-based carbon fibers.* Pure and Applied Chemistry, 1986. **58**(3): p. 455-468.
77. Kobayashi, T., K. Sumiya, Y. Fujii, M. Fujie, T. Takahagi, and K. Tashiro, *Stress concentration in carbon fiber revealed by the quantitative analysis of X-ray crystallite modulus and Raman peak shift evaluated for the variously-treated monofilaments under constant tensile forces.* Carbon, 2013. **53**: p. 29-37.

78. Johnson, J.W. and D.J. Thorne, *Effect of internal polymer flaws on strength of carbon fibres prepared from an acrylic precursor.* Carbon, 1969. **7**(6): p. 659-661.
79. Nunna, S., M. Setty, and M. Naebe, *Formation of skin-core in carbon fibre processing: A defect or an effect?* Express Polymer Letters, 2019. **13**(2): p. 146-158.
80. Liu, J., Z. Yue, and H. Fong, *Continuous nanoscale carbon fibers with superior mechanical strength.* Small, 2009. **5**(5): p. 536-42.
81. Liu, F., H. Wang, L. Xue, L. Fan, and Z. Zhu, *Effect of microstructure on the mechanical properties of PAN-based carbon fibers during high-temperature graphitization.* Journal of Materials Science, 2008. **43**(12): p. 4316-4322.
82. Gu, Y., M. Li, J. Wang, and Z. Zhang, *Characterization of the interphase in carbon fiber/polymer composites using a nanoscale dynamic mechanical imaging technique.* Carbon, 2010. **48**(11): p. 3229-3235.
83. Liu, X., C. Zhu, J. Guo, Q. Liu, H. Dong, Y. Gu, R. Liu, N. Zhao, Z. Zhang, and J. Xu, *Nanoscale dynamic mechanical imaging of the skin–core difference: From PAN precursors to carbon fibers.* Materials Letters, 2014. **128**: p. 417-420.
84. Cooper, G.A. and R.M. Mayer, *The strength of carbon fibres.* Journal of Materials Science, 1971. **6**(1): p. 60-67.
85. Loidl, D., O. Paris, H. Rennhofer, M. Müller, and H. Peterlik, *Skin-core structure and bimodal Weibull distribution of the strength of carbon fibers.* Carbon, 2007. **45**(14): p. 2801-2805.
86. Reynolds, W.N. and J.V. Sharp, *Crystal shear limit to carbon fibre strength.* Carbon, 1974. **12**(2): p. 103-110.
87. Xue, Y., J. Liu, F. Lian, and J. Liang, *Effect of the oxygen-induced modification of polyacrylonitrile fibers during thermal-oxidative stabilization on the radial microcrystalline structure of the resulting carbon fibers.* Polymer Degradation and Stability, 2013. **98**(11): p. 2259-2267.
88. Guo, X., Y. Cheng, Z. Fan, Z. Feng, L. He, R. Liu, and J. Xu, *New insights into orientation distribution of high strength polyacrylonitrile-based carbon fibers with skin-core structure.* Carbon, 2016. **109**: p. 444-452.
89. Gandhi, S. and R.E. Lyon, *Health hazards of combustion products from aircraft composite materials*. 1998, Federal Aviation Administration Technical Center: Atlantic City, NJ. p. 1-29.
90. Kumar, S., D.P. Anderson, and A.S. Crasto, *Carbon fibre compressive strength and its dependence on structure and morphology.* Journal of Materials Science, 1993. **28**(2): p. 423-439.

CHAPTER 2. THE HOLLOW FIBER APPROACH

2.1 Overview of hollow fibers

As discussed previously, traditional CF require lengthy and costly oxidation processing, and often possess an undesirable skin-core structure. The above reports suggest that the core of CF does relatively little to contribute to the overall tensile properties of the fiber. One potential solution which reduces the characteristic diffusion length, mitigating skin-core structure development and increasing specific tensile properties, is the development of hollow carbon fibers by intentionally spinning precursor PAN hollow fiber (HF) and converting them into hollow carbon fiber (HCF). The proposed HCF have the potential to improve on traditional solid CF properties by effectively reducing fiber density (resulting in higher specific strength and modulus) which can lead to lighter weight parts. As CF strength has been found to be largely governed by surface flaws [1], the omission of the fiber core is hypothesized to have minimal impact on tensile strength, and therefore the production of a HF has the potential to conserve the tensile strength of a traditional solid fiber. In fact, conservation of tensile strength has been previously shown for hollow glass fiber, compared to a solid fiber [2].

In addition to the hypothesis of preservation of tensile strength, it is hypothesized that the oxidation of a hollow PAN-based precursor fiber will allow oxygen diffusion to proceed in two directions, from the outside, as per conventional solid fiber oxidation, but also from the inner lumen (hollow portion). This would significantly reduce the characteristic diffusion length when compared to a traditional solid fiber, as seen in Figure 2.1. For this diffusion-limited process, taking the ratio of dimensionless Fourier mass transfer numbers, N_{Fo}, for both the solid (N_{Fo}^{S}) and hollow (N_{Fo}^{H}) filaments (as shown in Figure 2.1) allows the effect of diffusion length on process time to be calculated and compared using Eqn. 2.1. The diffusivity of O_2 in PAN, D, is assumed equivalent for both hollow and solid fibers. The characteristic timescales are represented for solid (t_s) and hollow (t_H) fibers. Assuming a 14 μm outer diameter (OD) and 9.3 μm inner diameter (ID) precursor hollow fiber, the diffusion distance is half the wall thickness, as oxidation proceeds in both directions. Therefore, the diffusion distance for the HF, l_H, is 1.175 mm.

For a conventional precursor fiber 14 μm in diameter, where oxidation proceeds from the outside only, the diffusion distance for the solid fiber, l_S, is 7.0 mm. Assuming the ratio of Fourier mass transfer numbers is unity, the oxidation of a hollow fiber would be expected to require **35x** less time than that of conventional solid fiber (t_s/t_H). And all else equal, the HF would not develop the skin-core structure of the solid fiber.

$$\frac{N_{Fo}^{S}}{N_{Fo}^{H}} = \frac{\frac{Dt_s}{l_s^2}}{\frac{Dt_H}{l_H^2}} \qquad \text{Eqn. 2.1}$$

If this hypothesis is correct, this increase in oxidation speed could result in a significant reduction in CF cost [3], as oxidation is known to be the rate limiting step in the production of carbon fiber [4]. Typical oxidation process line speeds are 10-30 m/min, while typical spinning speeds are an order of magnitude faster. Aside from improving line speed, the reduction in characteristic diffusion length during oxidation is hypothesized to lead to a more homogeneous morphology, negating any skin-core effect that may be present in traditional solid fibers.

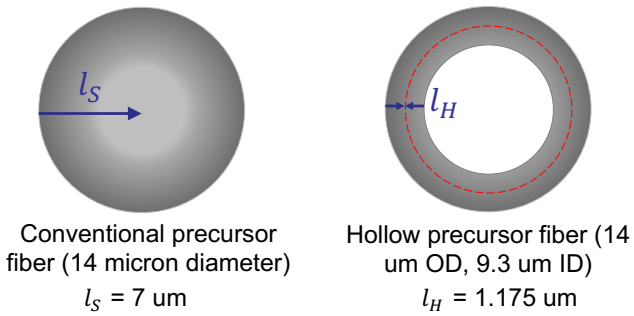

Figure 2.1. Comparison of characteristic diffusion length for a conventional solid (l_S) versus a hollow (l_H) fiber.

The development of HCF is not a new idea. In fact, various approaches and materials have been utilized in an attempt to produce consistently high-quality, structural HCF. Some of the first hollow carbon fibers were actually produced by accident following incomplete stabilization of PAN precursor fiber. Upon carbonization, it was found that the

severely under-stabilized core had vaporized, producing a “hollow fiber”, albeit with poor morphology and properties [5, 6]. The following section will introduce a few of the methods used in attempts to produce HCF, as well as the relative successes and failures of those methods, including electrospinning, melt spinning, and solution (wet) spinning.

2.2 Previous research

Before delving into previous research into HCF development, it is important to describe the methods by which HF and HCF properties are calculated, as they will be discussed here as well as throughout the remained of this work. There are two primary methods for determining HF cross sectional area which are illustrated in Figure 2.2. True area is calculated based on the solid cross-sectional area. True area, in the case of a HF, is the annulus area. Effective area is calculated as the area within the HF outer diameter and contains both the area of the HF annulus and lumen. Effective area is always greater than true area for a HF. True area and effective area are equivalent for a solid fiber. Tensile stress calculated as force per true area will be greater than that based on effective area. However, from the viewpoint of a CF composite material, the effective measurements are of primary importance.

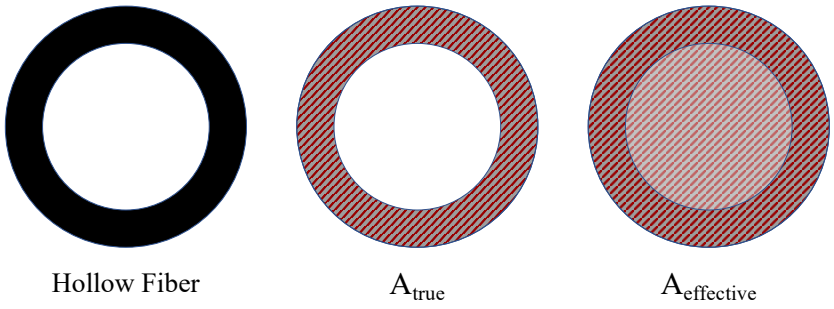

Figure 2.2. Schematic showing area determination for a hollow fiber, where true area is defined as the area of the solid and effective area is the area contained within the outer diameter of the filament.

2.2.1 Electrospinning

Electrospinning relies on a high voltage electric field to accelerate electrically charged jets from polymer solutions or melts, which solidify by means of solvent

evaporation or melt cooling. The highly charged fibers are directed toward a rotating drum or collector plate that is either grounded or of the opposite charge, where they are most commonly collected as a non-woven mat [7]. Resulting fiber diameters vary but are typically on the nanometer scale. Coaxial electrospinning (needle within needle) has been used to produce HCF measuring 100s of nanometers in outer diameter, but some versions have relied on the use of a sacrificial core, which is burned or dissolved out after the spinning process. While a sacrificial core provides support during spinning for the future HCF, its complete removal can be difficult, and difficult removal may be detrimental to the resulting CF properties. While electrospinning can be cost effective to produce nanoscale HCF, the filaments produced are not intended for structural applications, but rather for use in solar cells, lithium-ion rechargeable batteries, super capacitors, or as catalysts [8]. Additionally, the non-woven mats traditionally produced during electrospinning cannot be held under proper tension during the thermal conversion process, resulting in CF with tensile properties inferior to those of CF derived from a continuous solution spun process [9]. As a result, electrospinning of HCF is not ideal for producing CF for high-performance structural applications.

2.2.2 Melt spinning

Melt spinning entails heating a polymer above its melting or softening point and extruding through a spinneret. The filaments solidify in air as they move from the heated spinneret to the take-up spool. Melt spinning is a commonly used process to produce continuous fibers from a variety of polymer sources, including polyester, nylon, and polypropylene, for example. Hollow filaments are routinely spun from a melt spinning process utilizing C-shaped or segmented arc spinnerets (2C, 3C, or 4C) [10, 11], as shown in Figure 2.3. When utilizing, for example, the C-shaped spinneret, the molten material exits the C-shaped capillary and air is allowed to enter the open fissure in the forming fiber. However, as the fiber moves ever farther from the spinneret, the fissure begins to heal as the molten material coalesces and cools. Finally, the fissure is fully healed and cooled, resulting in a hollow filament. The air drawn in through the fissure before the fiber heals aids in preventing the collapse of the fiber walls. An illustration of this phenomenon is presented in Figure 2.4 for the melt spinning of polypropylene hollow filaments [11-13].

The fissure length has been found to be greatly impacted by the polymer die swell [11]. This same principle of fissure healing also applies to segmented arc spinnerets (2C, 3C, and 4C).

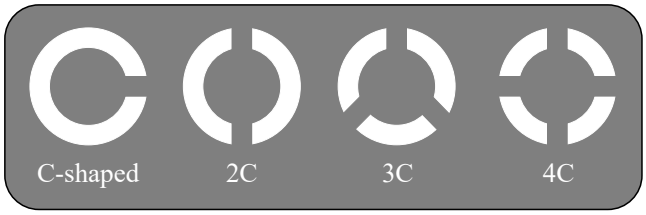

Figure 2.3. Common segmented arc spinneret capillary designs used during the melt spinning of hollow filaments.

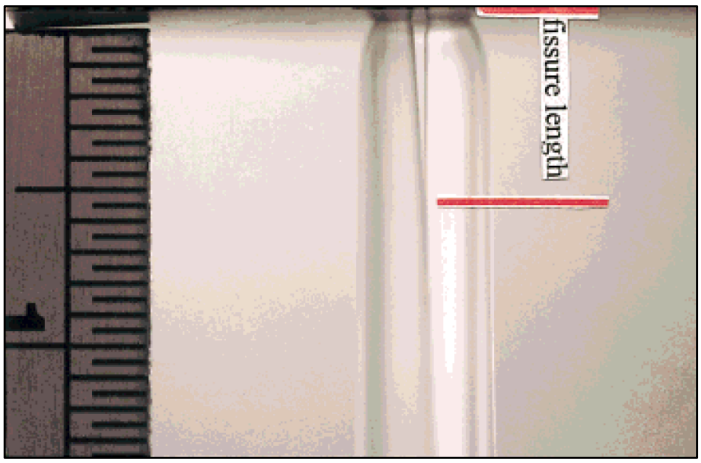

Figure 2.4. Formation of a hollow polypropylene filament during melt spinning, illustrating healing of the fissure in the air gap to form a hollow filament. Reprinted from [11] with permission © 2001 John Wiley & Sons, Inc.

Pitch is a commonly melt spun material, often used as a precursor for high modulus, high thermal conductivity (but low strain-to-failure) CF. Studies exist comparing traditional solid, C-shaped, and hollow isotropic pitch-derived CF and their composites [14]. Shim et al. developed pitch-derived C-shaped and hollow CF [14]. The calculated effective tensile properties of the solid (R-CF) and hollow isotropic pitch-derived CF (H-CF) are shown in Table 2.1. The H-CF showed a lower effective tensile strength, but a higher effective modulus compared to their traditional solid fiber counterparts. The effective tensile strength difference was likely impacted by the larger outer diameter of the

H-CF compared to the solid CF (34 μm compared to 22 μm). While isotropic pitch-derived CF are useful in some applications, their use in structural applications is limited.

Table 2.1. Comparison of isotropic pitch-derived carbon fiber properties of round/traditional solid (R-CF) and hollow (H-CF), calculated based on effective cross-sectional areas. Adapted from [14].

Carbon Fiber Type	Outer Diameter (μm)	Inner Diameter (μm)	Effective Tensile Strength (MPa)	Effective Elastic Modulus (GPa)
R-CF	22	N/A	932	55
H-CF	34	20	706	67

An alternative to melt spinning of pitch would seem to be the melt spinning of PAN. However, PAN is known to degrade prior to melting [15]. It is for this reason that it is spun utilizing a solution spinning process. However, there have been attempts to melt spin PAN, but thus far none have been found to be commercially viable [16-18]. In fact, there exists a BASF patent application (which has since been withdrawn) for the melt spinning of PAN-based HCF with a C-shape. The outer diameters indicated were 5 to 20 μm, with fiber wall thicknesses ranging from 0.5 to 5 μm. However, no images or fiber properties were given [19].

2.2.3 Solution spinning

As described earlier, solution spinning relies on a dual diffusion process of nonsolvent in and solvent out of the forming fiber to begin solidification. The control of this diffusion process is vital to controlling the morphology of the resulting filaments and, as a result, the final fiber properties [20]. Solution spun hollow PAN fibers have been produced, although primarily for application as asymmetric gas separation membranes. In this application, PAN hollow fiber are large in diameter (0.5 to 1 mm) and consist of a spongy sub-structure through much of the hollow fiber wall, which supports a very thin, dense fiber skin. These fibers are not designed to be precursors for CF or to possess high tensile properties and are produced utilizing a bore-fluid approach (to be described). Some researchers have attempted to use such an approach in the production of PAN HF precursors. In addition to a bore-fluid approach, other approaches used to solution spin PAN HF precursors include bicomponent spinning and the use of segmented arc spinnerets

(similar to those used in melt spinning). Previous work toward the production of PAN HF precursors utilizing these methods will be discussed.

2.2.3.1 Bore fluid approach

Commonly used to produce HF membranes, a bore fluid approach relies on an internal fluid (gas or liquid) which is fed through a needle to form and maintain the hollow filament. In some instances, the bore fluid, in addition to holding the wall of the forming fiber open, contains the chemistry necessary to help form the porous substrate which supports the separating layer. A needle supplying this lumen fluid must be placed concentrically within the spinneret capillary, around which the dope flows. Due to manufacturing limitations, the minimum needle diameter available is larger than desired for producing PAN HF precursors. In addition, HF membranes are not commonly spun in a multifilament tow, as each capillary must be assured of concentric placement of its individual bore fluid needle. On the contrary, traditional solid PAN precursors are spun in thousands of filaments per tow. Despite these bore-fluid limitations, attempts have been made to utilize this approach for the production of PAN hollow filaments as precursors for carbon fiber [21]. For example, Thewlis utilized a single-filament bore-fluid approach to spin PAN, using a spinneret orifice diameter of 600 μm and a needle OD of 330 μm. Fibers were drawn to achieve small diameters [22]. Images of the resulting fibers are shown in Figure 2.5. PAN HF measuring 28 μm in OD were produced, with an effective density of 0.84 g/cc. The effective density (ρ_{eff}) was calculated according to Eqn. 2.2,

$$\rho_{eff} = 1.18\left[1 - \left(\frac{\emptyset_{ID}}{\emptyset_{OD}}\right)^2\right] \qquad \text{Eqn. 2.2}$$

where $\emptyset_{ID}$ is the inner diameter, $\emptyset_{OD}$ is the outer diameter, and 1.18 refers to the typical density of PAN (1.18 g/cc). These PAN HF precursors had a maximum effective tensile strength and elastic modulus of 227 MPa and 4.9 GPa, respectively [22]. The filaments lacked concentricity (as shown in Figure 2.5a, b, and c) and appeared to suffer from variations in wall thickness along the fiber length, as shown in Figure 2.5d, all of which would be detrimental to the final carbon fiber tensile properties.

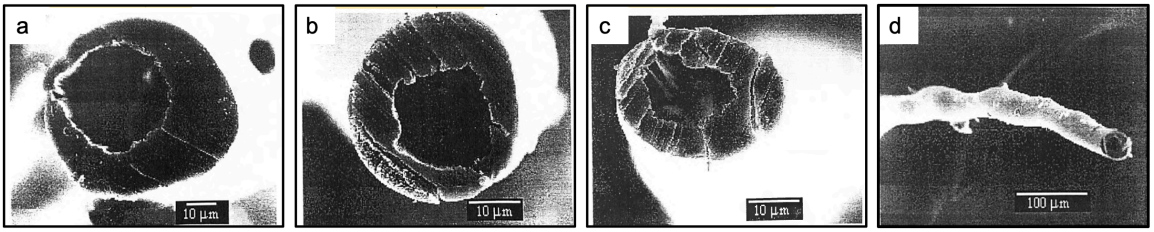

Figure 2.5. Cross-sectional images (a, b, and c) of hollow precursor filaments spun from PAN using a single-filament bore-fluid approach, where (d) shows a side view of fiber (b). Reprinted with permission from the author [22].

Other attempts to utilize a bore-fluid have been undertaken. Similar to Thewlis, Ferguson [23] filed a patent reporting bore-fluid solution spinning of PAN HF. Properties of the resulting fibers are shown in Table 2.2**,** adapted from [23]. The highest effective tensile strength achieved was 261 MPa, with 4.1 GPa effective elastic modulus for a 57 µm OD HF. Again, these tensile properties are encouraging but fall short of those typically found in traditional solid fiber PAN precursors (see Table 1.2). Ferguson also did not detail the morphology of the resulting filaments.

Table 2.2. Properties of hollow PAN precursor filaments spun by Ferguson using a multifilament bore-fluid approach. Adapted from [23].

Outer Diameter (µm)	Inner Diameter (µm)	Effective Break Strength (MPa)	Effective Elastic Modulus (GPa)
60	47	146	0.9
66	51	200	1.2
63	43	226	2.5
57	35	261	4.1

The literature presented above by Thewlis and Ferguson represent the few attempts made to utilize a bore-fluid approach to produce PAN HF as precursors for structural HCF. While interesting, the bore-fluid approach remains limited in its ability to co-spin thousands of filaments and has been unable to achieve the outer diameters of traditional solid precursors (10-12 µm), which is important for efficient thermal conversion processing, and therefore investigation of alternative approaches continues.

2.2.3.2 Bicomponent Spinning Approach

Some researchers have considered the use of a sacrificial polymer to form the hollow portion of the fiber to produce smaller diameter HF with thinner walls, improved concentricity, and reduced variation. In this case, fibers are typically spun as biocomponent fibers, with the sheath consisting of PAN and lumen filled with PMMA, PVA, or similar sacrificial polymer. This lumen filling is then removed via dissolution during fiber washing or via vaporization during thermal conversion, leaving behind a PAN HF. For example, Yaodong et al. utilized a bicomponent method to produce PAN-based HCF using PMMA as a sacrificial core [24], as shown in Figure 2.6. The precursor PMMA filled PAN fiber is shown in Figure 2.6a. The PMMA was removed during oxidative stabilization (Figure 2.6b), although the process by which the thermal degradation products exit the fiber remains unclear. However, tensile results for the resulting HCF were presented (evaluated at a 6 mm gauge length and 0.36 mm/min crosshead speed). The calculated effective tensile properties of the HCF were 2280 MPa tensile strength and 198 GPa modulus, as shown in Table 2.3. The resulting HCF cross-sections are shown in Figure 2.6c, and at the time (2015), Yaodong claimed the highest reported values for HCF [24].

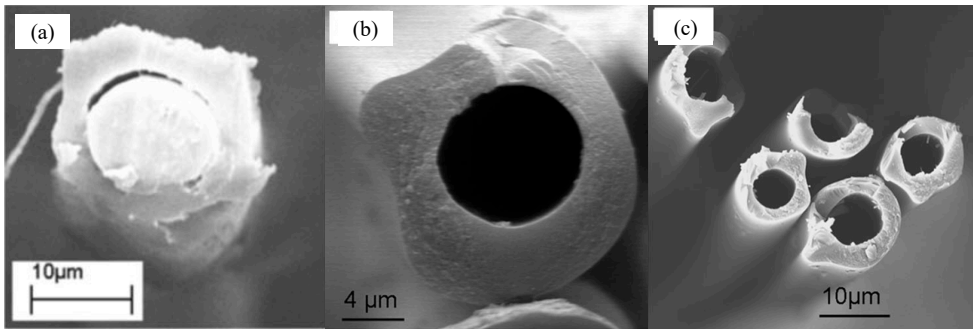

Figure 2.6. (a) Precursor PAN/PMMA fiber; (b) Stabilized PAN/PMMA fiber; (c) PAN based HCF produced utilizing a sacrificial PMMA core. Reprinted from [24] by permission from Springer Nature.

Following Yaodong, Gulgunje et al. [25] utilized the bicomponent spinning method to produce PAN/PMMA "honeycomb" fibers. Here again, the PMMA was removed during thermal conversion. Resulting tensile properties are shown in Table 2.3. The "honeycomb" HCF, when measured at a gauge length of 12.7 mm and strain rate of 0.1 %/s, resulted in an effective break strength of 1750 MPa and effective modulus of 268 GPa. Cross-sectional images of the precursor and resulting CF are shown in Figure 2.7a and b, respectively.

Table 2.3. Effective tensile properties of hollow PAN precursor and CF spun using a bicomponent spinning method. PAN/PMMA HF precursor and resulting PAN HCF adapted from [24]. Honeycomb precursor and resulting CF adapted from [25].

Fiber	OD (μm)	ID (μm)	Effective Density (g/cc)	Effective Break Strength (MPa)	Effective Elastic Modulus (GPa)	Strain at Break (%)
PAN/PMMA HF Precursor	17.3	---	---	650	14	---
PAN HCF	8.8	5	1.3	2280	198	1.2
Honeycomb PAN Precursor	16.3	---	---	400	10	7.3
Honeycomb PAN CF	9.3	---	1.2	1750	268	0.7

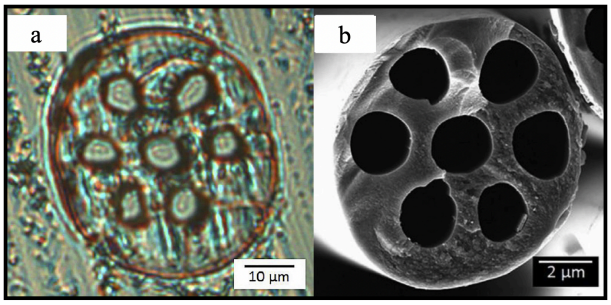

Figure 2.7. (a) As-spun honeycomb PAN precursor fiber with PMMA islands. (b) Honeycomb carbon fiber cross section. Reprinted from [25] with permission from Elsevier.

The results produced thus far utilizing bicomponent spinning have shown promise, however, the sacrificial polymer approach suffers from drawbacks similar to the bore-fluid approach, wherein a specialized spinneret and second pump and filtration system is required to allow for bi-component spinning. Significant modification to capital spinning plants would be needed for commercial scale manufacturing of these filaments from a bicomponent spinning process. Additionally, questions remain surrounding the thermal degradation of PMMA in the fiber and its impact on not only the fiber but the oxidation and carbonization ovens.

2.2.3.3 Segmented arc spinneret approach

The use of a segmented arc spinneret could serve as a drop-in replacement for commercial solid fiber spinnerets for air gap spinning. While these spinnerets have been traditionally used for the production of melt spun hollow filaments [10, 11], they have yet to be used extensively for solution spinning. The methods previously described to produce

HF (bore-fluid and bicomponent spinning approaches) rely on the presence of a solid or liquid material in the fiber lumen to keep the fiber open and hollow during extrusion and fiber solidification. When using a segmented arc spinneret, the lumen is supported by a gas (typically air), which enters through the fiber fissure (shown in Figure 2.3). Unlike melt spinning, wherein the molten segments can heal and begin to solidify through cooling immediately upon exiting the spinneret, during air gap spinning the spinning solution does not begin to solidify until it enters the coagulation bath. Therefore, time spent in the air gap is pivotal to HF formation. For example, too little time and the HF may not form, but only produce solid segments. Too much time and the segments heal but then coalesce to form a solid fiber. This is just one example of a multitude of variables that must be carefully controlled to produce a HF when air gap solution spinning with a segmented arc spinneret (other variables include, but are not limited to, spinning solution temperature, jet draw, coagulation bath composition and temperature, etc.).

Due to its complexity, solution spinning with segmented arc spinnerets is currently uncommon, although they have been utilized for the dry spinning of hollow cellulose acetate fibers. In dry spinning, solvent evaporation rather than coagulation in a nonsolvent, solidifies the fibers [26]. For solution spinning PAN HF, few reports have been published. Zhang et al. appear to have been most successful solution-spinning PAN HF from a 2C segmented arc spinneret. They found that the length of the air gap impacted the resulting fiber shape and had to be carefully controlled to produce HF [27]. At a 6.1 mm air gap, fibers were circular and well-formed, as shown in Figure 2.8c. However, the resulting precursor HF measured ~190 μm OD, much larger than conventional solid commercial precursor fibers (10-12 μm). Additionally, a patent awarded to Hyundai Motor Company claimed the production of HCF from a 2C spinneret with 4.5 GPa effective tensile strength and 235 GPa effective modulus. Little information is given regarding the fiber, aside from Hyundai noting that oxidative stabilization time was indeed 45 min. shorter than for traditional solid fiber [28]. To the author's knowledge this process is not practiced/licensed, nor is the Hyundai Motor Company currently active in carbon fiber industry. None of the claimed properties have been published in peer reviewed articles. Finally, a paper published in the China Synthetic Fiber Industry journal by Longming et al. [29] shows the impact of coagulation bath concentration on PAN HF formation from a C-shaped

segmented arc spinneret. The few reports available describing solution spinning of PAN utilizing a segmented arc spinneret indicate that the area requires further research to successfully produce HCF for structural applications.

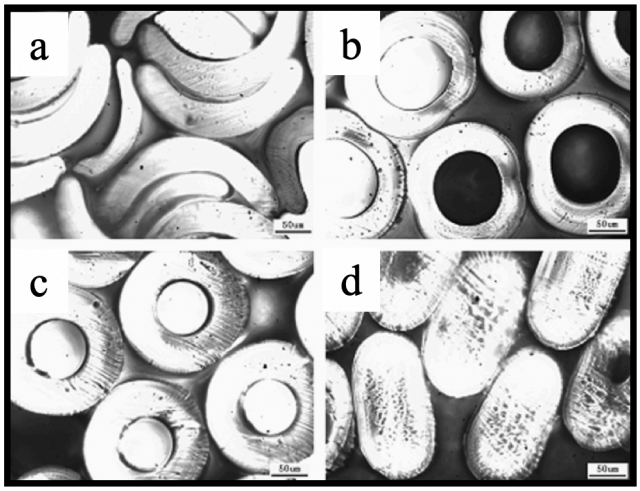

Figure 2.8. Impact of air gap distance on HF formation for a 2C spinneret: (a) 2.5 mm, (b) 4 mm, (c) 6.1 mm, (d) 10 mm. Reprinted from [27] with permission from Taylor & Francis.

2.3 Objectives

The literature review presented here contains an extensive analysis of previous work completed toward the production of HCF for structural applications. Electrospinning can be cost effective, however the filaments produced are not intended nor suited for structural applications, are often produced in non-woven mats, and require the use of a sacrificial core. Melt spinning of PAN remains an experimental endeavor and has not matured to the level required for production of structural fibers, and a bore-fluid spinning approach is not amenable to scale up to the tens of thousands of filaments typically co-spun in traditional solid CF processes. The bicomponent spinning approach has produced HCF with adequate tensile properties, however, commercial adoption of such a process would require expensive capital investments and retooling as well as the use of a sacrificial polymer, further increasing manufacturing costs. Finally, efforts toward solution spinning PAN HF with segmented arc spinnerets are rare, with only three references located after extensive literature review. If the advantages of a segmented arc spinneret can be realized, its use removes the need for a sacrificial polymer or bore fluid and is inherently scalable to 1000s

of filaments. Additionally, a segmented arc spinneret can serve as a drop-in replacement for traditional air gap spinnerets in large-scale manufacturing lines, requiring minimal additional capital investments. Considering these possibilities, the research presented herein is focused upon the use of a segmented arc spinneret to develop high tensile property HCF and to understand the process-structure-property development throughout the spinning, oxidative stabilization, and carbonization processes. The objectives of this research are presented here.

To the author's knowledge, only two references exist describing the impact of spinning variables on HF formation from a segmented arc spinneret. Zhang et al. investigated the impact of air gap distance on HF formation [27] while Longming et al. investigated the impact of coagulation bath composition [29]. Resulting filaments were very large or improperly formed. The initial objective of this research focuses upon the development of multifilament PAN HF precursor from the segmented arc spinneret. **It is hypothesized that a segmented arc spinneret can be used to produce HF precursors with dimensions and morphology appropriate to the production of high tensile property HCF.** Within this study, objectives include the contribution of knowledge to the understanding of the HF filament formation in the air gap and coagulation bath, with a focus on controlling the morphology development to minimize void formation and dimension control. Additionally, observations regarding the relationships between the coagulation bath, fiber washing and drawing, and thermal conversion is explored. Finally, tensile analysis of the PAN HF precursors is completed and their trends analyzed toward the production of high tensile property HCF, particularly with regard to comparison with traditional solid precursors.

Next, a particular hypothesized advantage of HF is the potential for faster oxidation. Here, **it is hypothesized that with reduced wall thickness, one can arrive at an optimally oxidized fiber faster than traditional solid fiber via oxidation from the exterior and interior of the filament**. As wall thickness decreases, the oxygen characteristic diffusion length decreases, compared to a solid fiber of the same OD, as shown in Figure 2.1. Spun HF precursors of varying OD and ID are oxidized and their stabilized fiber densities utilized as a proxy for oxygen uptake [30] to determine rate of

oxidation. These results are compared to solid fibers of similar OD. Knowledge related to the mechanisms behind HF oxidative stabilization are investigated and contributed.

Finally, one of the overarching goals of this research is to understand the resulting HCF properties. Two primary hypotheses regarding HCF properties have been developed. **First, it is hypothesized that the resulting effective tensile strength of the HCF can conserve the tensile strength of a similar OD solid CF.** This is hypothesized based on findings from other researchers previously discussed in section 1.1.4.2, who found that surface flaws are a major limiting factor in CF tensile strength [6, 31], as the skin carries up to 10 times the stress compared to the core [32] and that reducing or eliminating the skin-core structure would allow for homogeneous stress distribution along the fiber cross section, leading to improved tensile properties [6, 31]. **Second, it is hypothesized that the true elastic modulus of the HCF will increase as a function of increasing percent open area (for a fixed outer diameter) due to the reduction in skin-core structure in the HCF.** As described previously, the literature indicates that the majority of commercially available CF possess a skin-core structure, which results in the highly oriented, high modulus skin carrying much of the load [33, 34]. This suggests that the formation of a HCF would more efficiently exploit the oriented portion of the fiber. Considering the effective density of a HCF would be lower than a solid CF (of same the OD), and considering the arguments above, the specific tensile properties of HCF could be significantly superior to solid carbon fiber. After all, as mentioned in section 1.1.4, the specific tensile properties of carbon fiber underpin its utility in an array of structural applications.

The objectives and hypotheses discussed above are pertinent in the development of PAN HF precursor and PAN-derived HCF. To date, these questions have not been adequately addressed in the literature. Those who have attempted to develop and study HCF have conducted relatively little analyses of the fibers. Addressing these hypotheses would lead to a deeper understanding of the fundamentals governing PAN HF and HCF development and would represent a significant advancement in the field, which has, for the most part, been incrementally advancing over the past 30 years. If successful, the production of HCF has the potential to disrupt the entire carbon fiber market, which as of 2018, was estimated to be valued at $3-4B worldwide [35]. The questions addressed in the

work are relevant for technology advancement to produce hollow carbon fiber at lower cost and higher throughput (due to a potential increased oxidation rate), and to potentially significantly increase HCF specific strength and modulus the central basis of carbon fiber.

2.4 References

1. Johnson, J.W. and D.J. Thorne, *Effect of internal polymer flaws on strength of carbon fibres prepared from an acrylic precursor.* Carbon, 1969. **7**(6): p. 659-661.
2. Kling, S. and T. Czigany, *A comparative analysis of hollow and solid glass fibers.* Textile Research Journal, 2013. **83**(16): p. 1764-1772.
3. Weisenberger, M. and A. Morris. *Precursor processing development for low cost, high strength carbon fiber for composite overwrapped pressure vessel applications*. US Department of Energy 2018; Available from: https://www.hydrogen.energy.gov/pdfs/review18/st146_weisenberger_2018_p.pdf.
4. Morgan, P., *Carbon fibers and their composites*. 2005, Boca Raton, LA: Taylor & Francis Group.
5. Balasubramanian, M., M.K. Jain, and A.S. Abhiraman, *Evolution of structure and properties in contrinuous carbon fiber formation*, in *Biennial Conference on Carbon*. 1985: England. p. 312-313.
6. Liu, J., Z. Yue, and H. Fong, *Continuous nanoscale carbon fibers with superior mechanical strength.* Small, 2009. **5**(5): p. 536-42.
7. Subbiah, T., G.S. Bhat, R.W. Tock, S. Parameswaran, and S.S. Ramkumar, *Electrospinning of nanofibers.* Journal of Applied Polymer Science, 2005. **96**(2): p. 557-569.
8. Ju, A., S. Hou, Y. Pan, Y. Wang, Y. Zhu, and H. Chen, *Preparation of hollow carbon submicro-fibers with controllable wall thicknesses from acrylonitrile copolymer.* Textile Research Journal, 2017. **88**(16): p. 1893-1901.
9. Zussman, E., X. Chen, W. Ding, L. Calabri, D.A. Dikin, J.P. Quintana, and R.S. Ruoff, *Mechanical and structural characterization of electrospun PAN-derived carbon nanofibers.* Carbon, 2005. **43**(10): p. 2175-2185.
10. Wang, C.Y., M.W. Li, Y.L. Wu, and C.T. Guo, *Preparation and microstructure of hollow mesophase pitch-based carbon fibers.* Carbon, 1998. **36**(12): p. 1749-1754.
11. Rwei, S.-P., *Formation of hollow fibers in the melt-spinning process.* Journal of Applied Polymer Science, 2001. **82**(12): p. 2896-2902.
12. Lee, M.S., T.H. Oh, S.Y. Kim, and H.J. Shim, *Deformation kinetics of polypropylene hollow fibers in a continuous drawing process.* Journal of Applied Polymer Science, 1999. **74**(7): p. 1836-1845.
13. De Rovere, A., B.P. Grady, and R.L. Shambaugh, *The influence of processing parameters on the properties of melt-spun polypropylene hollow fibers.* Journal of Applied Polymer Science, 2002. **83**(8): p. 1759-1772.
14. Shim, H.B., J.I. Lee, H.S. Kim, Y.J. Choe, and B.S. Rhee. *On hollow and C-type carbon fiber reinforced composite materials*. in *International Conference on Advanced Composite Materials (ICACM)*. 1993.

15. Morris, E.A. and M.C. Weisenberger, *Solution Spinning of PAN-Based Polymers for Carbon Fiber Precursors*, in *Polymer Precursor-Derived Carbon*, A.K. Naskar and W.P. Hoffman, Editors. 2014, ACS Books. p. 189-213.
16. Liu, S., K. Han, L. Chen, Y. Zheng, and M. Yu, *Structure and properties of partially cyclized polyacrylonitrile-based carbon fiber-precursor fiber prepared by melt-spun with ionic liquid as the medium of processing.* Polymer Engineering & Science, 2015. **55**(12): p. 2722-2728.
17. Mahmood, S.F., B.L. Batchelor, M. Jung, K. Park, W.E. Voit, B.M. Novak, and D. Yang, *Study of a melt processable polymer precursor for carbon fiber.* Carbon Letters, 2019. **29**(6): p. 605-612.
18. Lee, J.H., J.-U. Jin, S. Park, D. Choi, N.-H. You, Y. Chung, B.-C. Ku, and H. Yeo, *Melt processable polyacrylonitrile copolymer precursors for carbon fibers: Rheological, thermal, and mechanical properties.* Journal of Industrial and Engineering Chemistry, 2019. **71**: p. 112-118.
19. Fitzer, E. and W. Metzler, Hollow carbon fibres. 1990.
20. Morris, E.A., M.C. Weisenberger, and G.W. Rice, *Properties of PAN fibers solution spun into a chilled coagulation bath at high solvent compositions.* Fibers, 2015. **3**(4): p. 560-574.
21. Noland, R.L. and T.D. O'Brien, Hollow carbon fibers. U.S. Patent 5,338,605. August 16, 1994.
22. Thewlis, R., *The spinning of hollow polyacrylonitrile fibres as a precursor for the formation of hollow carbon fibres*. 1998, University of Strathclyde.
23. Ferguson, J., Apparatus and method for spinning hollow polymeric fibres. U.S. Patent 6,143,411. November 7, 2000.
24. Liu, Y., H.G. Chae, Y.H. Choi, and S. Kumar, *Preparation of low density hollow carbon fibers by bi-component gel-spinning method.* Journal of Materials Science, 2015. **50**(10): p. 3614-3621.
25. Gulgunje, P.V., B.A. Newcomb, K. Gupta, H.G. Chae, T.K. Tsotsis, and S. Kumar, *Low-density and high-modulus carbon fibers from polyacrylonitrile with honeycomb structure.* Carbon, 2015. **95**: p. 710-714.
26. Hao, J.H., H. Dai, P. Yang, and Z. Wang, *Spinning of cellulose acetate hollow fiber by dry-wet technique of 3C-shaped spinneret.* Journal of Applied Polymer Science, 1996. **62**(1): p. 129-133.
27. Zhang, X., Y. Wen, Y. Yang, and L. Liu, *Effect of air-gap distance on the formation and characterization of hollow polyacrylonitrile (PAN) nascent fibers.* Journal of Macromolecular Science, Part B, 2008. **47**(6): p. 1039-1049.
28. Choi, Y.H., S. Han, and C.H. Choi, Preparation method for hollow carbon fiber. U.S. Patent 9,109,305. August 18, 2015.
29. Longming, W., Y. Yang, and X. Lianghua, *Formation mechanism of PAN hollow fiber prepared by wet spinning process.* China Synthetic Fiber Industry, 2012. **35**(1): p. 26-30.
30. Choi, J., S.-S. Kim, Y.-S. Chung, and S. Lee, *Evolution of structural inhomogeneity in polyacrylonitrile fibers by oxidative stabilization.* Carbon, 2020.
31. Liu, F., H. Wang, L. Xue, L. Fan, and Z. Zhu, *Effect of microstructure on the mechanical properties of PAN-based carbon fibers during high-temperature graphitization.* Journal of Materials Science, 2008. **43**(12): p. 4316-4322.

32. Kobayashi, T., K. Sumiya, Y. Fujii, M. Fujie, T. Takahagi, and K. Tashiro, *Stress concentration in carbon fiber revealed by the quantitative analysis of X-ray crystallite modulus and Raman peak shift evaluated for the variously-treated monofilaments under constant tensile forces.* Carbon, 2013. **53**: p. 29-37.
33. Huang, Y. and R.J. Young, *Effect of Fibre Microstructure Upon the Modulus of PAN- and Pitch-Based Carbon Fibres.* Carbon, 1995. **33**(2): p. 91-107.
34. Liu, X., C. Zhu, J. Guo, Q. Liu, H. Dong, Y. Gu, R. Liu, N. Zhao, Z. Zhang, and J. Xu, *Nanoscale dynamic mechanical imaging of the skin–core difference: From PAN precursors to carbon fibers.* Materials Letters, 2014. **128**: p. 417-420.
35. Das, S., J. Warren, D. West, and S.M. Schexnayder, *Global carbon fiber composites supply chain competitiveness analysis*. 2016, Oak Ridge National Laboratory; The University of Tennessee, Knoxville.

CHAPTER 3. EXPERIMENTAL METHODS AND CHARACTERIZATION TECHNIQUES

This chapter provides a detailed description of the experimental methods and techniques that are used repeatedly throughout the following chapters. Experimental methods specific to a given chapter will be described in the experimental section of that chapter.

3.1 Lyophilization (freeze drying)

Coagulated fibers were generally collected by allowing fibers to "spool" on godet rollers directly following the coagulation bath. The fibers were then carefully removed from the roller and excess external liquid removed utilizing lint-free wipes (Kimwipes). To avoid fiber porosity collapse due to air drying, the fibers were placed in bottles of deionized water until ready for lyophilization. Freeze drying was completed utilizing a Labconco FreeZone 1-Liter Benchtop Freeze Dry System. Samples were removed from deionized water, excess external liquid again removed with lint-free wipes, and the samples frozen in liquid nitrogen prior to addition to the system's freeze drying flasks. The flasks containing the frozen samples were attached to the FreeZone system, which was maintained at 0.050 mbar and -50 °C. Samples were allowed to lyophilize for several hours until all frost disappeared from the outer surface of the sample container, indicating the sample was dry and ready for further analysis.

3.2 Fiber sectioning

Following freeze drying to preserve the coagulated fiber structure, fibers were sectioned using a Leica CM1100 portable benchtop cryostat. The cryostat was utilized to section not only freeze dried coagulated fibers, but also fibers collected at other positions in the spinning process, including after washing, drying, and final spooling. The cryostat was necessary for sectioning the polymer (precursor) fibers to prevent deforming the fiber during sectioning. During preparation for sectioning, approximately 1 cm of fiber tow was bundled using Cu tape and then placed in a mold filled with Tissue-Tek O.C.T compound. This mold was then placed under moderate vacuum for approximately 10 minutes when studying hollow fiber (HF) to aid the O.C.T. compound in filling the hollow lumen. Molds

were then placed inside the cryostat, which was maintained at -30 °C for freezing of the sample and compound. Once frozen, the embedded sample was removed from the mold and attached to the cryostat specimen holder, perpendicular to the stationary cutting blade. The sample was trimmed using the cutting blade and then removed from the specimen holder and washed in deionized water for several hours to fully remove any O.C.T. residue.

3.3 Optical microscopy

Cross sections of precursor, stabilized, and carbonized HF were observed under optical microscopy. Fibers were held vertical in uncured epoxy and placed under vacuum to encourage filling the HF lumen. The epoxy was then allowed to cure overnight at room temperature or in an hour at 50 °C and polished perpendicular to the fiber axis for imaging. Fiber cross sections were imaged at 500x magnification under reflected light. Under reflected light, the skin-core structure of the oxidized fibers was visible, with the skin appearing lighter in color than the core. Diameters and other measurements were obtained using Adobe Photoshop 2021. In Photoshop, the measurement scale is set and the magnetic lasso tool used to trace the region of interest, allowing measurements such as area and perimeter, for example, to be collected. The average value of measurements was calculated, and error bars represented the standard deviation for the sample.

3.4 Scanning electron microscope (SEM)

Imaging of the fibers was performed on a Hitachi S-4800 field emission SEM. Precursor and stabilized fibers were sputter coated with Au prior to imaging generally at 5 kV accelerating voltage and 10 μA beam current. Carbon fibers did not require sputter coating and were generally imaged at 15 kV accelerating voltage and 15 μA beam current. Fibers were bundled and sandwiched between Cu tape and cut, either using the Leica CM1100 cryostat (coagulated and precursor fibers) or a razor (carbon fibers) for viewing the fiber cross section. Samples for fiber surface imaging were prepared by laying fibers across conductive carbon tape. Diameters and other measurements were obtained using Adobe Photoshop 2021 to analyze the resulting micrographs. The average value of measurements was calculated, and error bars represented the standard deviation for the sample.

3.5 Focused ion beam

Prior to elemental composition analysis by energy dispersive X-ray spectroscopy (EDX), the fibers were cross-sectioned in a dual beam system: focused ion beam / scanning electron microscope (FIB/SEM, Helios Nanolab 660/G3, ThermoFisher Scientific, formerly FEI, Hillsboro, OR). Fibers were attached onto a 45° pre-tilted SEM sample holder using carbon and copper conductive tapes and further immobilized by conductive graphite paint (Ted Pella, Inc.) to limit drift. Based on the dual beam geometry (52° between the electron and ion beam), the stage was tilted to 7° during ion milling so that the ion beam was normal - and the created cross-section face perpendicular - to the long axis of the fibers. Milling was conducted using gallium ions accelerated to an energy of 30 keV, until the end of the fibers were cut, revealing a fresh cross-section face. After completion of the milling process, the stage was tilted to 45° to position this face normal to the electron beam for imaging and energy-dispersive X-ray spectroscopy (EDX) analysis.

3.6 Energy-dispersive X-ray spectroscopy (EDX)

Elemental analysis by EDX (X-Max^N 80 mm^2 detector, Oxford Instruments, Abingdon, United Kingdom) was conducted in the same dual beam system immediately after completion of the cross-sectioning step. The freshly exposed cross-section surface was therefore not exposed to air prior to analysis, as it remained in the high vacuum of the system's chamber (pressure typically lower than 10^{-6} mbar). Incident electrons with 10 keV energy were used to perform the EDX analysis, sufficiently energetic to fully excite the characteristic X-rays of the elements present in the sample. A total of 10 million EDX spectra were collected to create the EDX maps (2048 channels over 10 keV energy range, i.e. resolution of 4.88 eV per channel). The proprietary software from Oxford Instruments (AZtec) performed background fitting and peak deconvolution to properly identify and display the presence of specific elements in the map.

3.7 Density measurements

Precursor and stabilized fiber densities were analyzed using a Testing Machines Inc. Model 21-25 Auto Density Gradient Column. Glass beads with densities calibrated to four decimal places were placed in the column to form a calibration curve. Fibers were washed

overnight in methanol and vacuum dried before placing into a column of carbon tetrachloride and n-heptane. Fibers were allowed to equilibrate for at least 24 hours and three specimen per sample were analyzed.

Carbon fiber density was determined on chopped fiber using a Micromeritics Accupyc II 1340, equipped with a 0.1 cc cell. To avoid water uptake by CF during density measurements, the Accupyc II system was located in a dry room, which was maintained at 0.03% humidity and fibers were dried prior to measurement. Dry nitrogen was used as the gas and 10 measurements per sample were obtained.

Both the density gradient column and the gas pycnometer provided "true" (or skeletal) densities (ρ_{true}). These measurements were then used to calculate the effective densities (ρ_{eff}), according to Eqn. 3.1, where A_{true} and A_{eff} are the true and effective cross sectional areas of the fiber, as defined in Figure 2.2.

$$\rho_{\text{eff}} = \rho_{\text{true}} \frac{A_{\text{true}}}{A_{\text{eff}}} \qquad \text{Eqn. 3.1}$$

The percent density increase from the precursor was calculated for all oxidized samples using Eqn. 3.2,

$$\frac{(\rho_i - \rho_p)}{\rho_p} \times 100 \qquad \text{Eqn. 3.2}$$

where ρ_p is the true density of the precursor fiber and ρ_i is the density of the oxidized fiber, where i refers to after the i$^{\text{th}}$ heating stage of oxidation ($i = 1^{\text{st}}, 2^{\text{nd}}, 3^{\text{rd}}, 4^{\text{th}}$).

3.8 Mechanical characterization

Tensile testing of precursor fibers was done using a Textechno FAVIMAT+ROBOT2(AI) automatic single fiber test system. Tests were performed at a gauge length of 25.4 mm, pretension of 0.5 cN/tex, and test speed of 5 mm/min. The average of at least 10 tests are reported for each fiber sample and error bars represent the standard deviation.

To avoid damage to the HCF by the FAVIMAT+ grips, single filament HCF were mounted on aperture cards using epoxy and tested using an MTS QTest10 testing machine,

equipped with a 250 g load cell. Single filaments were evaluated at a 10 mm gauge length with a test speed of 0.1 mm/min. At least 12 filaments were analyzed for each sample and effective tensile properties reported. No compliance correction for modulus or strain was performed.

The true and effective tensile properties of the precursor fibers were calculated based on the true and effective areas of the hollow fibers (see Figure 2.2). In addition, when determining specific properties, the effective fiber densities were always used in order to observe the impact of cross-sectional area on specific properties. For example, Eqn. 3.3 shows the equation for determining specific effective tensile strength, where F is the fiber break force, A_{eff} is the fiber effective area, and ρ_{eff} is the effective density. Similarly, in Eqn. 3.4, the specific true tensile strength is calculated, where A_{true} is the fiber true area, again defined as shown in Figure 2.2. Specific effective and true modulus were calculated in a similar fashion, as shown in Eqn. 3.5 and Eqn. 3.6, where ε is the fiber strain under the applied force, F.

$$\text{specific } \textbf{effective} \text{ tensile strength} = \frac{F/\boldsymbol{A_{\text{eff}}}}{\rho_{\text{eff}}} \qquad \text{Eqn. 3.3}$$

$$\text{specific } \textbf{true} \text{ tensile strength} = \frac{F/\boldsymbol{A_{\text{true}}}}{\rho_{\text{eff}}} \qquad \text{Eqn. 3.4}$$

$$\text{specific } \textbf{effective} \text{ elastic modulus} = \frac{F/\boldsymbol{A_{\text{eff}}}}{\varepsilon\rho_{\text{eff}}} \qquad \text{Eqn. 3.5}$$

$$\text{specific } \textbf{true} \text{ elastic modulus} = \frac{F/\boldsymbol{A_{\text{true}}}}{\varepsilon\rho_{\text{eff}}} \qquad \text{Eqn. 3.6}$$

3.9 Wide angle x-ray scattering (WAXS)

The precursor HF and HCF were analyzed using a XENOCS Xeuss 2.0 SAXS/WAXS system in transmission mode to determine structural parameters and orientation. The source was GeniX^{3D}Cu ULD 8 keV with wavelength of 0.154 nm. Several fibers were aligned into a bundle and fixed across an aperture card. The aperture card with the aligned fiber bundle was then transferred to the WAXS sample holder which was placed at 106 mm from the 2D detector (Dectris Pilatus 200 K) following LaB_6 calibration. Exposure time was 600 s.

For precursor PAN fiber, the diffraction pattern of the equatorial scan contains PAN fiber peaks at 2θ = ~16.5° and 29.5°, which represent the Bragg angles associated with the (100) and (110) planes. These planes correspond to a nearly perfect hexagonal spacing of 6.0 Å [1], represented by the lattice parameters $a = c = 6.17$ Å [2] which define the cell dimensions. For the CF, the resulting crystal structure is shown by the peaks at Bragg angles 2θ = 25° and 42°, representing the (002) and (100) planes.

Data processing to obtain the integrated diffracted intensity versus 2θ and azimuthal angle, Ψ, was performed using the software Foxtrot provided by XENOCS. Structural parameters were determined by peak fitting of the Foxtrot data using Rigaku PDXL 2.0 software. For both precursor and CF, the degree of crystallinity was calculated as the ratio of the integral intensity contained within the crystalline peaks to the integral intensity of the entire sample [3]. Crystallite size $L_{c_{(002)}}$ and $L_{a_{(100)}}$ were calculated using the Scherrer equation found in Eqn. 3.7 and the interlayer spacing, $d_{(002)}$, was calculated using Bragg's Law using Eqn. 3.8, respectively,

$$L = \frac{k\lambda}{\beta \cos\theta} \qquad \text{Eqn. 3.7}$$

$$d = \frac{\lambda}{2\sin\theta} \qquad \text{Eqn. 3.8}$$

where λ is the x-ray wavelength 0.154 nm, θ is the Bragg angle, β is the full width at half maximum (FWHM) of the diffraction peak with respect to 2θ, and the k value is a

constant of 0.9 for $L_{c_{(002)}}$ and 1.84 for $L_{a_{(100)}}$ [4]. To quantify the degree of orientation of the fibers, the Herman's orientation factor, $f_{(002)}$, was calculated from the WAXS data using

$$\langle \cos^2 \Psi_{(002),z} \rangle = \frac{\int_0^{\pi/2} I(\Psi) \cos^2 \Psi \sin \Psi d\Psi}{\int_0^{\pi/2} I(\Psi) \sin \Psi d\Psi} \quad \text{Eqn. 3.9}$$

and

$$f_{(002)} = \frac{3\langle \cos^2 \Psi_{(002),z} \rangle - 1}{2} \quad \text{Eqn. 3.10}$$

In Eqn. 3.9 and Eqn. 3.10, Ψ is the azimuthal angle, $I(\Psi)$ represents the azimuthal intensities, and $\langle \cos^2 \Psi_{(002),z} \rangle$ is the average cosine square of the angle that the (002) plane made with the draw direction, z. As a result, $f_{(002)} = 1$ for perfectly oriented crystal planes parallel to the draw direction and $f_{(002)} = -0.5$ when the orientation of the crystal planes is perpendicular to the draw direction, and $f_{(002)} = 0$ for an isotropic material with no preferred orientation [5]. Finally, a T700S carbon fiber sample was also analyzed as a benchmark.

3.10 References

1. Rizzo, P., F. Auriemma, G. Guerra, V. Petraccone, and P. Corradini, *Conformational disorder in the pseudohexagonal form of atactic polyacrylonitrile.* Macromolecules, 1996. **29**(27): p. 8852-8861.
2. Colvin, B.G. and P. Storr, *The crystal structure of polyacrylonitrile.* European Polymer Journal, 1974. **10**(4): p. 337-340.
3. Mikolajczyk, T., S. Rabiej, G. Szparaga, M. Boguń, A. Fraczek-Szczypta, and S. Błażewicz, *Strength properties of polyacrylonitrile (PAN) fibres modified with carbon nanotubes with respect to their porous and supramolecular structure.* Fibres & Textiles in Eastern Europe, 2009. **17**(6): p. 13-20.
4. Yang, F., W. Liu, M. Yi, L. Ran, Y. Ge, and K. Peng, *Effect of high temperature treatment on the microstructure and elastoplastic properties of polyacrylonitrile-based carbon fibers.* Carbon, 2020. **158**: p. 783-794.
5. Chuah, H.H. and B.T.A. Chang, *Crystal orientation function of poly(trimethylene terephthalate) by wide-angle x-ray diffraction.* Polymer Bulletin, 2001. **46**(4): p. 307-313.

CHAPTER 4. PROCESSING AND PROPERTIES OF HOLLOW PAN FIBER PRECURSORS FROM A SEGMENTED ARC SPINNERET

4.1 Introduction

Polyacrylonitrile precursors for the production of high tensile property CF typically have few (if any) voids, small diameter (approximately 10-12 μm), low comonomer content, >50% carbon yield in the resulting CF, and high tensile strength and modulus [1-4]. The utilization of PAN hollow fiber (HF) to produce structural hollow carbon fiber (HCF) has not been widely explored. As discussed in section 2.2, electrospinning [5] and melt spinning [6] methods have been explored to produce precursors for HCF, but have produced inferior products.

The approaches demonstrating the most promise in the production of precursors for HCF are based on a solution spinning method, and include bore-fluid [7-9], bicomponent [10, 11], and segmented arc spinneret approaches [12-14]. Unfortunately, the bore-fluid approach relies on concentric placement of the needle supplying the lumen fluid within the spinneret capillary. Due to manufacturing limitations, the minimum needle diameter available is larger than desired for producing PAN HF precursors. In addition, the bore-fluid approach is primarily suited to single filament spinning and is not appropriate for spinning thousands of filaments per tow, as is common for PAN precursors.

The bicomponent approach has shown promise in producing HF and HCF with adequate tensile properties, but the use of a sacrificial polymer to form the hollow portion of the filament increases production costs through the addition of secondary pumping systems and complicated spinneret geometries. The vaporization of the sacrificial polymer during thermal conversion also has questionable effects on the fiber and the ovens used during thermal treatment.

Finally, the use of a segmented arc spinneret shows the most promise in terms of ease of conversion from traditional solid precursor spinning to HF spinning, as the segmented arc spinneret can serve as a direct drop-in replacement for traditional solid fiber, air-gap spinnerets. Unfortunately, little research has been completed on the use of segmented arc spinnerets for solution spinning. Solution spinning with a segmented arc spinneret relies

on healing of the segments in the air gap prior to entering the coagulation bath (similar to the healing shown in Figure 2.4) and little is understood regarding the process-structure-property relationships in the development of HF PAN precursors. A schematic of a 2C segmented arc spinneret capillary being used for solution spinning is shown in Figure 4.1. **It was hypothesized that a segmented arc spinneret could be used to produce HF precursors with dimensions and morphology appropriate to the production of high tensile property HCF.** This chapter reports on the investigation of this hypothesis, including the spinning process and the resulting HF precursors and includes observations regarding coagulation, fiber drawing, and the resulting HF precursor tensile properties.

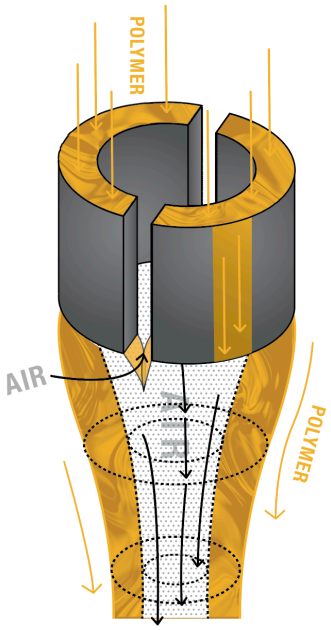

Figure 4.1. Schematic describing the use of a segmented arc spinneret capillary for the production of hollow filaments from a solution spinning method. The spinning solution exiting the 2C segments of the capillary heal to produce a hollow filament. Air is drawn in between the healing segments to maintain the hollow structure.

4.2 Experimental

4.2.1 Materials

Two types of polyacrylonitrile terpolymers were utilized during the course of this research. Both polymers contained 97 mol% acrylonitrile, 2 mol% methyl acrylate, and 1

mol% methacrylic acid and were obtained from Technorbital Advanced Materials Pvt. Ltd. (Kanpur, India). The first of the polymers, TechPAN1 (TP1), had a weight average molecular weight (M_w) of 300,000 g/mol (via GPC). The second polymer, TechPAN2 (TP2), was of lower molecular weight, estimated to be approximately 150,000 g/mol. Dimethylsulfoxide (DMSO), 99.9%, was purchased from VWR and used as received.

4.2.2 Dope preparation

Spinning solutions were prepared using an 8 CV Helicone Reactor/Mixer (Design Integrated Technology Inc., Warrenton, VA). The TechPAN polymer was added, along with DMSO, to the 50 °C preheated mixer and mixed at 15 RPM utilizing the intersecting dual heliconical blades over 12 hours at 50 °C to produce a homogeneous spinning solution. The solution was degassed under vacuum in the mixer and finally extracted using 2 psi N_2 overpressure into a 1 L syringe pump (Teledyne ISCO 1000D, Lincoln, NE).

4.2.3 Spinneret design

Multiple spinneret configurations were designed and utilized for this study (Table 4.1), to discern the best dimensional configuration for producing the smallest dimension filaments. All spinnerets were configured to produce 25 hollow filaments using 2C segmented arc capillary designs. Schematics of the spinneret and capillary are shown in Figure 4.2.

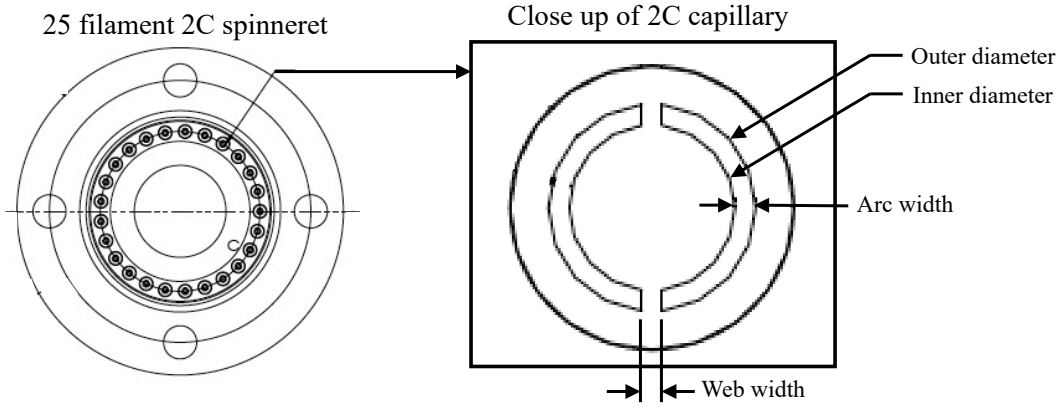

Figure 4.2. Schematics of the 25 filament 2C segmented arc spinneret with a close up of the 2C capillary.

HF-A was the first and primary spinneret utilized for this research. Attempts with HF-B were made, which was designed with significantly reduced OD and ID, however, machining limits meant that the arc and web width could go no smaller than 71 and 51 μm, respectively. As a result of the relatively large arc and web widths compared to the OD and ID, HF was not well formed. A third iteration, HF-C, reduced the OD and ID, but maintained the arc and web width from HF-A. HF-C was successful in producing HF, albeit with large wall thickness to OD ratios compared to fibers produced with HF-A, as will be discussed.

Table 4.1. 2C segmented arc spinnerets designed and utilized for this research, including inner and outer capillary diameters, as well as arc and web width.

Spinneret	Number of 2C Segmented Arc Capillaries	Capillary Outer Diameter (μm)	Capillary Inner Diameter (μm)	Arc Width (μm)	Web Width (μm)
HF-A	25	1000	800	100	100
HF-B	25	416	280	71	51
HF-C	25	680	540	100	100

4.2.4 Solution spinning apparatus

The solution spinning line used for this research is located at the University of Kentucky Center for Applied Energy Research. A schematic of the spinning line is shown in Figure 4.3. The line begins with a 1 L Teledyne ISCO pump which contains the deaerated, fully dissolved spinning solution. The ISCO uses positive displacement to control the volumetric flow rate of dope fed through a 3 μm microglass filter element, through a breaker plate, and into the spinneret. The 2C jets exit the spinneret and pass through an air gap (5-15 mm) before entering the coagulation bath. The coagulation bath is typically a mixture of solvent and non-solvent, from 0 to 80 wt.% solvent/non-solvent. For this study, the solvent is dimethylsulfoxide (DMSO) and the non-solvent is water. The remainder of the spinning line consists of godet stands typically configured with four rollers as well as baths for washing and drawing (or stretching) of the filaments. The godet stands are controlled for linear speed to apply the desired draw ratio to the fiber in each bath, as shown in Eqn. 4.1, where v_{y_i} is the velocity of first godet (y_0, y_1, y_2, etc.) and $v_{y_{(i+1)}}$ is the velocity of the next godet (y_1, y_2, y_3, etc.). The ratio of the velocities is the draw down ratio (DDR), or stretch, applied to the fiber between the two godets.

$$\mathrm{DDR} = \frac{v_{y_{(i+1)}}}{v_{y_i}} \qquad \text{Eqn. 4.1}$$

Following coagulation, the godets move the fiber tow through a series of water wash baths (T ~20 °C) for removal of fiber residual solvent. Upon reaching godet y_3, the following three baths are heated water. The first two warm water baths (T ~50 °C) aid in further washing of the fiber, while in the third hot water bath (T ~90 °C) the first major draw of the fiber occurs. Following this first major draw, the fibers make multiple passes around the godet rollers on y_6, which is a heated godet (T ~60 °C). This is necessary to dry and remove water prior to entering the hot glycerol stretching bath (T ~160 °C). The use of hot glycerol enables the application of high draw ratios to the fiber tow by heating the fiber significantly above its glass transition (T_g) and serves as an excellent heat transfer medium. After drawing through hot glycerol, it is necessary to again wash the fiber in hot water (T ~90 °C) to remove glycerol from the fiber. This is completed using two baths. Finally, a dilute aqueous silicone emulsion spin finish is added to the fiber for handleability and to aid with subsequent thermal conversion, and the fiber tow is finally dried over another larger heated godet (T ~60 °C) and spooled using a traversing winder. Spools were labeled with a run number as well as a letter (A, B, C, etc.) to designate that differing conditions were utilized during the same spinning run to collect the respective spool.

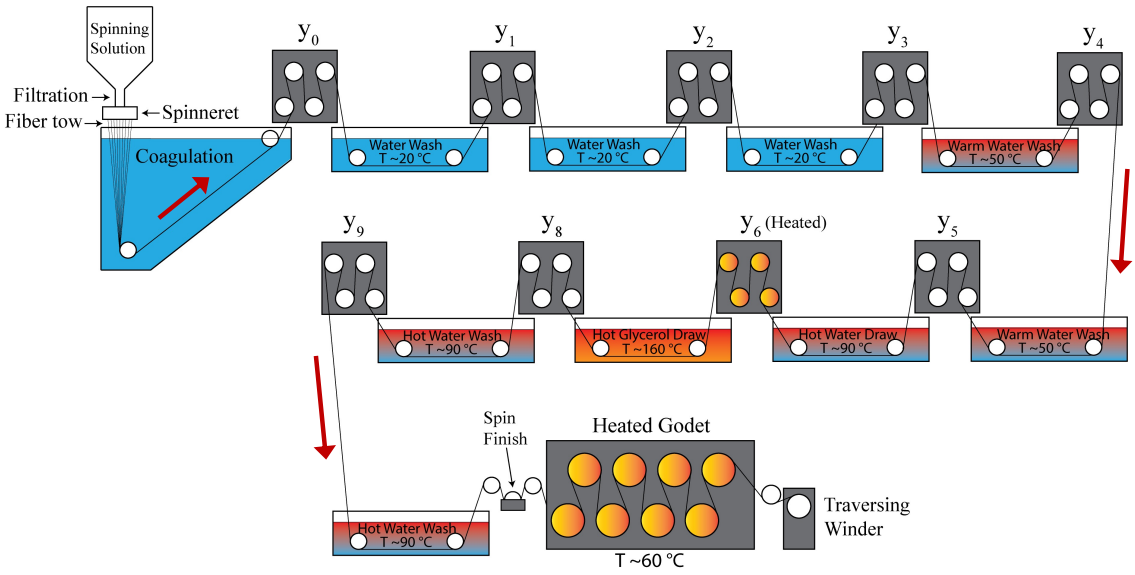

Figure 4.3. Schematic of the solution spinning line at the UK Center for Applied Energy Research utilized for the hollow fiber research.

4.2.5 Rheological analysis

Shear rheology studies were conducted on both TechPAN1 and TechPAN2 polymer solutions using a TA Instruments AR-G2 parallel plate rheometer. Polymer solutions were placed between the Peltier temperature controlled bottom plate, held fixed, and the top rotating 40 mm diameter parallel plate tool. The gap between the Peltier and the tool was maintained at 500 µm. Experiments were conducted by ramping the applied shear rate from 0.1 to 10 s^{-1} while measuring shear viscosity (Pa-s). Additional experiments were conducted by holding the shear rate constant at 1 s^{-1} and ramping the temperature from 25 to 80 ºC while measuring the viscosity (Pa-s).

4.2.6 Thermogravimetric analysis (TGA)

A TA Instruments Discovery Thermogravimetric Analyzer (TGA 5500) was utilized to determine the residual liquid content present in precursor HF by evaporation. The residual liquid is likely comprised of a mix of water and DMSO. Prior to analysis, 10 to 15 mg of precursor fiber sample were chopped into ~1 mm lengths and added to a tared 250 µL alumina crucible. The samples were analyzed by ramping from room temperature to

400 °C at 20 °C/min in flowing N_2 (25 mL/min). Residual liquid content was determined by the weight percent change from room temperature to 275 °C.

4.2.7 Differential scanning calorimetry (DSC)

A TA Instruments Discovery Differential Scanning Calorimeter (DSC 2500) was utilized to examine exothermic events. For exotherm observation, polymer powders were dried under vacuum to remove adsorbed water and 4-6 mg of sample was added to a Tzero DSC pan, which was then fitted with a Tzero lid. Samples were heated under 50 mL/min of N_2 from room temperature to 450 °C at 10 °C/min.

4.3 Results and discussion

4.3.1 Initial coagulation trials

Initial work on the spinning of hollow filaments began with the use of TechPAN1 polymer, which had previously been proven in-house to produce high-quality solid precursor fibers and CF with tensile properties similar to T700S (Table 1.1 and Table 1.2). Having extensively studied the formation of solid PAN precursor fibers, particularly in the coagulation bath, it was known that high solvent content in the coagulation bath (>70 wt.%, but <80 wt.%, solvent/non-solvent) produces precursor fibers with circular cross section, smaller diameters, higher density, higher molecular orientation, and higher tensile properties [15].

Utilizing this knowledge, initial spinning trials with the HF-A 2C segmented arc spinneret to develop hollow fibers focused on the use of a high solvent content coagulation bath, with the goal being to produce round, dense, concentric hollow PAN precursor fibers. Contrary to expectations, fibers spun into a 78 wt.% DMSO/water bath attained none of the desired characteristics. In Figure 4.4, a resulting coagulated fiber cross section is shown, displaying macrovoids on the order of 10s of microns in diameter positioned around the fiber circumference. It was hypothesized that the high solvent content coagulation bath, which is preferred for the formation of solid fibers due to the slow coagulation, allowed for the collapse of the 2C segments and the formation of a relatively solid, macrovoid-filled fiber. To prevent this collapse, a potential solution was the removal of solvent from the

bath and the use of a 100% non-solvent (water) bath. Spinning into 100% non-solvent leads to the rapid outward diffusion of non-solvent, resulting in the instantaneous precipitation of the polymer [16]. This rapid precipitation leads to a dense cuticle formation on the surface of the fiber, which in the context of the HF spinning reported here, was hypothesized to aid in preserving the lumen of the nascent, healed 2C segments during fiber formation, resulting in a concentric HF.

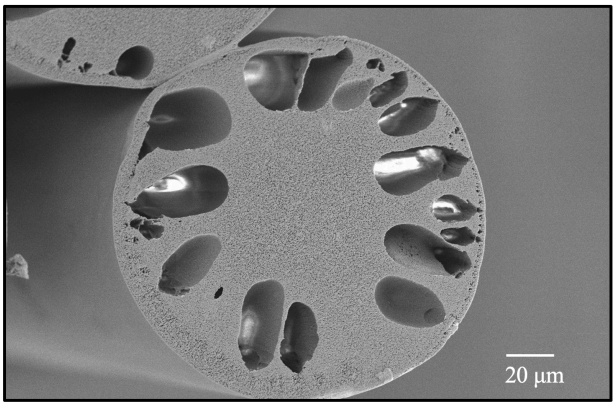

Figure 4.4. Resulting coagulated fiber cross section from initial 2C segmented arc spinneret spinning trials, which were spun into a 78 wt.% DMSO/water coagulation bath.

To test this hypothesis, numerous spinning runs utilizing a 100% water coagulation bath and the HF-A spinneret were completed. Initial spinning experiments were somewhat Edisonian in nature as attempts were made to determine which of the numerous spinning variables (outside of coagulation bath composition) were most impactful on initial HF filament formation. Important variables under observation during the formation of hollow filaments were air gap distance, dope flow rate, and draw down ratio, to name a few. The concentration of TechPAN1 in DMSO to produce the spinning solution varied between 14 and 16 wt.%. Higher solids content (polymer) in the spinning solution was preferred as it is known to produce a slightly more homogeneous structure formation [17, 18]. However, higher solids content also increases solution viscosity, which can lead to difficulties properly degassing the solution to remove entrained gasses and the high viscosity can render spinning difficult. Issues with void formation in the spun fibers would lead to the use of a 14 wt.% TechPAN1/DMSO solution in some instances, as this solution was easier to degas compared to the 16 wt.% solution. However, the presence of macrovoids in the

HF being related to entrained gasses in the spinning solution was eventually debunked, as will be discussed.

Examples of coagulated fiber cross sections from early experiments are shown in Figure 4.5. Figure 4.5a, b, c, d, e, and f show cross sections from spinning runs 419, 420, 423, 476, 478, and 480, respectively. Table 4.2 includes the air gaps, flow rates, and draw down ratios (DDR) used to produce these fibers. For the fiber sections shown here, air gaps varied from 6 to 10 mm, flow rates from 4 to 8 mL/min, and draw down ratios (DDR) from 0.8 to 5, where DDR through the coagulation bath is calculated according to Eqn. 4.2. In Eqn. 4.2, it is shown that flow rate and DDR are dependent on one another, where v_{y_0} is the linear velocity of the godet rollers at the coagulation bath exit (y_0), A is the total area of the spinneret capillaries, and Q is the volumetric flow rate controlled by the positive-displacement pump through the spinneret capillaries.

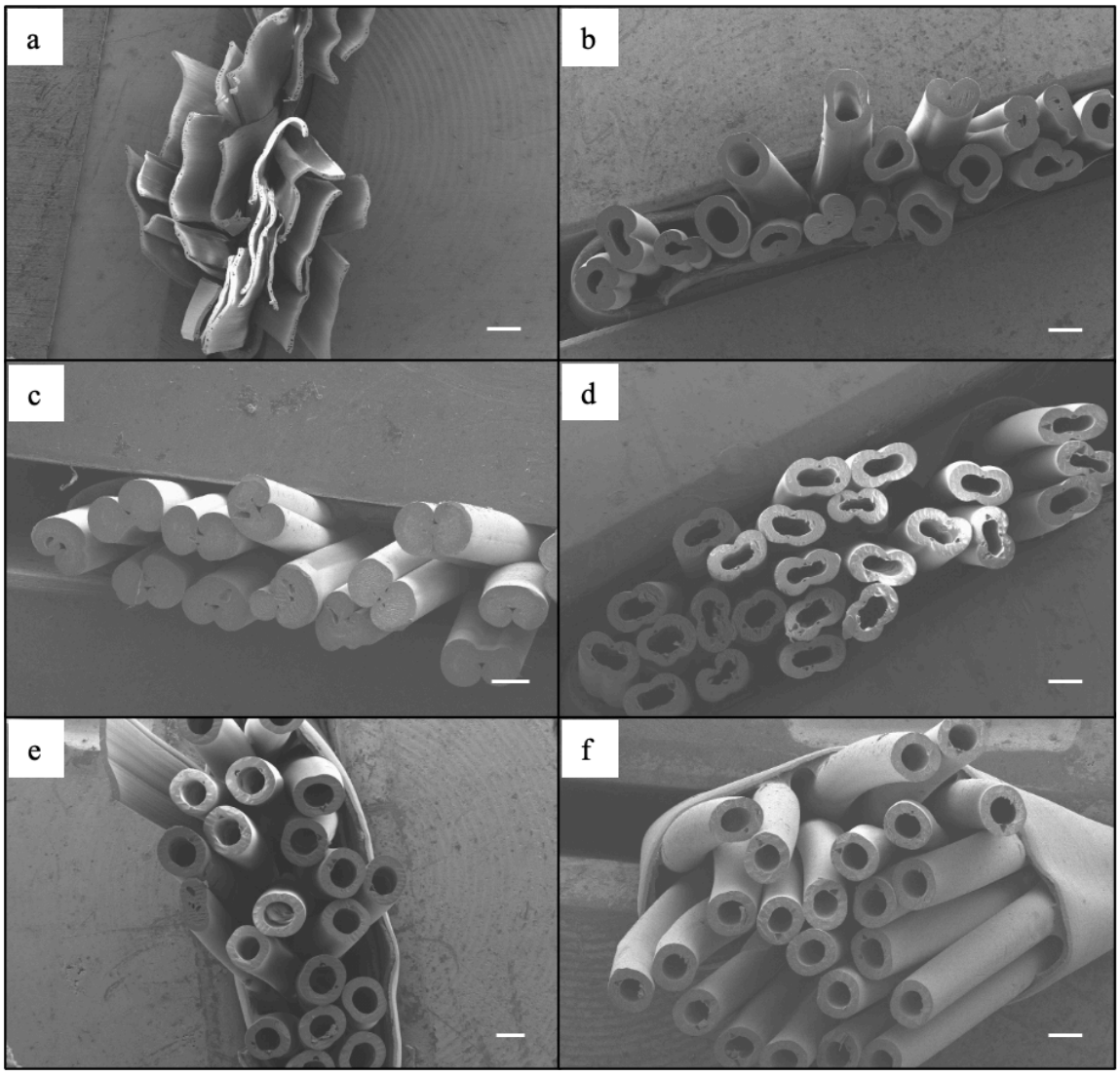

Figure 4.5. Examples of coagulated fiber cross sections from early HF spinning experiments. (a) run 419; (b) run 420; (c) run 423; (d) run 476; (e) run 478; (f) run 480. White calibration bars are 250 μm.

Table 4.2. The air gaps, flow rates, and draw down ratios (DDR) used in early attempts to produce HF.

Run	Air Gap (mm)	Flow Rate (mL/min)	Draw Down Ratio
419	6	4	5
420	8	4	0.8
423	10	8	3.5
476	8	8	1.68
478	8	4	1.68
480	8	4	1.84

$$\mathrm{DDR} = \frac{v_{y_0} A}{Q} \qquad \text{Eqn. 4.2}$$

Various fiber cross sectional shapes are shown in Figure 4.5. Figure 4.5a shows polymer "ribbons". These were attributed to the inability of the 2Cs of the segmented arc spinneret capillaries to heal, in the air gap, prior to entering the coagulation bath. The use of a high draw ratio (5x) in this case was hypothesized to hinder adequate time in the air gap for this healing to occur. Fibers shown in Figure 4.5b were spun using a 0.8x DDR and the resulting filaments varied greatly in cross sectional shape. Increasing draw ratio again to 3.5x, along with the air gap and flow rate, resulted in the production of lobed cross sections (Figure 4.5c). Figure 4.5d contained hollow filaments of somewhat regular cross section, however, they were non-circular and the "healing" line between the 2Cs was evident. Reducing the flow rate from 8 mL/min to 4 mL/min in Figure 4.5e and f allowed more time in the air gap for the healing of the 2Cs and resulted in mostly round, concentric HF.

Again, the fibers presented in Figure 4.5 represent a very small portion of the fibers initially spun and studied. In general, it was found that fibers spun using an 8 mm air gap, 4 mL/min flow rate, and approximately 1.8x DDR tended to produce round, concentric HF from the HF-A segmented arc spinneret. These HF spinning parameters served as a starting point for the experiments and results discussed in this chapter, which were completed in an effort to gain further insight into the HF development process.

4.3.2 Hollow fiber drawing process

Upon determining some initial parameters capable of producing hollow filaments, research focused on extending the spinning process beyond the coagulation bath, to include washing, stretching, drying, and take-up of the hollow filaments on a spool. Several spinning runs were completed, with samples taken at varying points in the spinning process. A 16 wt.% TechPAN1/DMSO dope was used, at a flow rate of 4 mL/min for all runs. Fiber outer diameter (OD) and inner diameter (ID) were measured and plotted in Figure 4.6 as a function of cumulative draw. The cumulative draw increases as fiber progresses down the spinning line through washing, stretching, drying, and final take-up on the spool. Solid symbols indicate measured OD, while open symbols indicate measured ID. Both ID and OD are shown to decrease with increasing cumulative draw, as expected. Fibers measuring 426 μm OD and 246 μm ID out of the coagulation bath were reduced to 158 μm OD and 108 μm ID at the spool after a cumulative draw of 7, a reduction of 63% and 56%, respectively. The smallest spooled fibers measured 73 μm OD and 43 μm ID after a cumulative draw of 30. In addition to the measured data, theoretical ID and OD prediction lines were developed based on an assumed constant fiber density, a constant 1.8 OD/ID ratio, and Eqn. 4.3, where $\emptyset_{OD_1}$ is the initial outer diameter and $\emptyset_{OD_2}$ is the outer diameter resulting after the application of a known cumulative draw.

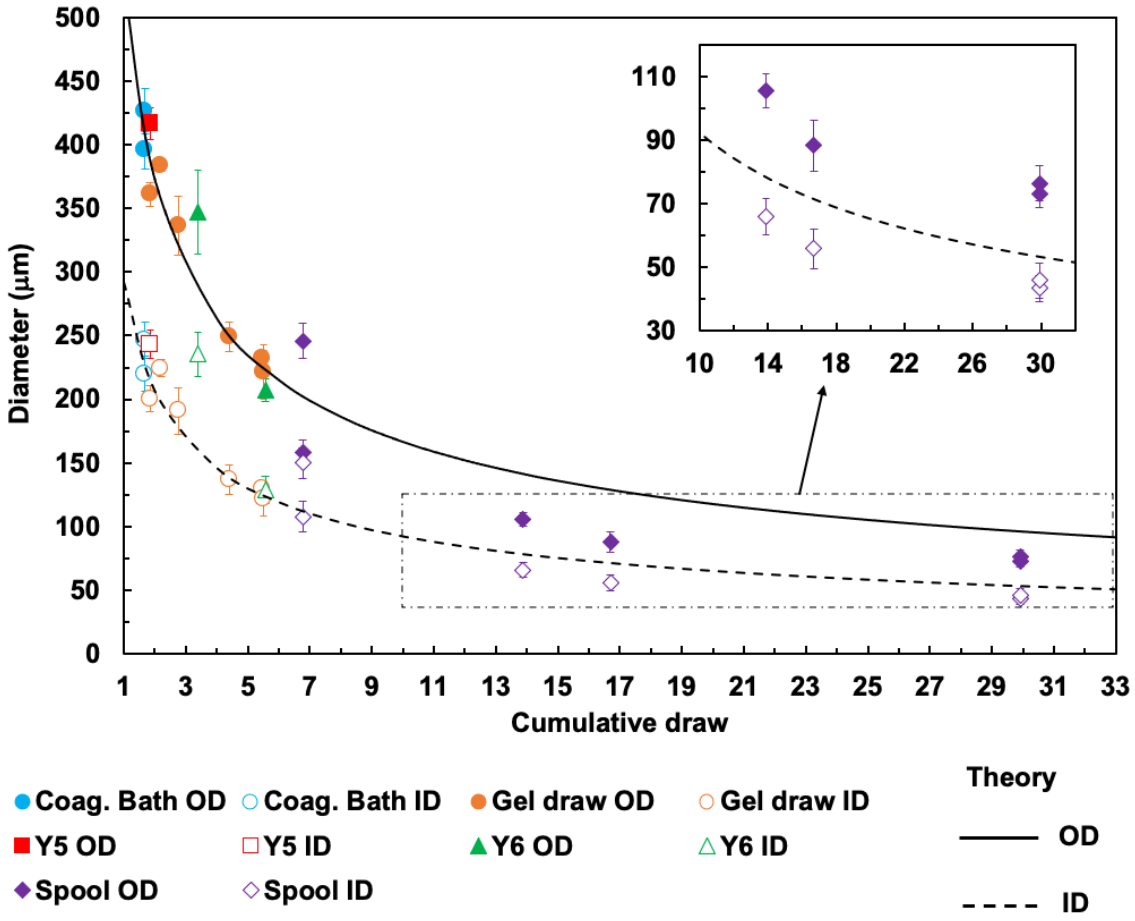

Figure 4.6. Hollow fiber inner and outer diameter for multiple similar spinning runs plotted as a function of cumulative draw attained along the spinning line. Theoretical predictions for outer diameter and inner diameter trends are indicated.

$$\emptyset_{OD_2} = \frac{\emptyset_{OD_1}}{\sqrt{\text{Cumulative Draw}}} \qquad \text{Eqn. 4.3}$$

The theoretical predictions for ID and OD hold well until reaching cumulative draws ≥ 7, at which point it appears that the assumed OD/ID ratio of 1.8 no longer holds and that some wall thinning occurs at high cumulative draws. This wall thinning was attributed to pore collapse within the polymer network, and therefore an increasing fiber density along the fiber spinning line. The cross section of spooled HF resulting from a cumulative draw of 30 are shown in Figure 4.7. It was particularly encouraging to observe that the filaments retained their hollow structure despite the rigors of the spinning process.

During the washing, and particularly during the stretching process for example, tension on the fiber tow can reach 100s of grams force. This was not, however, enough to collapse the fibers as they were wound on a core, and the fibers retained their hollow structure.

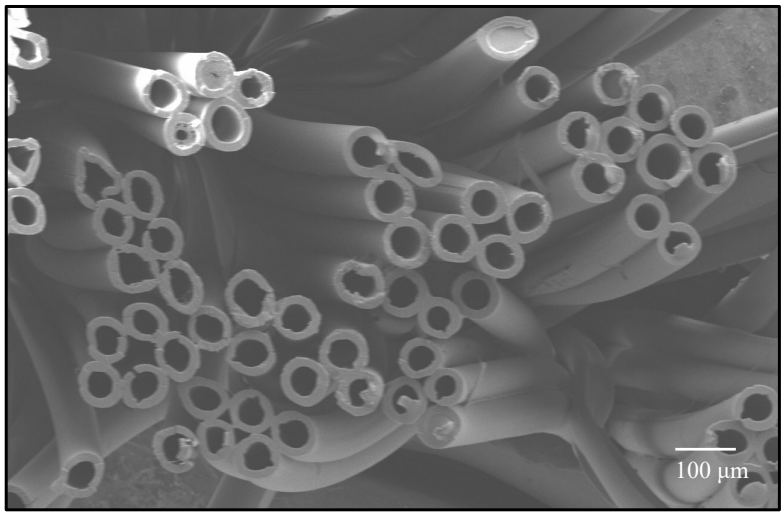

Figure 4.7. Cross section of spooled HF following cumulative draw down ratio of 30.

4.3.3 Hollow fiber morphology

While the initial parameters used to produce HF were adequate, undesirable fiber morphologies were observed. In Figure 4.8a, HF cross sections are shown which contain triangular or "heart-shaped" macrovoids (circled in red). These macrovoids are undesirable for producing high strength CF [19-21]. In addition, obvious inter-filament fusion is observed (circled in yellow). The results of this inter-filament fusion are shown in Figure 4.8b, where two previously fused filaments have begun to pull apart, resulting in damage to the surface of both fibers. This surface damage, in addition to the macrovoid presence, greatly reduces the tensile strength of fibers [19]. In Figure 4.8c, a close-up of a fiber cross section with a triangular macrovoid is shown, with some evidence in the fiber lumen of the fiber "wrinkling" or buckling around the macrovoid. When examining the lumen further (Figure 4.8d), more wrinkling was observed in isolated locations, suggesting pockets or macrovoids were lurking beneath the surface.

Initially, macrovoid formation was hypothesized to stem from the “healing” of the 2C segments. However, further investigation revealed that their location about the fiber cross section was random, rather than being located on opposite sides of the fiber, and that their number varied, with cross sections sometimes containing one, two, three, or more macrovoids. The second hypothesis was that these macrovoids were formed due to the use of a 100% water coagulation bath. When utilizing a 100% non-solvent bath (water, in this case), the polymer dope experiences an instantaneous phase change upon contact with the bath, forming a solid cuticle about the external surface of the fiber. Given the high density of this polymer cuticle, it can hinder further diffusion of non-solvent in and solvent out of the forming fiber. In addition, as this dual diffusion process is occurring, voids can be formed due to a rupture of this cuticle under pressure of the inward non-solvent diffusion [22]. Microscopic surface faults, such as those caused by spinneret imperfections, can make such rupture more likely [23]. Interestingly, Takahashi et al. found similar void structures formed when spinning solid filaments into a 100% water coagulation bath [24]. They observed voids to significantly decrease with increasing solvent content in the coagulation bath.

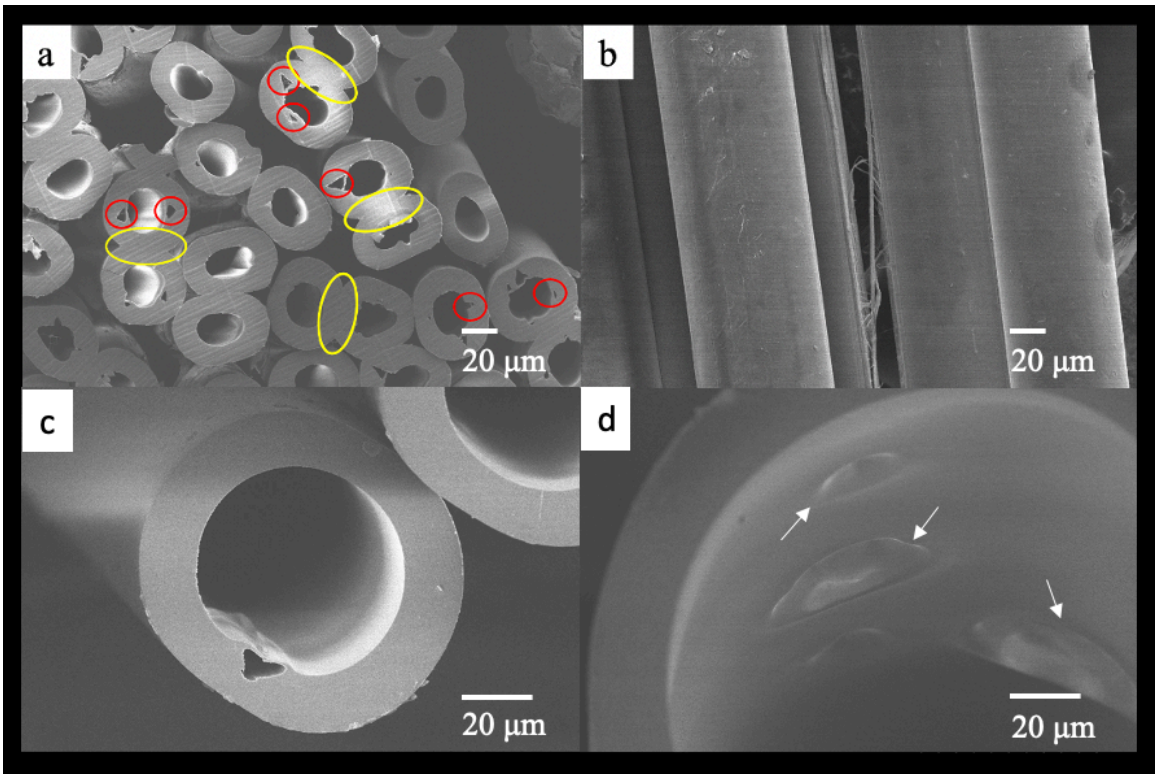

Figure 4.8. Fully drawn and spooled HF. (a) HF cross sections are shown which contain triangular or "heart-shaped" macrovoids (circled in red) and inter-filament fusion is observed (circled in yellow). (b) Two previously fused filaments have begun to pull apart, resulting in damage to the surface of both fibers. (c) A close-up of a fiber cross section with a triangular macrovoid. (d) Wrinkling was observed in the fiber lumen in isolated locations (indicated by white arrows), suggesting pockets or macrovoids were lurking beneath the surface.

4.3.4 Rheological and thermal analysis

One potential method available to hinder macrovoid formation is to increase the polymer solids content in the spinning dope. Increasing the solids content slows coagulation by hindering the dual diffusion process and allows for slightly more homogeneous structure formation [17, 18]. Initial spinning trials were completed using TechPAN1 polymer, with a M_w of 300,000 g/mol. Based on this M_w, spinning runs were completed with a 14-16 wt.% TechPAN1/DMSO polymer dope. TechPAN2, with similar comonomer content but a lower M_w was received later in the project and comparisons between the two polymers were completed.

Figure 4.9a shows the shear viscosity results at room temperature for 16 to 24 wt.% TechPAN2 (TP2) solutions in DMSO, compared to the incumbent 16 wt.% TechPAN1 (TP1)/DMSO solution which had been reliably used during initial spinning trials. The shear viscosity of the new TechPAN2 dope at 20 wt.% TP2/DMSO concentration was found to overlap very well with the 16 wt.% TP1/DMSO dope. The use of TechPAN2 enabled the production of higher solids content dopes due to its lower molecular weight compared to TechPAN1, while retaining the same spinnable shear viscosity.

Shear viscosity measurements were completed as a function of dope temperature, maintaining the shear rate at 1 s^{-1}. As shown in Figure 4.9b, the viscosities of the 20 wt.% TP2/DMSO and 16 wt.% TP1/DMSO solutions were quite similar, particularly at the typical 50 °C spinning dope temperature. Finally, differential scanning calorimetry (DSC) analysis of both neat polymers was completed. Differences in their exothermic reactions with temperature were not expected due to the similarities in the comonomer contents and, indeed, the results in Figure 4.9c indicate nearly overlapping exothermic reactions. From the results gathered and shown in Figure 4.9, it was found that a 20 wt.% TechPAN2/DMSO dope could offer a path toward reduced macrovoid content when compared to the previously spun 14 or 16 wt.% TechPAN1/DMSO dopes, while retaining spinnability.

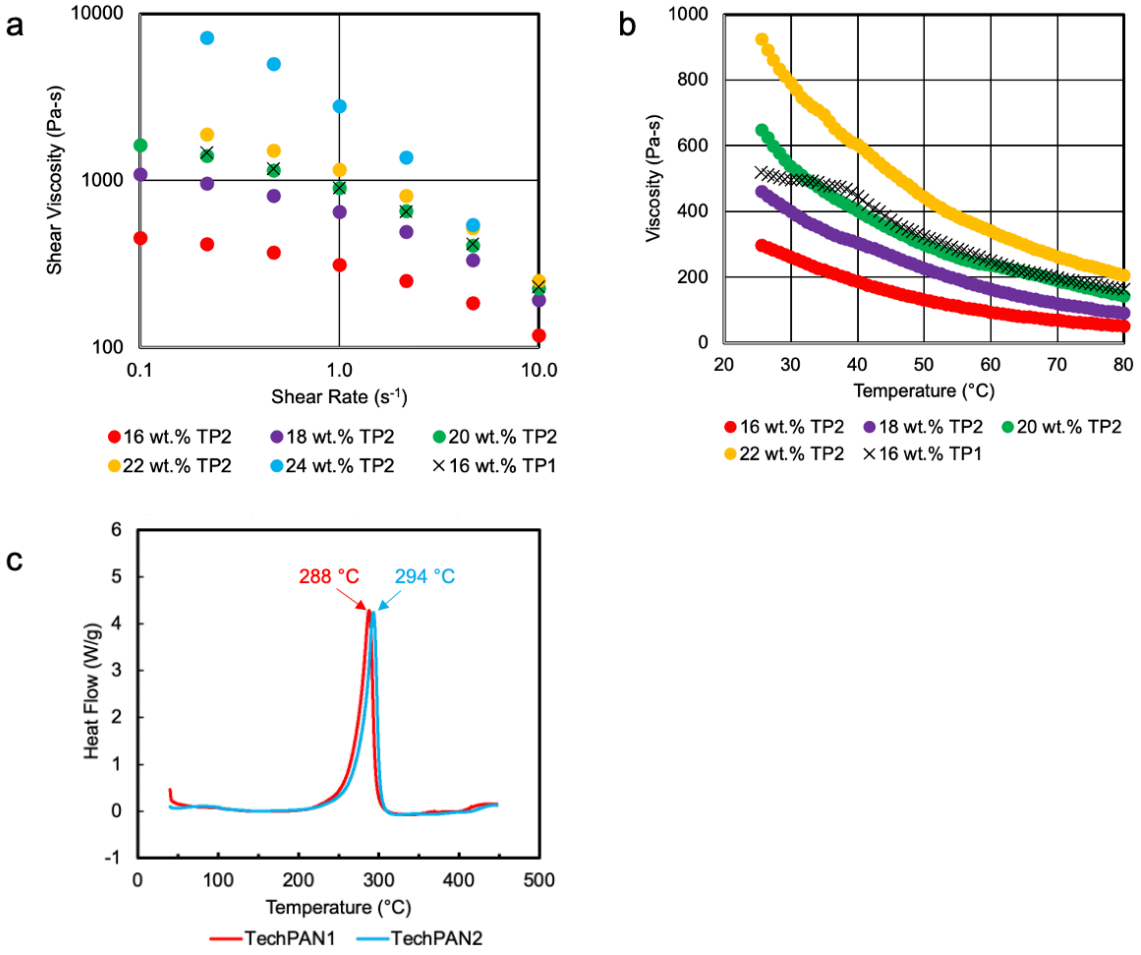

Figure 4.9. (a) Shear viscosity measurements at room temperature for 16 to 24 wt.% TechPAN2 (TP2) solutions in DMSO, compared to the incumbent 16 wt.% TechPAN1 (TP1)/DMSO. (b) Shear viscosity measurements as a function of dope temperature, maintaining the shear rate at 1 s^{-1}, again compared to the incumbent 16 wt.% TechPAN1 (TP1)/DMSO. (c) Differential scanning calorimetry (DSC) of neat TechPAN1 and TechPAN2 polymers.

To test the hypothesis that an increased dope polymer content would aid in the prevention of macrovoid formation, a 14 wt.% TechPAN1/DMSO and 20 wt.% TechPAN2/DMSO dope were each spun under the same conditions and their resulting HF compared. Samples were collected out of the coagulation bath, spun using the following conditions: 50 °C dope temperature, 8 mm air gap, 4 mL/min dope flow rate, and 100% water coagulation bath. The HF dimensions, including outer diameter, inner diameter, wall thickness, and percent open area are shown in Table 4.3. The fiber spun from the 20 wt.%

TechPAN2/DMSO solution had a slightly smaller OD and slightly larger ID, resulting in a thinner wall (48 μm) and larger percent open area (30.4%) compared to the TechPAN1 derived HF.

Table 4.3. Coagulated HF dimensions comparing HF spun from 14 wt.% TechPAN1/DMSO and 20 wt.% TechPAN2/DMSO solutions.

	Outer Diameter (μm)		Inner Diameter (μm)		Wall thickness (μm)		Open Area (%)	
	AVG	STDEV	AVG	STDEV	AVG	STDEV	AVG	STDEV
14 wt.% TP1/DMSO	230	10	114	7	58	2	24.7	1.2
20 wt.% TP2/DMSO	214	5	118	2	48	3	30.4	1.6

In a further comparison of the two fibers, scanning electron micrographs were collected of the fiber cross sections. In Figure 4.10a, the cross sections of HF derived from TechPAN1 can be found to contain a high number of macrovoids. On the contrary, in Figure 4.10b, the HF stemming from the TechPAN2 solution displayed a dramatically reduced macrovoid content. This is in agreement with the dimensional analysis as well, as the wall thickness was thinner for TechPAN2 derived fibers and the percent open area greater. Overall, these results indicate that the use of a 20 wt.% TechPAN2/DMSO dope produced fibers which had significantly reduced macrovoid content, smaller wall thickness (suggesting denser fiber structure), and greater percent open area over a 14 wt.% TechPAN1/DMSO. Therefore, the use of higher solid content in the spinning dope, with TechPAN2, presented a path forward for improving HF morphology by reducing the occurrence of macrovoids.

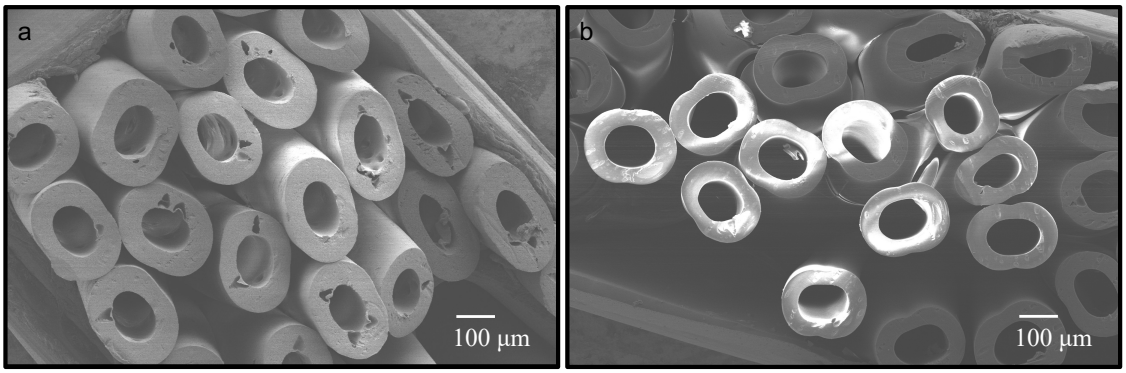

Figure 4.10. Scanning electron micrographs of coagulated HF cross sections, derived from: (a) 14 wt.% TechPAN1/DMSO and (b) 20 wt.% TechPAN2/DMSO dopes.

4.3.5 Wall thickness and characteristic time-scale in the air gap

With the ability to produce both coagulated and fully washed, stretched, and dried spooled hollow fiber established, it was decided to revisit the initial spinning parameters to better understand their dependencies and impact on the fiber morphology to make desired changes (reduced diameter, wall thickness, etc.). Utilizing spinneret HF-C, with smaller outer and inner capillary diameters, a 20 wt.% TechPAN2/DMSO dope was spun at 50 ºC with a DDR of 3 through the coagulation bath. To vary the time of a nascent fiber fluid packet in the air gap, the dope flow rate and the y_0 speed (see Figure 4.3) were increased while maintaining a DDR of 3 in the air gap. These parameters are shown in Table 4.4. Two runs were completed, one with a 6.5 mm air gap (run 520) and one with an 8 mm air gap (run 518). The fiber cross sections were measured and wall thickness determined for samples collected as time in air gap was varied. The results are plotted in Figure 4.12. Time in the air gap was calculated assuming constant acceleration in the air gap per Eqn. 4.4. In Eqn. 4.4, *t* is the time in the air gap, *s* is the air gap distance, *u* is the dope jet velocity exiting the spinneret and *v* is the y_0 godet speed, estimated as the final filament velocity upon entering the bath.

$$t = \frac{s}{0.5(u+v)} \qquad \text{Eqn. 4.4}$$

The HF-C spinneret possessed smaller outer and inner capillary diameters compared to HF-A but the same arc width (Table 4.1). As a result, the fibers produced using HF-C tended to have thicker walls compared to those produced from HF-A (fibers produced from HF-A are shown in Figure 4.7, for example). Interestingly, when analyzing results from spinning runs 520 and 518, which were spun using different air gaps, there was a local minima for both with regard to wall thickness, with the minimum wall thickness occurring with 0.33 s residence time in the air gap. It was hypothesized that when the dope flow rate and y_0 linear speeds were high, the dope would be quick to exit the capillaries, but the high flow rate through the capillary would result in higher shear rates and less time within the capillary, extending and aligning the polymer chains. As the dope exited the capillary, this stored elastic energy would be recovered and the exiting polymer solution would swell. Despite the high linear speed of the godet which would attempt to counter the viscoelastic

die swell, this may result in coalescence of the 2C segments with a thicker than desired wall thickness. Formation of a working hypothesis explaining what happened at low dope flow rates and low y_0 linear speeds to generate large wall thickness was more difficult. It is possible that the relatively large residence time in the air gap (0.42 s, for example) permitted the 2Cs to coalesce to produce a thicker than desired wall, as demonstrated in Figure 4.11. Further investigation is necessary to determine the cause for this local minima. If possible, die swell measurements may be helpful.

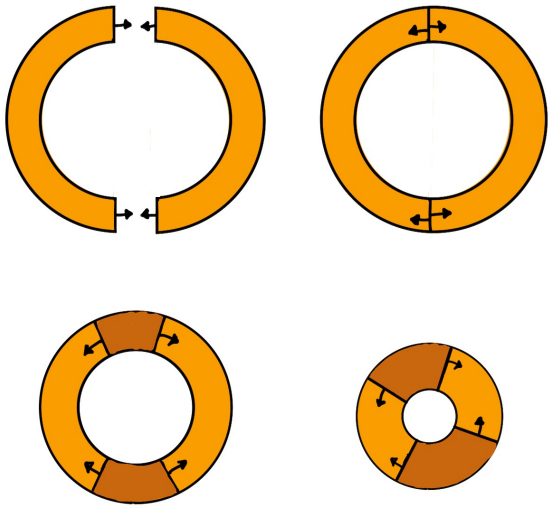

Figure 4.11. Hypothesized coalescence of the 2Cs during large residence times in the air gap, leading to a thicker than desired hollow fiber wall.

Despite not yet having a concrete causality behind the phenomenon, the results presented here indicated that it was possible to determine an appropriate balance between dope flow rate and godet linear speed to minimize the wall thickness by managing coalescence of the 2C segments, with results in this case indicating 0.33 s in the air gap to be appropriate for minimizing wall thickness, independent of air gap distance.

Table 4.4. Parameters utilized in the collection of coagulated fibers from runs 518 and 520, including methods for varying flow rate and y_0 linear speed to maintain a constant draw ratio (DDR) of 3.

DDR	Dope Flow Rate (mL/min)	y_0 Linear Speed (m/min)	Time in air gap (s)	
			Run 520 (6.5 mm Air Gap)	Run 518 (8 mm Air Gap)
3	1.4	1.38	0.42	0.52
3	1.6	1.58	0.37	---
3	1.8	1.78	0.33	0.41
3	2.0	1.98	0.30	0.37
3	2.2	2.17	0.27	0.33
3	2.4	2.37	0.25	0.30

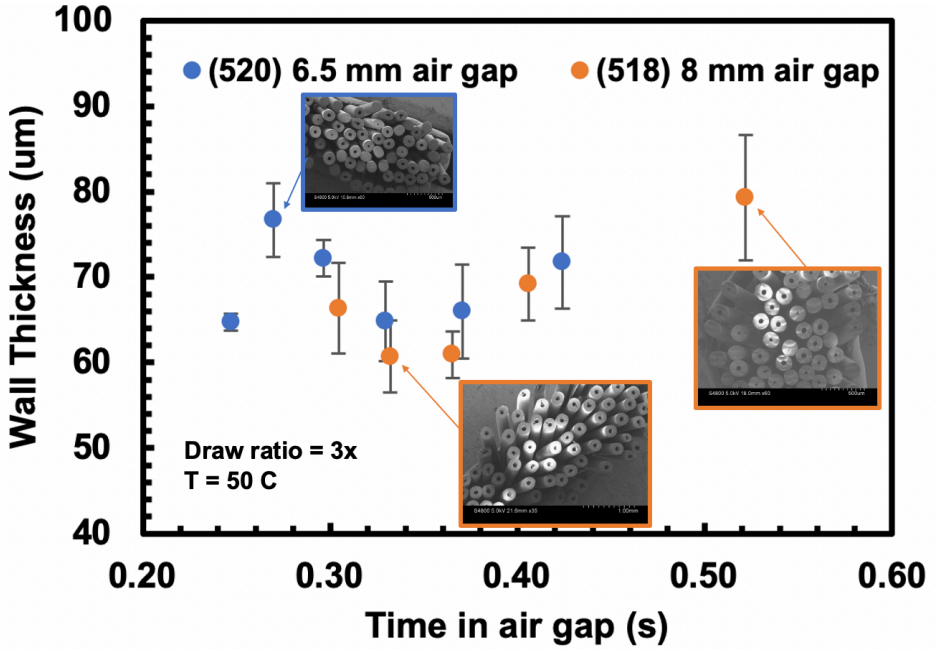

Figure 4.12. Wall thicknesses for HF spun with varying time in the air gap, with a draw ratio of 3 kept constant by increasing dope flow rate and increasing y_0 godet speed out of the coagulation bath.

4.3.6 Residual liquid content

Thus far, the use of a higher solids content dope (20 wt.% TechPAN2/DMSO) aided in the reduction of macrovoid formation, which was hypothesized to stem from the use of a 100% water coagulation bath (as found by other researchers [24]). While a reduction in macrovoid frequency was observed, issues with a 100% water coagulation bath remained.

As stated previously, the formation of a polymer cuticle due to instantaneous coagulation in the 100% non-solvent bath hinders the dual diffusion process, and the effects of this were observed in the resulting fibers. Interestingly, when observing the HF with optical microscopy, liquid was found to exist in the lumen of the dried and spooled fiber, as shown in Figure 4.13, indicated by the menisci (solid bands). This liquid was observed to move within the fiber as the fiber was repositioned under the microscope. This result indicated that the HF was not sufficiently dried despite drying prior to take-up. Difficulties with the removal of trapped liquid from the fiber interior during washing and drying were hypothesized to stem from hindered diffusion caused the dense external cuticle layer.

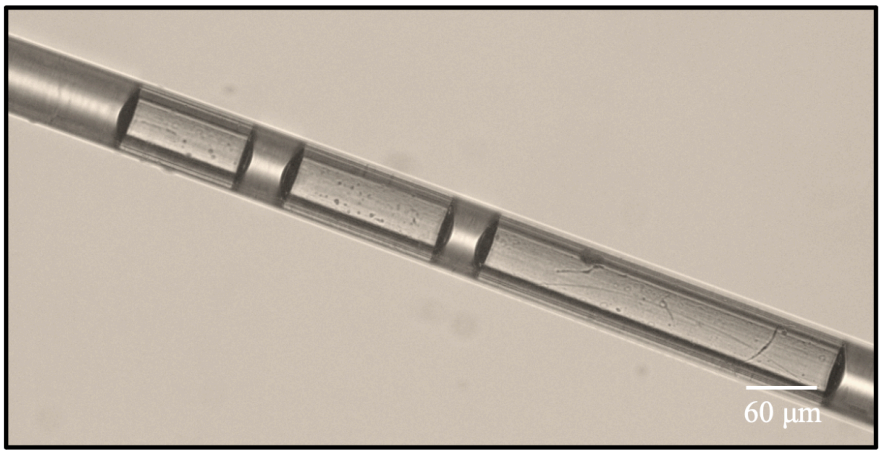

Figure 4.13. Optical micrograph of a hollow filament showing trapped liquid within the fiber.

To determine the amount of liquid persisting in the spooled fiber, thermogravimetric analysis (TGA) was completed. It was hypothesized that the liquid consisted of a mixture of solvent and non-solvent, or DMSO and water in this case. Benchmark mixtures were prepared in addition to neat DMSO and water to observe their weight change as a function of temperature. The resulting curves are shown in Figure 4.14a. Despite a 100 °C boiling point for water and a 189 °C boiling point for DMSO, the TGA curves of their mixtures smoothly decreased with temperature. There were no clear changes in the rate of weight loss with temperature for water, DMSO, or their mixtures (6.1, 50, and 94.4 wt.% DMSO/water), likely due to the hydrogen bonding which occurs between the two. Based

on the results, the liquid would need to be treated as some unknown concentration of DMSO/water during TGA analysis.

Several spooled hollow fibers, as well as a commercially produced precursor (as a benchmark) were analyzed and their resulting curves are shown in Figure 4.14b, with their corresponding weight losses shown in Table 4.5. Interestingly, all hollow fibers show a two-step weight loss up to 275 °C. It was hypothesized that the initial weight loss was attributed to free liquid within the fiber, such as liquid stored in the fiber lumen, which would behave similarly to the liquids in Figure 4.14a. The second weight loss was attributed to liquid interacting with the polymer network, which would therefore take more energy to liberate compared to the free liquid. Therefore, total liquid content was determined by measuring the weight change from 35 to 275 °C. While the benchmark commercial precursor contained 0.8 wt.% residual liquid, HF residual liquid content varied from 6.8 wt.% up to 25.8 wt.%. Variations in the HF residual liquid content were hypothesized to be related to differences in their spinning conditions, which will be discussed later. Wei et al. found that when spinning into a ~ 50 wt.% DMSO/water bath, solid fibers analyzed via TGA contained > 20 wt.% residual DMSO, albeit without the rigorous in-line washing used in this study [16]. Similarly, this was attributed to the quick formation of polymer cuticle which limited the outward diffusion of DMSO. Removal of residual liquid (and in particular residual solvent) is vital to the production of high tensile property CF as residual solvent acts as an impurity during thermal treatment and contributes to discontinuities in ladder polymer formation [25], imperfect crystalline structure [26], and fiber breakage. Therefore, residual solvent in the spun fiber should be < 0.5 wt.% [25].

Given the rather high residual liquid contents shown in Figure 4.14b, further experimentation was completed in an attempt to remove the residual liquid. In Figure 4.14c, a 30 cm continuous length of 497D HF tow was sampled from the fiber spool and washed for one hour while stirring in water. Following washing, TGA was completed and the total residual liquid content reduced from 25.8 to 15.0 wt.%. For comparison, spooled 497D fiber was chopped into ~ 1 mm length pieces and similarly washed in water for one

hour. As a result, residual liquid content was drastically reduced from 25.8 to 0.8 wt.%. Table 4.6 shows the weight losses for the washed fibers relative to the spooled fiber.

The drastic drop in residual liquid content following chopping of the fiber compared to washing a continuous length indicated that chopping provided more surface area on which washing and extraction of residual liquid could occur, and that this extraction was hindered in the continuous length by the presence of the dense cuticle, similar to what other researchers have found. This finding suggests that washing alone during spinning will not be adequate for the removal of this amount of residual liquid, as even the best washing procedures have a residence time on the order of minutes, not hours. Therefore, changes to the spinning method must be considered which can prevent the formation of the dense cuticle in order to allow dual diffusion and appropriate washing to residual solvent content to < 0.5 wt.%.

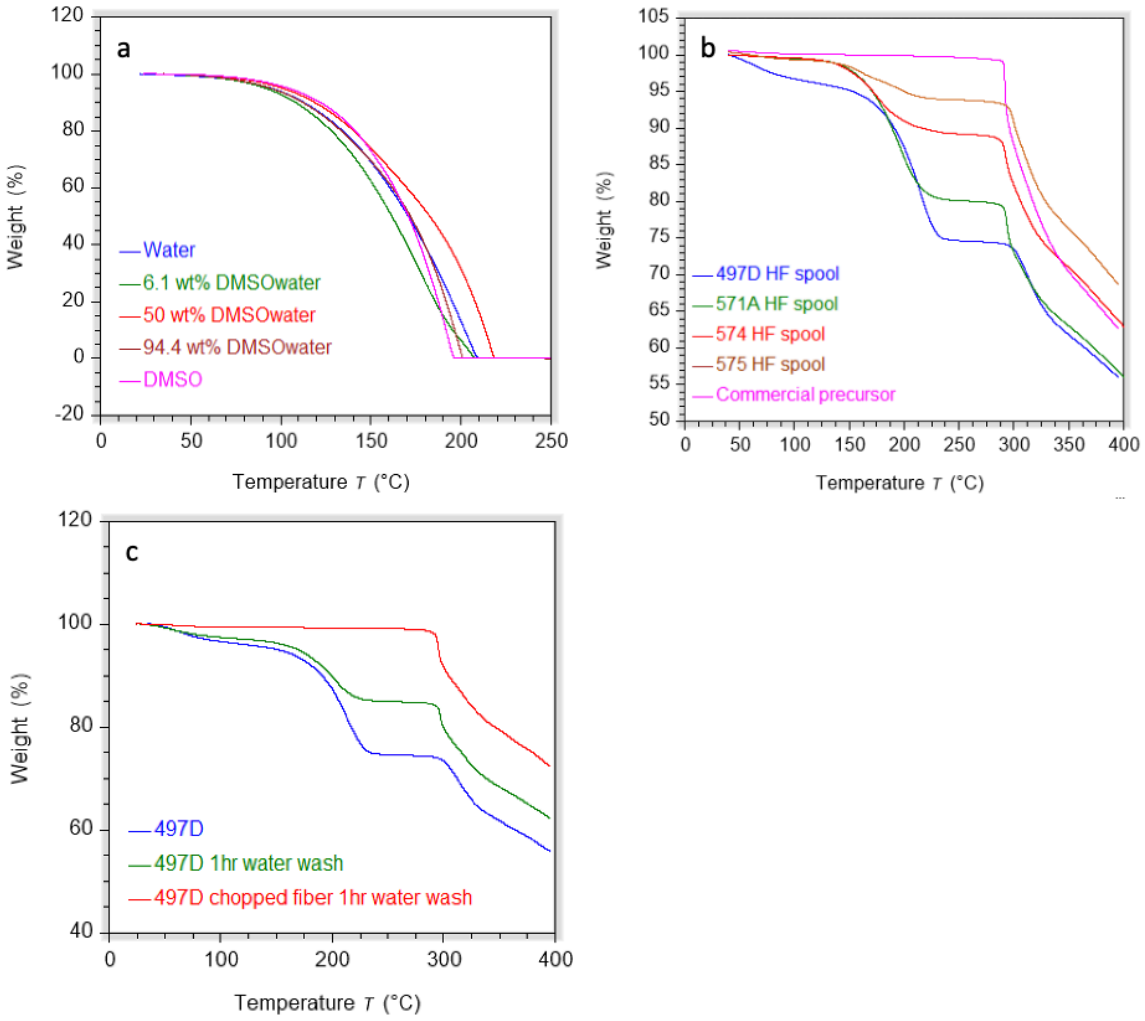

Figure 4.14. (a) TGA analyses of DMSO/water benchmark mixtures. (b) TGA analyses of various spooled HF to determine residual liquid contents, compared to a benchmark commercial solid precursor fiber. (c) TGA analyses of 497D HF off the spool for residual liquid content compared to 497D fiber after a 1 hr. water wash of a continuous 30 cm length and 1 mm chopped fibers.

Table 4.5. Weight loss attributed to residual liquid content within the HF for several HF and a commercial solid precursor fiber benchmark.

Precursor Fiber	35 to 200 °C Wt. Loss (%)	200 to 275 °C Wt. Loss (%)	Total Weight Loss (%)
497D	12.9	12.9	25.8
571A	13.6	6.1	19.7
574	8.8	2.0	10.8
575	5.4	1.4	6.8
Commercial	0.4	0.4	0.8

Table 4.6. Weight loss attributed to residual liquid content within the HF from run 497D, including weight losses for 497D spooled fiber, 497D fiber after washing a continuous length in water, and 497D fiber after chopping and washing in water.

Precursor Fiber	35 to 200 °C Wt. Loss (%)	200 to 275 °C Wt. Loss (%)	Total Weight Loss (%)
497D	12.9	12.9	25.8
497D Cont. Wash	10.1	5.0	15.0
497D Chop Wash	0.8	0.3	1.1

4.3.7 Solvent-assisted coagulation

Armed with an improved understanding of the critical HF formation variables (for example, air gap, dope flow rate, dope polymer content, and time in the air gap) and the knowledge that a 100% water coagulation bath remained detrimental to HF formation, it was decided to revisit the coagulation bath composition. Here, the goal was to determine if more gradual changes to the coagulation bath composition could be made to prevent the quick formation of the polymer cuticle during rapid coagulation, which had thus far been found to encourage macrovoid formation and trap residual liquid within the HF. Spinning experiments were completed utilizing a 10, 20, and 30 wt.% DMSO/water coagulation bath (corresponding to runs 571A, 574, and 575, respectively). All runs utilized a 20 wt.% TechPAN2/DMSO dope (which had been previously shown to reduce macrovoid formation relative to 14 wt.% TechPAN1/DMSO), 75 °C dope temperature, 4 mL/min flow rate, 8 mm air gap, and a total draw ratio of 30 from spinneret to spool. The resulting spooled HF from all three runs were concentric and hollow. An example of the HF produced from run 575 (30 wt.% DMSO/water coagulation bath) is shown in Figure 4.15.

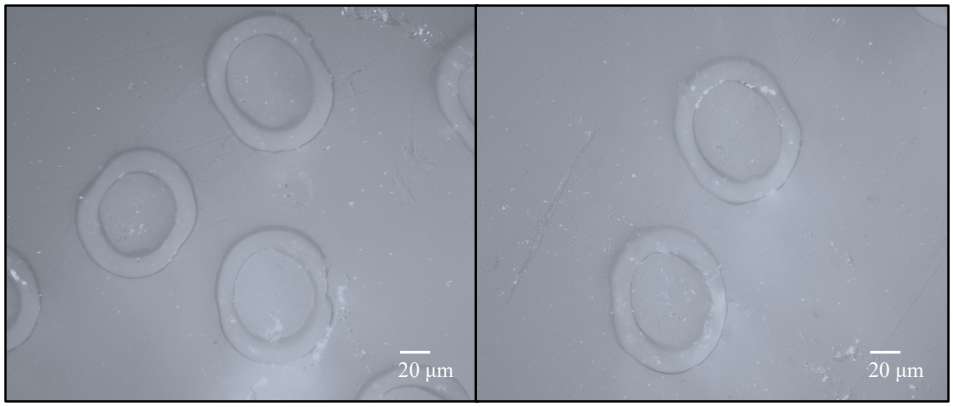

Figure 4.15. Optical micrographs of cross sections of HF spun into 30 wt.% DMSO/water coagulation bath (run 575), captured at 500x (reflected light in oil).

In addition to successfully retaining their hollow structure when spun into a bath containing a low amount of solvent (10 to 30 wt.% DMSO/water), recall from Figure 4.14b that several spooled HF contained decreasing amounts of residual liquid when compared to 497D HF, which was spun into a 100% water coagulation bath and contained 25.8% residual liquid (Table 4.5). Runs 571A, 574, and 575 were included in that TGA analysis (spun using 10, 20, and 30 wt.% DMSO/water coagulation baths, respectively) and contained 19.7, 10.8, and 10.3% residual liquid, respectively. Here, increasing the coagulation bath solvent content aided in the reduction of residual liquid content in the final fiber. Although far from the target of < 0.5 wt.% residual solvent content, the results indicated that the HF spinning process was moving in the right direction and further increases to the coagulation bath solvent composition concentration should be attempted.

4.3.8 Tensile properties

Tensile analysis of HF precursors was completed for spooled HF of varying outer diameter (497A, 497B, 497C, and 497D) which represented spooled fiber of increasing draw ratios from run 497 (spun using 16 wt.% TechPAN1/DMSO and a 100% water coagulation bath). A spool of 25 filament HF precursor tow, with inset scanning electron micrograph of a representative HF precursor cross section is shown in Figure 4.16. Their respective draw ratios, inner and outer diameters, and effective densities (Eqn. 3.1) are shown in Table 4.7. The effective tensile properties are shown in Figure 4.17a and b and

contain the effective tensile strengths and effective elastic moduli for the 497A, 497B, 497C, and 497D samples (navy open circles), as well as the *specific* effective properties (specific effective strength and specific effective modulus in the green open circles). The solid circles in Figure 4.17a and b represent tensile properties and diameters of solid precursor PAN fiber spun in-house from the same polymer (10.5 μm diameter, 600 MPa tensile strength, 14 GPa modulus, and 1.18 g/cc density).

In the HF, both effective tensile strength and modulus increase with decreasing fiber outer diameter, and trend toward the properties of the baseline solid fiber. Reductions in precursor fiber dimensions facilitate improved tensile strength due in part to a reduction in the volume per unit length in which voids or other defects can exist. Increases in fiber modulus in this case are attributed to the increased draw ratios utilized to produce the precursor filaments, which imparts higher molecular orientation to the fibers. Overall, this data suggested that further decreasing in HF precursor diameters would result in the achievement of solid precursor properties, but with a lower effective density. This is, of course, the ultimate goal in the resulting HCF.

Figure 4.16. A spool of 25 filament HF precursor tow, with inset scanning electron micrograph of a representative HF precursor cross section.

Table 4.7. Draw ratios used to produce the precursor HF during run 497, as well as the resulting precursor HF dimensions and effective densities.

Precursor Fiber	Draw Ratio	Outer Diameter (μm)	Inner Diameter (μm)	Effective Density (g/cc)
497A	5	215	153	0.58
497B	12	101	61	0.75
497C	27	58	33	0.8
497D	32	56	32	0.8

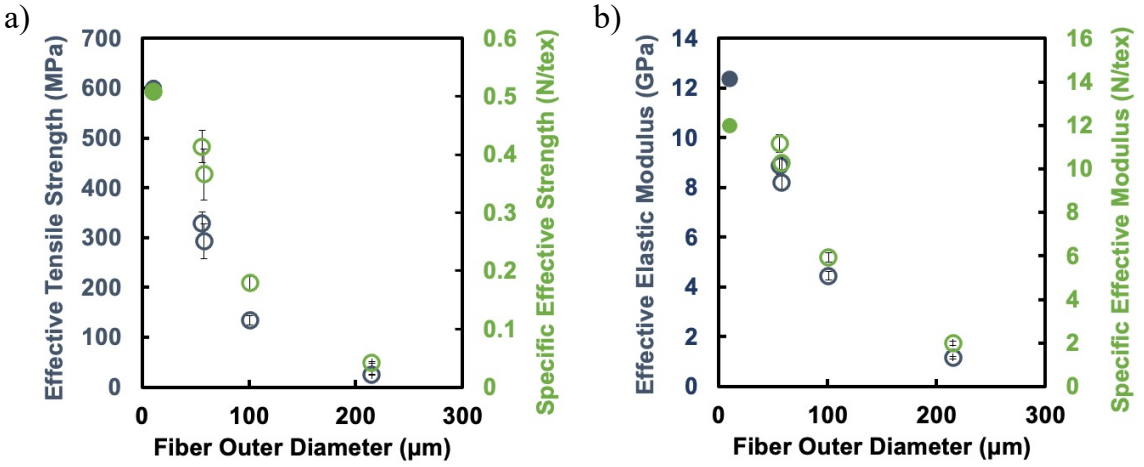

Figure 4.17. Hollow precursor fibers 497A, B, C, and D a) effective tensile strength and specific effective tensile strength as a function of outer diameter and b) effective elastic modulus and specific effective modulus as a function of the fiber outer diameter, compared to a solid precursor fiber. From the author's original work [27], reprinted with permission.

4.4 Conclusions

Prior to this study, little research had been completed on the use of multifilament segmented arc spinnerets for solution spinning PAN precursors. **It was hypothesized that a segmented arc spinneret could be used to produce HF precursors with dimensions and morphology appropriate to the production of high tensile property HCF.** This chapter reported on investigations of the spinning process and the resulting HF precursors and included observations regarding coagulation, fiber drawing, and tensile properties. Several significant findings were gathered. First, contrary to traditional solid precursor spinning, a high solvent content coagulation bath was initially

detrimental to HF formation. It was hypothesized that the high solvent content coagulation bath and resulting slow coagulation allowed for the collapse of the 2C segments and the formation of a relatively solid, macrovoid-filled fiber. To prevent this collapse, a 100% non-solvent (water) bath was utilized which led to the rapid outward diffusion of non-solvent, resulting in the instantaneous precipitation of the polymer. This rapid precipitation led to a dense cuticle formation on the surface of the fiber, which was hypothesized to aid in preserving the lumen of the nascent, healed 2C segments during fiber formation, resulting in a concentric HF. The use of a 100% water coagulation bath allowed for the preliminary study of other vital spinning parameters, including air gap, dope flow rate, and time in the air gap.

However, while valuable in helping to establish initial HF spinning parameters, the use of a 100% water coagulation bath was ultimately found to be detrimental to HF formation for a few reasons. First, fibers spun into a 100% water coagulation bath contained high amounts of residual liquid, known to be detrimental to CF development. This was attributed to the fast coagulation that occurred in the water bath, which created a thin polymer cuticle on the exterior of the fiber, hindering the dual diffusion process and resulting in high residual liquid contents in the fiber. Second, fibers spun into a 100% water coagulation bath contained macrovoids. It was hypothesized that macrovoid formation occurred due to breaks in the cuticle during coagulation which allowed a rapid influx of fluid.

While the use of a 100% water coagulation bath was found to not be ideal, it permitted the study of other spinning variables while producing HF. For example, it was found that by increasing the polymer content in the spinning dope, macrovoid formation could be drastically reduced. Upon developing a better understanding of the interactions between spinning variables which resulted in improved HF spinning process stability, slight increases to the coagulation bath solvent content were completed, and resulted in the formation of HF with little to no macrovoids and a notable decrease in residual liquid content. Of utmost importance in this study was the ability of the HF to retain their hollow structure despite the rigors of the spinning, washing, stretching, and drying processes. The tensile properties of PAN HF precursors produced in this study indicated a steady trend

toward traditional solid fiber properties as HF dimensions are reduced, and are expected to exceed those of traditional solid fibers particularly in terms of specific effective properties owing to the reduced effective density of the HF. Achieving this in the resultant HCF centrally motivated this work. Overall, these findings illustrate the significant feasibility of producing multifilament PAN HF from a segmented arc spinneret toward the production of hollow carbon fibers for structural applications.

4.5 Future Work

This work has opened the door to study of HF development from a segmented arc spinneret and there remains much to be examined. For example, increases to the coagulation bath composition ended with a maximum bath composition of 30 wt.% DMSO/water. Given the improved control and understanding of other important spinning variables developed in this study, can the coagulation bath solvent concentration be increased further and what are the impacts of this increase on HF formation? How can residual liquid within the HF fiber be minimized, targeting < 0.5 wt.%? Will future spinneret designs with smaller inner/outer diameters and arc slip thicknesses enable the production of HF with reduced OD and wall thickness? Is it possible to achieve and exceed the specific effective tensile properties of traditional solid precursors using this HF technology? These are a just a few of the questions that remain surrounding this new frontier in PAN fiber development.

4.6 References

1. M.A. Rahman, A.F.I., A. Mustafa, B.C. Ng, H. Hasbullah, M.S.A. Rahaman and M.S. Abdullah, *The Effect of Coagulation Bath Temperature on the Mechanical Properties of PAN-based Carbon Fiber.* p. 169-179.
2. S.J. Law, S.K.M., *Investigation of Wet-Spun Acrylic Fiber Morphology by Membrane Technology Techniques.* Journal of Applied Polymer Science, 1996.
3. Juan Chen, C.W., Heyi Ge, Yujun Bai, Yanxiang Wang, *Effect of Coagulation Temperature on the Properties of Poly(acrylonitrile-itaconic acd) Fibers in Wet Spinning.* J. Polym. Res., 2007. **14**: p. 223-228.
4. A.K. Gupta, D.K.P., Pushpa Bajaj, *Acrylic Precursors for Carbon Fibers.* Journal of Macromolecular Science, 1991. **C31**(1): p. 1-89.
5. Ju, A., S. Hou, Y. Pan, Y. Wang, Y. Zhu, and H. Chen, *Preparation of hollow carbon submicro-fibers with controllable wall thicknesses from acrylonitrile copolymer.* Textile Research Journal, 2017. **88**(16): p. 1893-1901.

6. Shim, H.B., J.I. Lee, H.S. Kim, Y.J. Choe, and B.S. Rhee. *On hollow and C-type carbon fiber reinforced composite materials*. in *International Conference on Advanced Composite Materials (ICACM)*. 1993.
7. Noland, R.L. and T.D. O'Brien, Hollow carbon fibers. U.S. Patent 5,338,605. August 16, 1994.
8. Thewlis, R., *The spinning of hollow polyacrylonitrile fibres as a precursor for the formation of hollow carbon fibres*. 1998, University of Strathclyde.
9. Ferguson, J., Apparatus and method for spinning hollow polymeric fibres. U.S. Patent 6,143,411. November 7, 2000.
10. Liu, Y., H.G. Chae, Y.H. Choi, and S. Kumar, *Preparation of low density hollow carbon fibers by bi-component gel-spinning method.* Journal of Materials Science, 2015. **50**(10): p. 3614-3621.
11. Gulgunje, P.V., B.A. Newcomb, K. Gupta, H.G. Chae, T.K. Tsotsis, and S. Kumar, *Low-density and high-modulus carbon fibers from polyacrylonitrile with honeycomb structure.* Carbon, 2015. **95**: p. 710-714.
12. Zhang, X., Y. Wen, Y. Yang, and L. Liu, *Effect of air-gap distance on the formation and characterization of hollow polyacrylonitrile (PAN) nascent fibers.* Journal of Macromolecular Science, Part B, 2008. **47**(6): p. 1039-1049.
13. Choi, Y.H., S. Han, and C.H. Choi, Preparation method for hollow carbon fiber. U.S. Patent 9,109,305. August 18, 2015.
14. Longming, W., Y. Yang, and X. Lianghua, *Formation mechanism of PAN hollow fiber prepared by wet spinning process.* China Synthetic Fiber Industry, 2012. **35**(1): p. 26-30.
15. Morris, E.A., M.C. Weisenberger, and G.W. Rice, *Properties of PAN fibers solution spun into a chilled coagulation bath at high solvent compositions.* Fibers, 2015. **3**(4): p. 560-574.
16. Wei, H.Q., X.D. Suo, C.X. Lu, and Y.D. Liu, *A comparison of coagulation and gelation on the structures and stabilization behaviors of polyacrylonitrile fibers.* Journal of Applied Polymer Science, 2020. **137**(19): p. 48671.
17. Knudsen, J.P., *The influence of coagulation variables on the structure and physical properties of an acrylic fiber.* Textile Research Journal, 1963. **33**: p. 13.
18. Stoyanov, A., *Influence of the content of polymer with different molecular weights in spinning solutions on properties of acrylic fibers.* Journal of Applied Polymer Science, 1982. **27**(1): p. 235-238.
19. Johnson, J.W. and D.J. Thorne, *Effect of internal polymer flaws on strength of carbon fibres prepared from an acrylic precursor.* Carbon, 1969. **7**(6): p. 659-661.
20. Liu, J., Z. Yue, and H. Fong, *Continuous nanoscale carbon fibers with superior mechanical strength.* Small, 2009. **5**(5): p. 536-42.
21. Kaur, J., K. Millington, and S. Smith, *Producing high-quality precursor polymer and fibers to achieve theoretical strength in carbon fibers: A review.* Journal of Applied Polymer Science, 2016. **133**(38).
22. Grobe, V. and K. Meyer, Faserforschung und Textiltechnik, 1959. **10**: p. 214-224.
23. Craig, J.P., J.P. Knudsen, and V.F. Holland, *Characterization of acrylic fiber structure.* Textile Research Journal, 1962. **32**(6): p. 435-448.
24. Takahashi, M., Y. Nukushina, and S. Kosugi, *Effect of fiber-forming conditions on the microstructure of acrylic fiber.* Textile research journal, 1964. **34**(2): p. 87-97.

25. Rajalingam, P. and G. Radhakrishxan, *Polyacrylonitrile Precursor for Carbon Fibers.* Journal of Macromolecular Science, Part C: Polymer Reviews, 1991. **31**(2-3): p. 301-310.
26. Wang, M., Y. Xiao, W. Cao, N. Jiao, W. Chen, and L. Xu, *SAXS and WAXD study of periodical structure for polyacrylonitrile fiber during coagulation.* Polymers for Advanced Technologies, 2015. **26**(2): p. 136-141.
27. Morris, E.A., R. Sarabia-Riquelme, N. Hochstrasser, J. Burgess, A.E. Oberlink, D.L. Eaton, and M.C. Weisenberger, *Early development of multifilament polyacrylonitrile-derived structural hollow carbon fibers from a segmented arc spinneret.* Carbon, 2021. **178**: p. 223-232.

CHAPTER 5. THE OXIDATION OF HOLLOW PAN PRECURSOR FIBERS

5.1 Introduction

As described earlier, three primary reactions occur during oxidative stabilization: cyclization, dehydrogenation, and oxidation. These result in the widely accepted chemical structure for fully oxidatively stabilized PAN, generally depicted in Figure 5.1 [1]. It is known, however, that these reactions occur to varying extents in the core of the fiber. To produce homogeneous oxidized cross section, an oxygen characteristic diffusion length exists, along which oxygen must diffuse to reach the fiber core and completely oxidize the fiber. For a solid fiber, the oxygen characteristic diffusion length is equal to the fiber radius (see Figure 2.1). However, oxygen diffusion to the fiber core is hindered by the continual formation of oxidized material near the fiber surface, which functions as a strong barrier to O_2 diffusion [2]. This results in the formation of the skin-core morphology, which is carried over into the final CF.

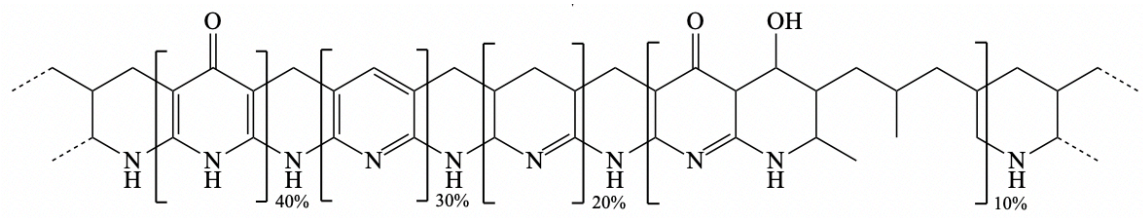

Figure 5.1. General chemical structure for fully oxidatively stabilized PAN. Adapted from [1] with permission from Elsevier.

The production of HF for structural HCF applications is largely unexplored and as a result the chemical and structural characterization of oxidized HF has also remained largely unstudied. However, several characterization techniques have been applied to solid oxidized PAN fiber, including EDX [3], X-ray spectroscopy [4], and Raman spectroscopy [5], to name a few. Differences between the chemical and structural features of the oxidized solid fiber skin and core have also been observed using optical microscopy. When imaged using optical microscopy, the skin appears brighter or of higher reflectance compared to the darker core [6]. This has been attributed to the formation of polycyclic aromatic

structures in the skin, which are known to exhibit higher reflectance [7]. The use of this technique may be useful for discerning the skin and core regions in an oxidized HF.

Characterization of the chemical structures in the oxidized PAN fibers is vital to the development of high tensile property CF because the chemical structures are responsible for differences in fiber morphology and therefore fiber properties. For example, density is closely associated with the chemical transformations from linear to ladder polymer by cyclization and with crosslinking by oxidation [5], all of which contribute to the development of compact structures [6, 8]. In fact, fiber density has been shown to track linearly with oxygen content, as oxygen diffuses in and is chemically incorporated into the stabilized PAN fiber [5, 6]. Both density and oxygen content targets exist for the production of stabilized fibers. These targets have been primarily established through empirical data, in which oxidized fibers of varying density and oxygen content were carbonized. The density and oxygen contents of the oxidized fibers which produced the highest tensile property CF were recommended as targets. Stabilized fiber oxygen contents ranging from 10-12 wt.% have been suggested for the production of high-quality CF [9-14]. The corresponding desired density range for stabilized fibers is generally 1.34 to 1.39 g/cc [15].

Attaining the desired density requires stabilization in an oxygen containing atmosphere. When fiber is stabilized in the absence of oxygen, fiber density increases at a slower, non-linear rate compared to fiber stabilized in an oxygen containing atmosphere and does not attain the targeted final density [5, 16]. Given that the stabilized fiber core is often oxygen “starved” compared to the skin, the density of the oxidized fiber skin is known to be higher than the core [17, 18]. Overall, due to its correlation with oxygen content and relative ease of measurement, density has been found to be a good indicator of the extent of stabilization for oxidized fibers [19, 20].

In Chapter 4, a process was described to obtain multi-filament hollow PAN precursor tow with round filaments, concentric lumens, and wall thicknesses. As discussed previously, traditional solid CF require lengthy and costly oxidation processing, and often possess an undesirable skin-core structure as a result of insufficient oxygen diffusion along the characteristic diffusion length to the fiber core. Reducing or eliminating the skin-core structure has been shown to allow for homogeneous stress distribution along the fiber cross

section, leading to improved tensile properties [21, 22]. Additionally, a reduction in precursor fiber diameter (and therefore a reduction in the oxygen characteristic diffusion length during oxidation) has been shown to reduce and even eliminate the skin-core structure [18] and to greatly increase the tensile Young's modulus of the resulting carbon fiber [23]. With this in mind, **it was hypothesized that with reduced wall thickness, one could arrive at an optimally oxidized fiber faster than traditional solid fiber via simultaneous oxidation from the exterior and interior of the filament.** Oxidation from the interior and exterior naturally reduces the oxygen characteristic diffusion length, potentially enabling the avoidance of a skin-core structure. This would allow the resulting HCF to more efficiently utilize the oriented carbon composing the fiber, increasing fiber tensile performance. The development of oxidized HF will be explored in this chapter.

5.2 Experimental

5.2.1 Materials

During HF precursor development, spooled HF precursors were generated and were available for subsequent thermal analysis and study. These are listed in Table 5.1. The spinneret, run number, TechPAN polymer, and coagulation bath composition used during the spinning process are listed, as are the resulting average inner and outer diameters, wall thicknesses, and percent open area for the resulting spooled precursor hollow fibers. The table is divided into HF spun utilizing TP1 and TP2 polymer.

Table 5.1. Spooled hollow fiber precursors available for thermal analysis and study. The spinneret, run number, TechPAN polymer, and coagulation bath composition used during the spinning process are listed, as are the resulting average inner and outer diameters, wall thicknesses, and percent open area for the resulting spooled precursor hollow fibers.

Spinneret	Run	TechPAN Type	Coagulation Bath Composition (wt.% DMSO/water)	Outer Diameter (μm)	Inner Diameter (μm)	Wall Thickness (μm)	Open Area (%)
HF-A	478	TP1	0	158	108	25.0	47
HF-A	489	TP1	0	75	43	16.0	33
HF-A	492	TP1	0	101	63	19.0	39
HF-A	479A	TP1	0	246	150	48.0	37
HF-A	479B	TP1	0	106	66	20.0	39
HF-A	479C	TP1	0	88	56	16.0	40
HF-A	483A	TP1	0	73	43	15.0	35
HF-A	490A	TP1	0	60	36	12.0	36
HF-A	490B	TP1	0	64	40	12.0	39
HF-A	497A	TP1	0	215	153	31.0	51
HF-A	497B	TP1	0	101	61	20.0	36
HF-A	497C	TP1	0	58	33	12.5	32
HF-A	497D	TP1	0	56	32	12.0	33
HF-A	506	TP1	0	46	21	12.5	21
HF-C	516	TP2	0	40	13	13.5	11
HF-A	526A	TP2	0	82	57	12.5	48
HF-A	526B	TP2	0	81	60	10.5	55
HF-A	526C	TP2	0	78	50	14.0	41
HF-A	567B	TP2	0	78	52	13.0	44
HF-A	567C	TP2	0	64	42	11.0	43
HF-A	569A	TP2	0	64	43	10.5	45
HF-A	571A	TP2	10	78	53	12.5	46
HF-A	572	TP2	20	84	53	15.5	40
HF-A	574	TP2	20	77	53	12.0	47
HF-A	575	TP2	30	84	59	12.5	49

5.2.2 Thermal treatment

Hollow PAN fibers were stabilized on a batch scale using a static, constant length method. While static conversion is simplest, it does not produce the highest quality fibers compared to continuous, variable strain stabilization. Specific strain pathways are required in addition to specific temperature/time pathways to achieve the highest possible tensile properties, further complicating the fiber stabilization process. Figure 5.2 presents the time-temperature pathway utilized in this study for batch oxidative stabilization. In Figure 5.2, the fiber was heated in air to 227, 235, 248, and 258 °C with a 20 min isotherm at each temperature, similar to the process described in [8]. Fiber tow was wrapped around the graphite rack and quickly placed into the 227 °C preheated oven (Thermo Scientific Heratherm Advanced Protocol convection oven) and held isothermal for 20 min. The atmosphere was air. The graphite rack was then removed from the oven and the temperature set to 235 °C. The oven was allowed to equilibrate for 5 min before placing the graphite rack back into the oven for another 20 min isotherm. This process was repeated for the 248 and 258 °C isotherms. Occasionally, to examine the effect of higher and lower temperature

isotherms on the HF oxidation, the process was extended to include 20 min. isotherms at 217 and 268 °C. If these extended temperatures are used, this will be noted in the study.

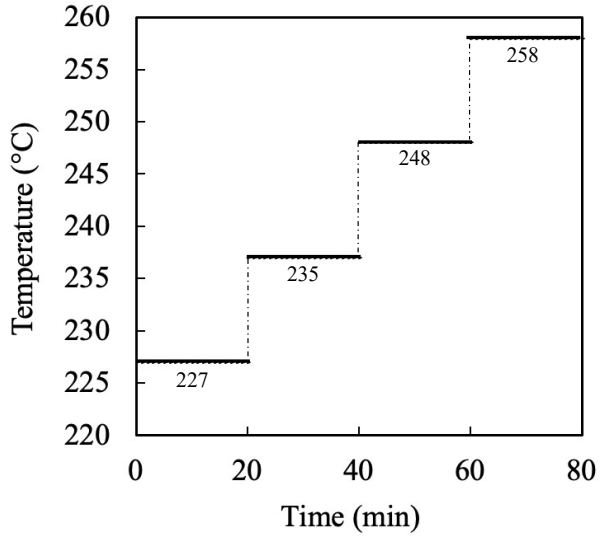

Figure 5.2. Schematic of the oxidation process showing 20 min. isotherms at 227, 235, 248, and 258 °C.

5.2.3 Raman spectroscopy

An oxidized HF sample was prepared and sent to Renishaw for analysis on their InVia Qontor Raman microscope. The precursor HF from run 516 was oxidized according to the stabilization process outlined in Figure 5.2, embedded in epoxy, and polished according to the method in section 3.3. The Raman spectrometer was equipped with an argon ion laser of 457 nm wavelength. The objective lens with magnification of 150x was used and the focused range of the laser beam was 0.2 μm in the x,y directions for collection of the spatial resolution map. The mapping measurement of the spectral window was centered at 1500 cm^{-1} and a laser power of 1% was used.

5.3 Results and discussion

5.3.1 Optical imaging analysis of evolution of skin-core contrast

Batch oxidative stabilization of run 490A precursor HF was completed using the time-temperature pathway shown in Figure 5.2. Figure 5.3 shows various images of the resulting stabilized fibers. In Figure 5.3a, the oxidatively stabilized 490A HF cross section was sectioned using FIB (see section 3.5) and analyzed using EDX mapping for oxygen content (see section 3.6), where oxygen is shown in blue. Higher oxygen levels were observed near the outer and inner surfaces in similar thickness bands. Higher oxygen levels in the outer band (or skin) has been similarly found by other authors for solid fibers [5, 14, 24]. This result suggests that the oxidatively stabilized HF developed a skin-core structure, similar to that seen in commercial fibers, but contained within the wall of the HF.

In this case, oxygen diffusion was observed to occur from both the exterior and interior of the HF, but, similar to traditional fibers, was hindered from reaching the midpoint of the HF wall thickness due to the continual formation of oxidized material near the fiber surface. As noted previously, the oxygen diffusion coefficient through PAN is 300% higher than through an oxidized PAN layer [2]. The average thickness of the 490A precursor HF wall was 12 μm and most precursors for commercial CF which possess a skin-core structure measure 12-14 μm in diameter (see Table 1.2). Therefore, it is not surprising that the oxidatively stabilized HF also showed a skin-core structure, as the characteristic oxygen diffusion distances were similar. This skin-core structure (albeit in the fiber wall) will remain detrimental to the final HCF properties, as it is well known that the structure of CF is inherited from the stabilized fibers [25, 26].

While a skin-core structure persisted for this fiber sample, the EDX data presented here supported the hypothesis that HF could oxidize simultaneously from both the interior and the exterior, at least when short fiber lengths were stabilized in a batch process. And, in this case, the resulting oxidized fiber contained equivalent thickness skin on the exterior and interior. Another interesting observation from the EDX data was the behavior of the skin around the HF macrovoid shown in Figure 5.3a. As discussed previously, HF spun into a 100% water coagulation bath tended to contain macrovoids due to rupture of the

rapidly formed polymer cuticle under pressure of the inward non-solvent diffusion [27]. Here, a macrovoid is present on the interior wall of the HF and the formation of the oxidized fiber skin follows the perimeter of the HF, including around the macrovoid itself. It is hypothesized that the macrovoid communicated to the fiber surface, allowing air (oxygen) to reach the interior of the macrovoid wall and oxidation proceeded. Yu et al. similarly found that skin formation followed the perimeter shape of the fiber (for bean-shaped fiber) [28].

Optical microscopy was investigated as a method for quickly observing and analyzing the skin-core structure of the stabilized HF. Figure 5.3b shows an optical micrograph of the 490A HF which was stabilized similarly to the sample in Figure 5.3a but in a nitrogen atmosphere. Negligible optical contrast through the wall was observed. Recall that in the absence of oxygen, the formation of an infusible polycyclic aromatic structure is not possible [5]. Similar homogeneous solid fiber cross sections have been observed when stabilized in N_2 [5].

Fibers shown in Figure 5.3c, d, and e were stabilized in air using the same process as that of Figure 5.3a. The solid oxidized fibers in Figure 5.3c had a precursor diameter of 12 μm (spun in-house from the same polymer as 490A HF and under similar processing condition, but with a higher solvent concentration coagulation bath, as is typical for producing solid round fibers). These were utilized as a benchmark solid fiber, as their solid fiber diameter was similar to the wall thickness of the 490A HF (12 μm) in Figure 5.3d (and Figure 5.3a). When observing the optical micrographs in Figure 5.3c, d, and e (where Figure 5.3e is a magnified view of Figure 5.3d), a clear skin-core structure was observed, with the skin appearing bright gray and the core a darker gray, as has been found by other researchers utilizing optical microscopy [18, 28]. This darker gray core region is the result of insufficient oxygen diffusion to the core [14, 29]. These results are similar to those found by EDX in Figure 5.3a, consistent with the skin observed in the optical microscopy images containing a higher oxygen content compared to the core. These relatively brighter regions of increased reflectance in the skin have been associated with the formation of the polycyclic aromatic structure via oxidative dehydrogenation and appear brighter under optical microscopy due to their increased reflectance of incident light [7].

When observing Figure 5.3e, the thickness of the interior and exterior skin, as well as the core of the wall, each measured approximately 4 μm, similar to the skin thickness of the solid fibers in Figure 5.3c. It is not surprising that the solid and HF possessed similar skin thicknesses, given that the characteristic oxygen diffusion distances were similar. In fact, several authors have found the thickness of the skin for solid fibers to be limited to 3-5 μm, irrespective of fiber diameter [28, 30]. And, once formed, the thickness of the skin does not change with degree of heat treatment [4]. All of this suggests that the rate at which oxygen atoms react with the fiber is greater than the diffusion rate of oxygen from the surface towards the center of the HF wall (or center of the fiber, in the case of the solid fiber), resulting in a relatively fixed skin-core structure [2, 3, 14]. Sun et al. did find the skin-core to decrease with increasing oxygen content in the atmosphere, with negligible skin-core formation in a 100% oxygen atmosphere. This was attributed to the higher diffusion rate enabled by the higher oxygen content [29]. However, operation of oxidation ovens in a 100% oxygen atmosphere is not practical (or safe), and therefore oxidative stabilization of the HF remains diffusion limited. However, despite being diffusion limited, the results presented here in Figure 5.3 suggest that the formation of the skin-core structure in the HF could be avoided if HF precursor with a wall thickness of $\leq$ 8 μm could be produced.

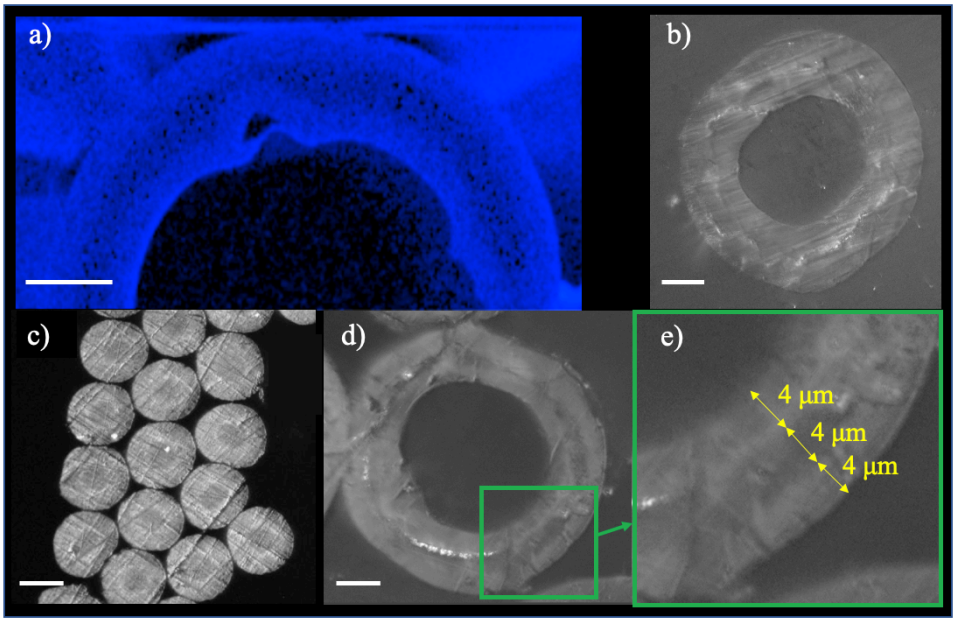

Figure 5.3. EDX and optical microscopy (OM) images of stabilized HF and solid fiber. (a) EDX of oxidized 490A HF for oxygen content (oxygen shown in blue); (b) OM image of nitrogen stabilized 490A HF showing no skin-core structure due to the absence of oxygen during heat treatment; (c) OM images of oxidized solid fiber with diameter similar to the wall thickness of the oxidized 490A HF found in (d). (d) OM image of oxidatively stabilized 490A HF. (e) OM image of oxidized 490A HF wall demonstrating skin-core structure. White scale bars are 10 µm. From the author's original work [31], reprinted with permission.

5.3.2 Spectroscopy

To further probe the differences between the skin and core of the oxidized HF, with a particular focus on understanding the chemical structure differences formed in the HF, several spectroscopic characterization methods were explored.

To complement the EDX data collected, energy-dispersive X-ray spectroscopy (EELS) was envisioned to provide spatial resolution of chemical bonding states. Of particular interest were the C=C C-O, and C=O bonds in the stabilized HF cross section. Upon sectioning via FIB and performing TEM-EELS of multiple stabilized fibers, the results for oxygen content were inconclusive. It is hypothesized that the 200 keV electron beam degraded the stabilized fiber samples, resulting in damage and loss of oxygen.

Another alternative for spatial resolution of chemical bonding was the use of X-ray photoelectron spectroscopy (XPS). It was hoped that the XPS could be used to etch and analyze the HF cross section to provide spatial mapping. However, the etching rate was approximately 0.034 nm/sec, equivalent to requiring 500 min. to etch 1 micron in depth. While it may have been possible to utilize the FIB sectioned fibers for XPS analysis, the XPS spot size was > 30 μm, far too large to spatially resolve bonding differences in the 12 μm wall of the HF. For this type of analysis, a synchrotron XPS system would be required (≤ 200 nm possible resolution), which was not available at the time of this study.

Finally, Raman spectroscopy was explored. A sample was submitted to Renishaw for analysis on their Raman spectroscopy system. The results for oxidized HF from run 516 are shown in Figure 5.4. Although more commonly used for analysis of carbonized materials, the occurrence of cyclization, dehydrogenation, and oxidation during oxidative stabilization result in changes in the hybridization of carbon atoms, making Raman a useful tool for monitoring the evolution of polycyclic aromatic structures in stabilized PAN [32]. In Raman spectroscopy, the G band corresponds to sp^2 hybridized carbons, while the D band corresponds to sp^3 hybridized carbons. For example, single-layered graphene consisting of pure sp^2 hybridized carbon exhibits a strong scattering peak at ~1590 cm^{-1}. When defects are present in the graphene layer, the D peak (indicating sp^3 hybridized carbon atoms) appears at ~1373 cm^{-1} [5]. The ratio of their intensities (I_D/I_G) is often used to quantify the disorder present in the material, with higher I_D/I_G ratios corresponding to higher degrees of disorder and can be used to monitor the evolution of polycyclic aromatic structures in stabilized PAN [5].

In Figure 5.4a, an optical micrograph of the oxidized 516 HF under study shows the bright skins and darker core present in the wall of the HF. The corresponding spatially resolved I_D/I_G ratios from the Raman analysis are shown in Figure 5.4b. The color bar on the right of Figure 5.4b indicates the I_D/I_G ratio and its corresponding color, with red indicating the highest I_D/I_G ratio and dark blue indicating the lowest I_D/I_G ratio. As shown in the spatial image, there is a clear difference between the structural disorder in the skin and core of the oxidized HF, which overlay nicely with the skin-core observed under optical microscopy (Figure 5.4a) and are similar to the results found using EDX (Figure

5.3). The skin region is shown by the Raman method to contain lower levels of disorder compared to the core. This is in agreement with the chemical structures presented in Figure 1.8, where the skin is shown to possess more sp^2 hybridized carbon compared to the core, and with the findings of other authors [5, 33].

Another interesting observation regarding Figure 5.4a and b is the disappearance of the outer skin at the fusion point of the fibers. This resulted in the cores merging. Meanwhile, the inner skin is unaffected. This is consistent with oxygen diffusion from the air clearly causing skin development. Interestingly, there appears to be little gradient between skin and core, which is consistent with the oxidized skin functioning as a barrier to oxygen permeation. In all, Figure 5.4b seems to confirm the role of oxygen in the formation of polycyclic aromatic structures in the structure.

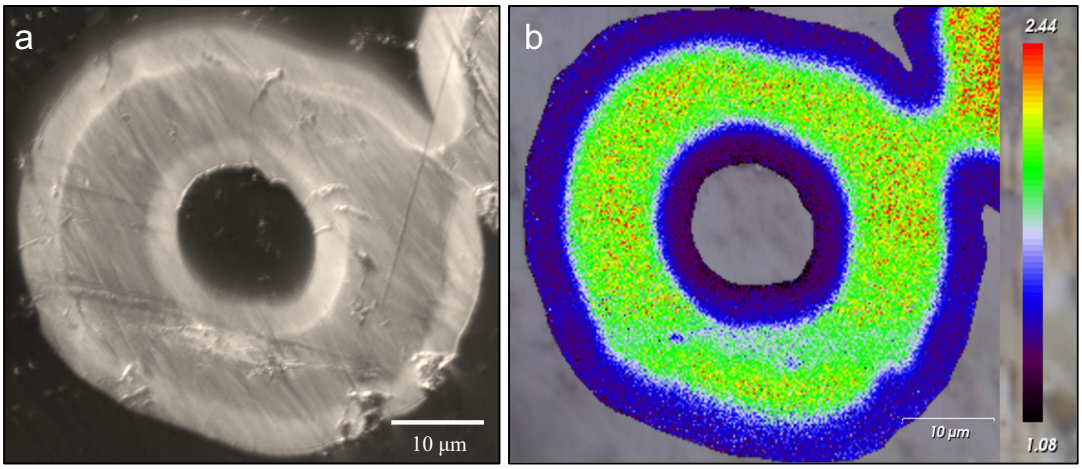

Figure 5.4. Raman spectroscopy analysis of run 516 oxidized HF. (a) Optical micrograph of oxidized HF showing bright skin and darker core region within the HF wall. (b) Spatial resolution of I_D/I_G ratio.

Figure 5.5 displays the intensity of the D and G peaks for both the skin and core. Both the D and G peaks present higher intensity in the skin, with the core showing a very small D peak and negligible G peak. The lower signal intensity presented by the core relative to the skin could be explained by the core being lower density due to less crosslinking [34] and/or a lower degree of dehydrogenation [35]. The stronger signal generated by skin has been attributed to the formation of polycyclic aromatic structures [5]. Overall, the spatially resolved Raman spectral analysis supports the previously

presented data, in that the skin and core of the oxidized HF are chemically and structurally different. These differences are the result of the diffusion limited oxidation process, where oxygen is largely responsible for the formation of conjugated and aromatic structures in the skin [36-40] which possess higher degrees of order and density. The results support the use of optical microscopy as a simple and efficient method for distinguishing differences between the skin and core in the oxidized HF.

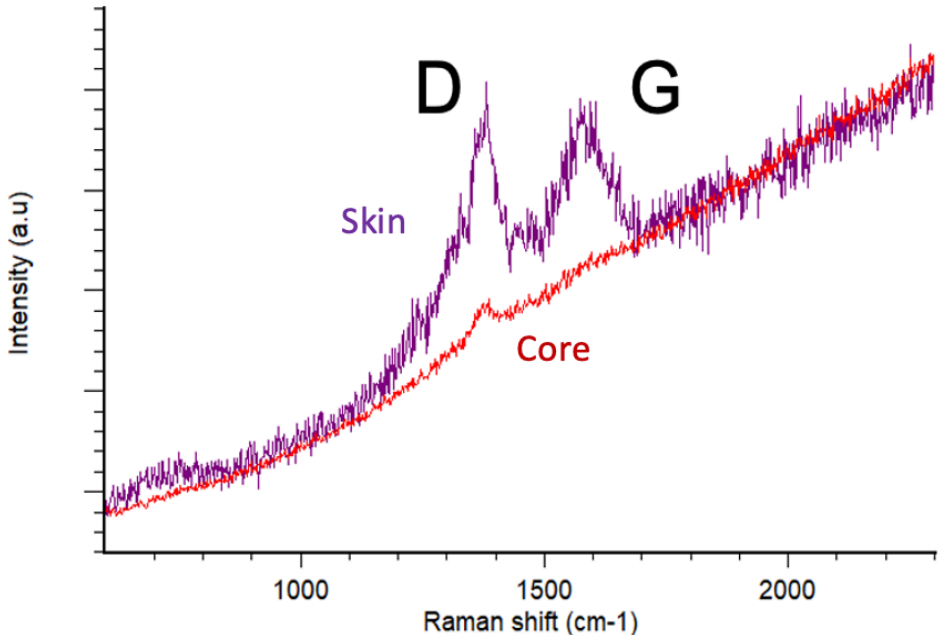

Figure 5.5. Raman peak intensities for D and G for both skin and core of the oxidized HF from run 516.

5.3.3 Percent open area and internal oxidation

It is clear from the previously presented data that oxidized HF presents a similar skin-core structure to traditional solid fibers (albeit in the fiber wall) when HF precursor wall thicknesses are > 8 µm, as is the case for all HF produced under this study. While the scope of this study was limited in its ability to further reduce the HF wall thickness, it was possible to produce HF with varying percent open area, primarily through variation in draw ratio, where percent open area is defined as in Eqn. 5.1,

$$\left(\frac{\mathrm{ID}}{\mathrm{OD}}\right)^2 \times 100 = \%\mathrm{OA} \qquad \text{Eqn. 5.1}$$

where ID is the inner diameter of the fiber, OD is the outer diameter, and %OA is the percent open area. Whereas the exterior of the HF has access to a, generally speaking, unlimited amount of oxygen (air) from the atmosphere, the closed nature of the HF means that the interior may see limited oxygen availability proportional to the air contained within the volume (or area) of the lumen. However, there was also the potential that air could be drawn into the HF lumen during the stabilization process, thereby providing a rather "continuous" oxygen supply. There were doubts as to whether this was possible, particularly for long lengths of continuous fiber (≥ 1 m), as the oxidized fiber lengths studied thus far were much shorter.

To understand the impact of percent open area on the internal oxidation, as well as to determine the ability of HF to draw air into the lumen, an experiment was designed utilizing two identical sets of HF with varying percent open area. HF tows from runs 516, 506, 497C, 490B, and 526A with 11, 20, 33, 39, and 44% open area, respectively, were selected and fed through a Heratherm oven via ports machined into the sides of the oven, as shown in Figure 5.6. Fiber tows were 1 m in length with 0.4 m of length located in the hot zone. One set of fibers had their ends embedded and cured in epoxy in order to "close" the HF ends to the atmosphere. The duplicate set had their ends left open to the atmosphere. Both sets were oxidized simultaneously in an air atmosphere under the oxidation conditions outlined in Figure 5.2a, up to a 250 °C final oxidation temperature. Fiber tow samples were collected at the end of each isotherm.

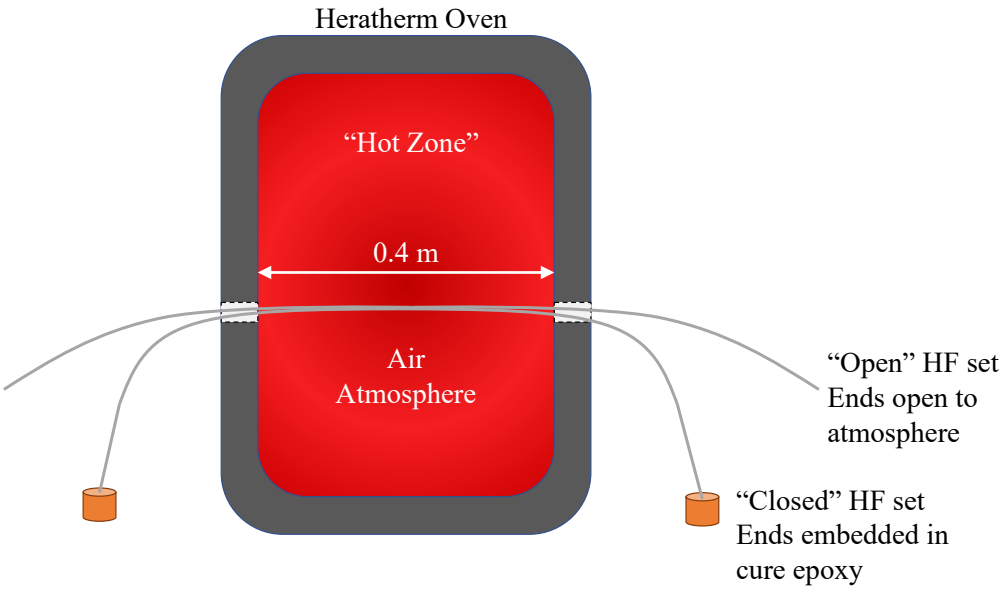

Figure 5.6. Experimental setup for evaluating the impact of HF percent open area and the impact of open versus closed HF ends on internal and external HF oxidation.

Following sample collection, specimens were collected from the middle of the fiber length (i.e. the center of the oxidation furnace). Following embedding in epoxy and polishing as in section 3.3, Adobe Photoshop was used to perform measurements, as shown in Figure 5.7. In Figure 5.7a, the as-captured optical micrograph for run 526A oxidized HF (44% OA) is shown. The corresponding image in Figure 5.7b shows the four measurements taken in Adobe Photoshop. Measurements were taken to calculate the thickness, perimeter, and area of the inner and outer skins of the hollow fibers, as well as the core, shown in red, green, blue, and yellow. Similarly, Figure 5.7c shows run 516 oxidized HF (11% OA) and its corresponding measurements in Figure 5.7d.

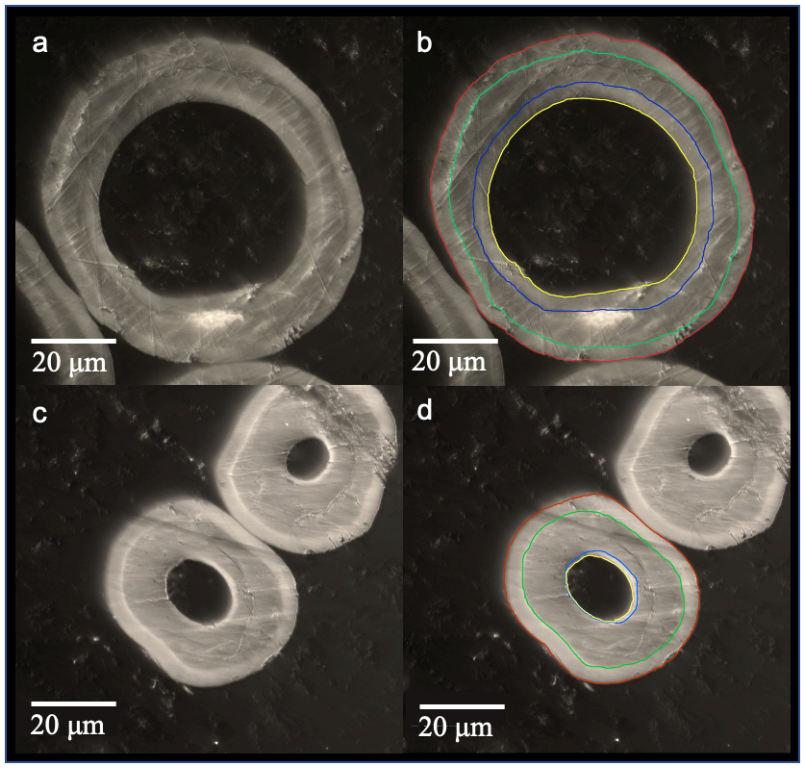

Figure 5.7. Optical micrographs of oxidized HF indicating measurements made. (a) Optical micrograph of run 526A oxidized HF (44% OA) and (b) the red, green, blue, and yellow lines indicating example measurements taken on the fiber. Similarly, (c) is an optical micrograph of run 516 oxidized HF (11% OA), also with (d) red, green, blue, and yellow lines indicating examples of measurements taken on the fiber.

In Figure 5.8, the ratio of interior skin thickness to half of the wall thickness ($x/(0.5t)$) is plotted versus percent open area for the HF sets with open and closed (embedded in epoxy) ends. If the oxygen available within the fiber lumen was sufficient to completely oxidize the interior skin of the lumen to the midpoint of the fiber wall, $x/(0.5t)$ would be equal to 1.

The results in Figure 5.8 indicated that the interior skin thickness increased as percent open area increased. In addition, no difference was observed between data points gathered from HF oxidized with open versus closed ends. This suggests that air is not drawn into the HF lumen during the oxidation process, and rather that the formation of the interior skin thickness is limited by the volume of air contained within the lumen at the start. Less

percent open area for a given HF will result in an oxidized HF with a thinner interior skin, which is observed in Figure 5.7c and d.

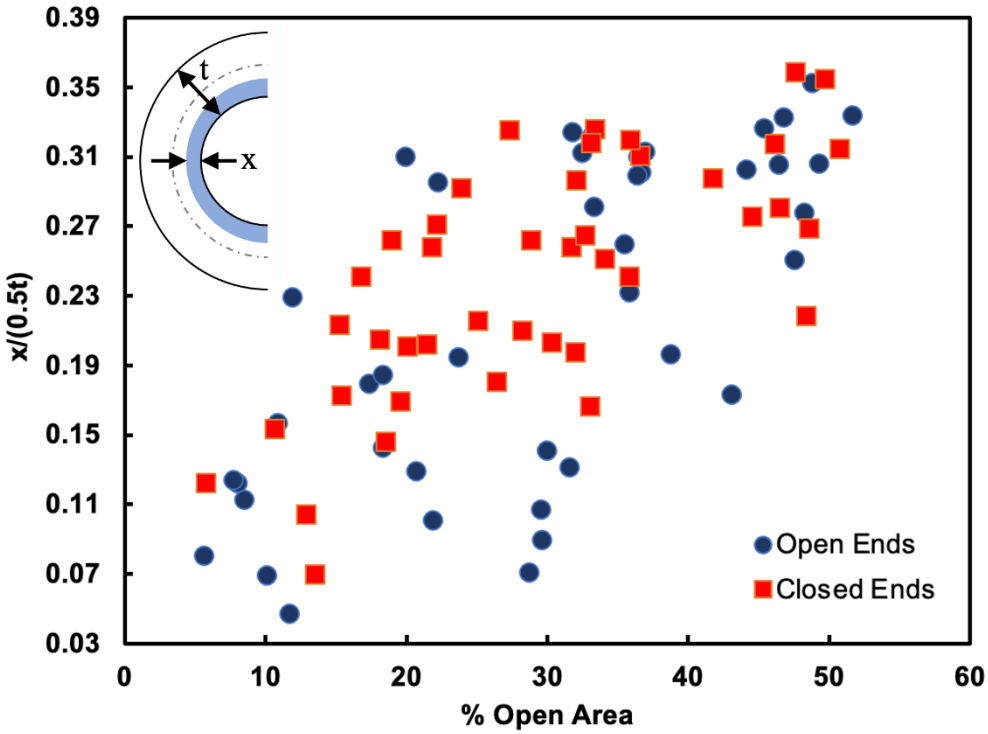

Figure 5.8. The ratio of inner skin thickness (x) to the midpoint of the oxidized HF wall thickness as a function of percent open area for two sets of HF, one with ends open to the atmosphere and one with ends closed (embedded in epoxy).

Data from Figure 5.8 was plotted again, but with inner and outer diameter skin thickness as a function of percent open area. The results are shown in Figure 5.9. A linear fit (shown by the dashed lines) was applied to both inner and outer diameter skin thickness data sets. Observation of the outer diameter skin thickness showed the skin thickness to be quite constant, and independent of the percent open area of the lumen. The outer layer thickness averaged 4.18 ± 0.35 µm (N = 89). This layer thickness is consistent with that seen in the literature for solid fibers, independent of fiber diameter [28, 30]. The inner layer thickness, on the contrary, increased with increasing percent open area. While there is scatter in the data, the linear fit suggested that in order to achieve the average layer thickness of the outer layer (~4 µm), the HF should approach 50% open area. Based on this data, as well as observations made from the optical microscopy analysis, it can be

hypothesized that the HF wall thickness should be ≤ 8 µm with ≥ 50% open area in order to produce an oxidized HF with homogeneous cross section (non-skin core).

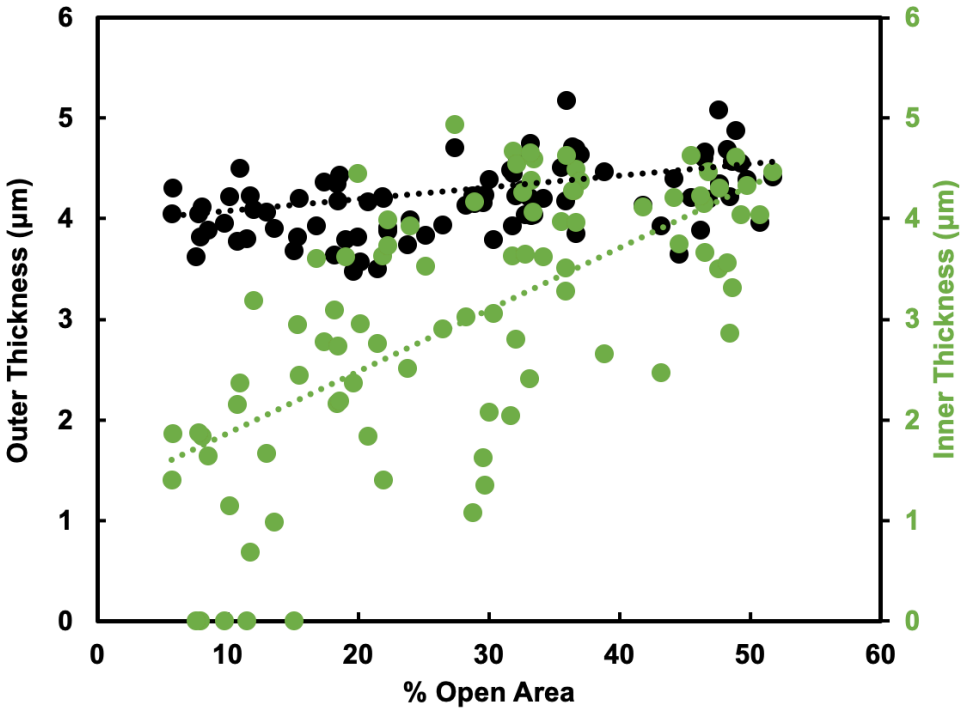

Figure 5.9. The outer and inner layer thicknesses for oxidized HF as a function of percent open area.

5.3.4 Oxidized HF density

The data presented earlier in this chapter support the hypothesis that hollow fiber is able to oxidize not only from the exterior but from the interior as well. Given this enhanced oxidation capability, it was further hypothesized that the hollow fiber would oxidize at an increased rate compared to a solid fiber of similar outer diameter. Oxidized fiber density has been used extensively to quantify the extent of oxidation [19, 20]. In fact, a linear correlation has been found between fiber density and the IR absorbance ratio between the pendant nitrile, $\nu_{C=N} \approx 2195$ cm^{-1}, and the cyclic nitrile, $\nu_{C=N} \approx 2240$ cm^{-1}, for oxidized fibers where pendant nitrile groups are converted into a cyclic structural arrangement [41]. Further, several authors have indicated that the ideal oxidized fiber density for the production of high tensile strength CF is 1.34 to 1.39 g/cc [15].

Ideally, to test this hypothesis, precursor fibers would be spun under the same conditions with the same outer diameter and varying percent open area (for example, 0 (solid), 10, 20, 30, 40, and 50% open area). It is hypothesized that when holding outer diameter constant and varying percent open area during oxidation, the HF with 50% open area would oxidize much faster than the solid, for example, due to the reduced characteristic oxygen diffusion length as well as the increased volume of air available in the lumen compared to HF with smaller percent open areas (10%, for example), resulting in a thicker inner skin and reduced skin-core structure, as was seen in Figure 5.8 and Figure 5.9.

Evaluating the precursor fibers available in this study (Table 5.1), several HF were chosen with outer diameter ~ 80 μm (shown in Table 5.2). Run 567B, 571A, and 526B had 44, 46, and 55% open area. These were the best precursors available at the time to test the hypothesis. For comparison, a 78 μm diameter solid fiber was spun from TP2 using a 78 wt.% DMSO/water bath (run 549A), as is common for the production of round solid precursor filaments (also listed in Table 5.2). Fibers were oxidatively stabilized according to Figure 5.2, with an added 20 min. isotherm at 217 °C. They were sampled after each oxidation stage for density analysis according to section 3.7. Density results are shown in Figure 5.10.

Table 5.2. Precursor hollow fibers selected for oxidation study versus a similar outer diameter solid fiber.

Run	TechPAN Type	Coagulation Bath Composition (wt.% DMSO/water)	Outer Diameter (μm)	Inner Diameter (μm)	Wall Thickness (μm)	Open Area (%)
567B	TP2	0	78	52	13.0	44
571A	TP2	10	78	53	12.5	46
526B	TP2	0	81	60	10.5	55
549A	TP2	78	78	N/A	N/A	N/A

Figure 5.10 shows the density values from precursor through the 258 °C oxidation temperature. It is clear that the solid precursor fiber (549A) had a much lower precursor density of 1.1299 ± 0.0025 g/cc compared to the three HF under study (567B, 571A, and 526B), whose precursor densities averaged 1.1781 g/cc, which is much closer to the known density of PAN polymer (1.18 g/cc) [9, 42, 43]. This low starting density likely stemmed from internal voids and persisted through the oxidation process, with the final oxidized

fiber, following 258 °C heat treatment, attaining an oxidized density of 1.2534 ± 0.0013 g/cc. On the contrary, the HF under study reached an average oxidized density of 1.3224 g/cc.

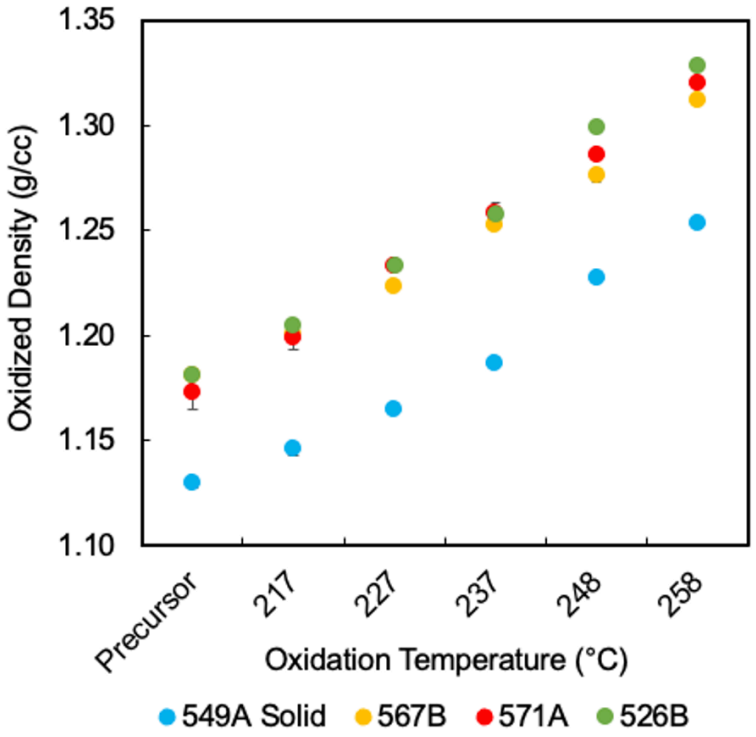

Figure 5.10. Oxidized fiber densities as a function of heat treatment temperature.

To determine the rate of oxidation, the percent increase in density from the precursor was calculated according to Eqn. 5.2, where ρ_0 is the precursor density and ρ_i is the oxidized fiber density following heat treatment at temperature i ($i =$ 217, 227, 237, 248, 258 °C). Results are plotted in Figure 5.11 as a function of temperature. A linear fit was applied to each data set and the slope of the fit used to determine the rate of densification, with results shown in Table 5.3.

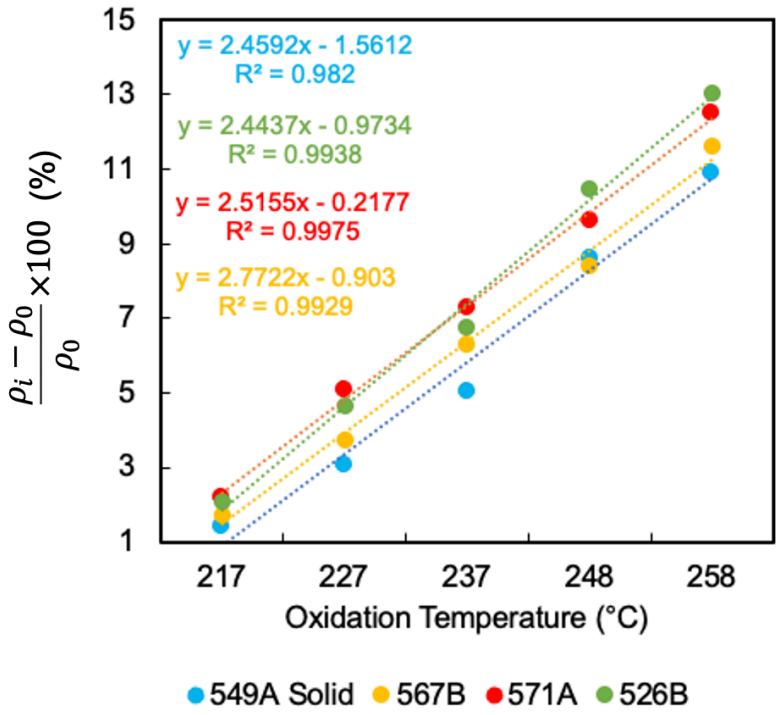

Figure 5.11. Percent increase in density from the precursor for solid and hollow fiber plotted as a function of heat treatment temperature.

$$\frac{(\rho_i - \rho_0)}{\rho_0} \times 100 \qquad \text{Eqn. 5.2}$$

Table 5.3. Comparison of densification rate for oxidized HF compared to oxidized solid fibers with similar outer diameter.

Fiber	Open Area (%)	Linear Fit Slope	Increase in densification rate (%)
549A solid	---	2.4592	---
567B	45	2.4437	-0.6
571A	47	2.5155	2.3
526B	55	2.7722	12.7

In Table 5.3, the increase in densification rate for several oxidized HF are shown, compared to a solid fiber of similar outer diameter. The results show what can be interpreted as no change in densification rate for the 567B HF, which had 45% open area. A slight increase of 2.3% in rate was observed for the 571A HF, with a 47% open area.

The largest increase in densification rate was 12.7% which was achieved by 526B HF with a 55% open area.

It is interesting that 567B HF with 45% open area and the ability to oxidize from the interior and exterior showed no advantage in increasing densification rate over the oxidized solid fiber derived from run 549A. The skin of oxidized PAN fiber is higher density than the core [17, 18], but the magnitude of difference between skin and core material skeletal density has not been directly measured. One potential method to determine the density of the skin and core material is to evaluate fiber densities resulting from both oxidatively stabilized fibers and fibers heated treated in N_2. In the absence of oxygen (under an N_2 atmosphere), the skin-core structure does not form, as shown previously in Figure 5.3b. During oxidative stabilization, the skin-core forms with the core resulting from oxygen starvation, as discussed at length previously. Therefore, it may be assumed that the density of material resulting from N_2 heat treatment represents the density of the core material of the oxidized fiber. Given that the overall oxidized fiber density contains the density of the skin and core, then using the rule of mixtures, it may be possible to calculate the density of the skin of the oxidized fiber.

Calculation of the oxidized fiber skin density was attempted utilizing the 549A solid fiber, whose densities were determined after N_2 heat treatment and after oxidative stabilization. The density results are shown in Table 5.4, along with the skin and core area fractions of the oxidized fiber, as measured using Adobe Photoshop, and the resulting calculated skin density using the rule of mixtures according to Eqn. 5.3. In Eqn. 5.3, x and y represent the core and skin area fractions, respectively, and ρ_{N_2}, ρ_{skin}, and ρ_{ox} represent the N_2 heat treated (assumed to represent the core density in the oxidized fiber), skin, and overall oxidized fiber densities, respectively. Solving for the skin density yielded an average skin density of 1.2953 g/cc. The maximum density of the core (N_2 heat treated fiber density) was 1.2494 g/cc. Therefore, while the skin was denser than the core, it was only 3.5% denser than the core.

Table 5.4. Comparison of measured densities for 549A solid fiber heat treated in N_2 and oxidatively stabilized, where skin and core area fractions were measured and oxidized fiber skin density was calculated by rule of mixtures assuming the N_2 treated fiber densities represent the densities of the core material.

549A Solid Fiber Sampling Point	N_2 Treated Fiber Density (g/cc)	Oxidized Fiber Density (g/cc)	Oxidized Fiber Skin Area Fraction	Oxidized Fiber Core Area Fraction	Calculated Skin Density (g/cc)
Post 227 °C Isotherm	1.1303	1.1824	0.26	0.74	1.3270
Post 235 °C Isotherm	1.1729	1.2115	0.32	0.68	1.2936
Post 248 °C Isotherm	1.1954	1.2410	0.47	0.53	1.2931
Post 258 °C Isotherm	1.2494	1.2583	0.49	0.51	1.2674

$$x\rho_{N_2} + y\rho_{skin} = \rho_{ox} \qquad \text{Eqn. 5.3}$$

In addition to the experimental results provided above, interpretation of results presented in the literature may provide added insight. For example, further analysis of the results presented by Kong et al. [18], including the use of Adobe Photoshop to determine the area fractions of the skin and core of their stabilized fibers (shown in Figure 5.12), were correlated to their measured stabilized fiber densities and the results shown in Table 5.5. An oxidatively stabilized fiber with 17% core area (A1) had a measured density of 1.3591 g/cc. In comparison, the A3 oxidized fiber contained no skin-core structure and the density was increased to 1.3614 g/cc. Interpretation of these results indicated that the core was of lower density than the skin. However, a reduction in the skin-core structure by 17% (the core area of A1) resulted in a corresponding density increase of only 0.2%.

Table 5.5. Analysis of the results presented by Kong et al. for their stabilized PAN fibers with differing skin and core area fractions, compared to their resulting measured densities. Adapted from [18].

Oxidized Fiber from Kong et al.	Skin Area Fraction	Core Area Fraction	Density (g/cc)
A1	0.83	0.17	1.3591
A2	0.88	0.12	1.3596
A3	1	0	1.3614

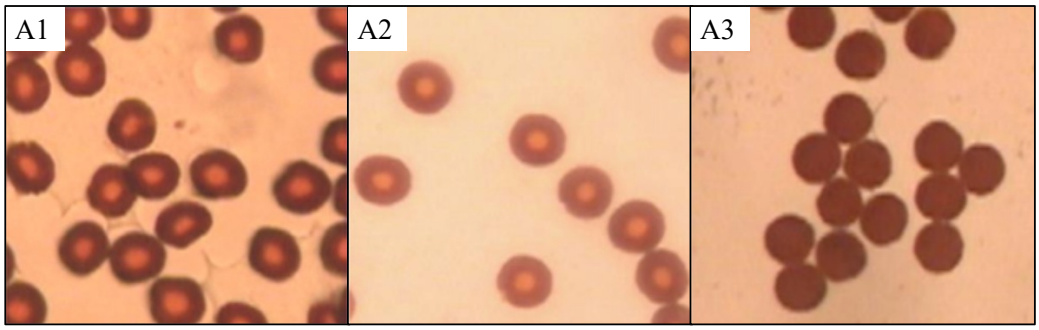

Figure 5.12. Optical microscopy images of oxidized PAN fibers with different diameters after stabilization. Adapted by permission from [18], © 2015.

The experimental and literature results presented above support the findings of other authors that the density of the skin is higher than the core in an oxidized PAN fiber [17, 18], but further show that the magnitude in difference is quite small, and therefore reductions in the skin-core structure elicit only minute changes in the resulting oxidized fiber densities.

Another potential caveat to the data presented here regards the solid fiber used for comparison and calculation. As the HF precursors produced in this study were larger in diameter than traditional precursors, relatively large diameter solid fiber had to be spun in order to compare hollow and solid with similar outer diameter. In the process of spinning large diameter solid fiber, minimal draw was applied to the fiber in order to keep the diameter large. Under these conditions, molecular alignment is limited and pore collapse less likely to occur. The resulting large diameter solid fiber contains macrovoids as a result. The presence of significant void structure is supported by the lower density of the precursor fibers, at 1.1299 g/cc, as well as the optical micrographs presented in Figure 5.13. Figure 5.13 contains a selection of optical micrographs of 549A solid fiber following oxidation at 227 and 258 °C. When oxidized at 227 °C (Figure 5.13a), the resulting fibers consisted of a ~ 4 μm thick skin (blue in color) and an orange tinted core. Observation of the core revealed the presence of voids, which are shown as bright yellow shapes situated about the perimeter of the fibers. As oxidation proceeded and reached 258 °C (Figure 5.13b), the fibers show significant skin thickening, particularly where voids are present about the perimeter. It is hypothesized that these voids contain air or communicate with the outer diameter which contribute oxygen to the oxidation process which would otherwise not exist

in a dense fiber. The skin of the fiber can be seen to thicken in areas about the fiber circumference where voids are prevalent. It is hypothesized that, were it possible to spin large diameter precursors with appropriate density (~1.18 g/cc) and negligible macrovoid structure, the rate of densification of the solid fiber would be much lower than that presented in Figure 5.10. As a result, the increase in densification for the HF compared to the solid fiber would be higher than that presented in Table 5.3.

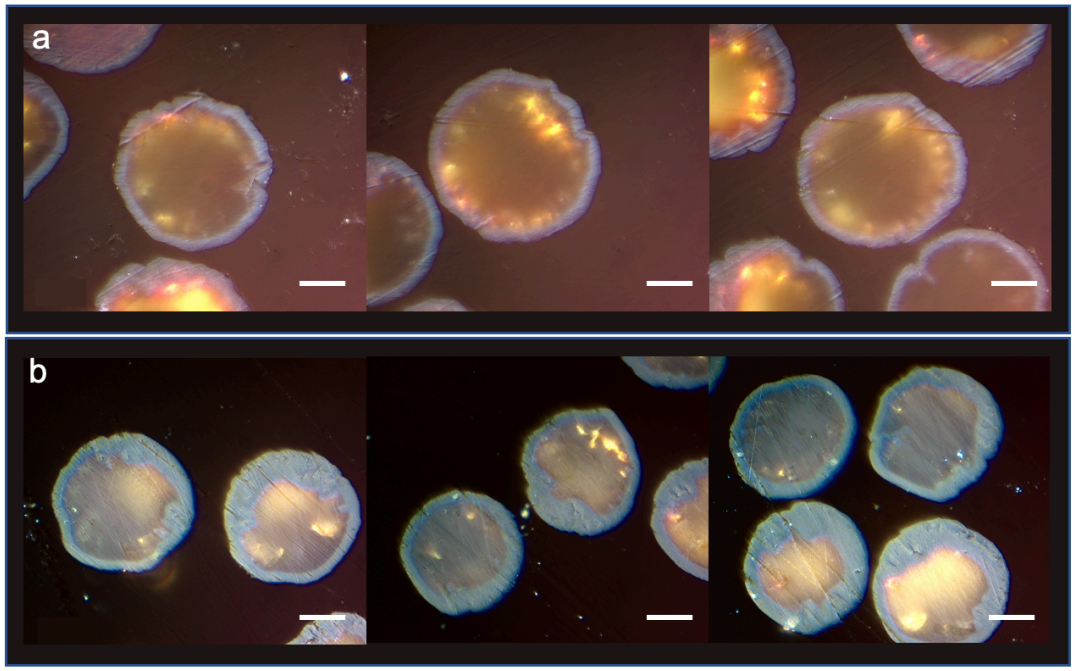

Figure 5.13. Optical micrographs of 549A solid fiber (78 µm diameter) sampled after oxidative stabilization at (a) 227 and (b) 258 °C. White calibration bars are 20 µm.

5.4 Conclusions

Utilizing the HF precursors discussed in Chapter 4, oxidation studies were completed. **It was hypothesized that with reduced wall thickness, one could arrive at an optimally oxidized fiber much faster than traditional solid fiber via simultaneous oxidation from the exterior and interior of the filament.** In the process of investigating this hypothesis, it was discovered that oxidation of the HF precursors produced in this study led to the development of a skin-core structure within the wall of the resulting HF due to the large dimensions of the HF. For a wall thickness of 12 µm, an interior and exterior skin of 4 µm was observed. The skin was found to contain higher levels of oxygen via EDX.

Optical microscopy and spatially resolved Raman spectroscopy overlaid well, indicating that the skin of the oxidized HF contains oxygen and sp^2 hybridized carbons and can be easily observed using optical microscopy. The EDX, optical microscopy, and Raman results support the hypothesis that a homogeneous cross section could be produced if the HF wall thickness were ≤ 8 μm.

Further, a study evaluating the effect of percent open area of the HF on skin-core development was completed. It was found that air was not pulled into the fibers through the lumen during oxidation, but rather that the oxygen available to the HF lumen was determined by the initial volume of air contained within the lumen. As a result, the thickness of the interior skin was dependent on the percent open area of the HF. Further, the outer skin thickness averaged 4.18 μm, independent of fiber dimension. Based on the data, it was determined that in order to obtain a similar thickness interior skin layer, the HF should possess ≥ 50 % open area. This data sharpened the hypothesis that, if a ≥ 50 % open area HF could be produced, a ≤ 8 μm wall thickness would lead to an oxidized HF with a homogeneous (non-skin-core) morphology.

Finally, the core hypothesis was examined, to determine if **with reduced wall thickness, one could arrive at an optimally oxidized fiber much faster than traditional solid fiber via simultaneous oxidation from the exterior and interior of the filament.** HF with varying percent open area and similar outer diameters were oxidized alongside an in-house spun solid fiber with similar diameter. When compared to the solid fiber, the HF with 45% open area (567B) demonstrated a negligible difference in rate of densification, while HF with 55% open area (526B) demonstrated a 12.7% increase in rate of densification over the solid fiber. It was interesting to find no difference in rate of densification for the HF with 45% open area compared to a solid fiber, but this was attributed to difficulty performing a direct comparison between the HF and solid due to differences in their precursor morphology. The solid precursor used in the study contained a large portion of macrovoids, which reduced the solid precursor density to 1.1299 g/cc, much lower than the HF precursors of ~1.18 g/cc. In addition, these macrovoids contained air, which likely enhanced the oxidation of the solid precursor fiber. As a result, it is hypothesized that the solid fiber with macrovoids oxidized at a faster rate compared to a

solid precursor fiber of that diameter with an appropriate density (~1.18 g/cc). Therefore, when comparing the HF and solid fiber under study, the rate of densification of the HF over solid was only 12.7% higher. Nonetheless the HF did densify faster than the solid, baseline fiber.

5.5 Future work

Future oxidation studies should be prefaced by the development of HF precursors with targeted dimensions. Of particular interest would be HF with ≤ 8 μm wall thickness and ≥ 50 % open area. Here it was hypothesized that such filaments could be oxidized and a skin-core structure avoided. The production of precursor filaments with these dimensions would allow direct testing of that hypothesis. Spinning such fibers remains difficult, but not impossible.

Finally, if precursor HF could be produced with reduced outer diameter approaching the 10-14 μm diameter seen in traditional solid PAN precursors, the HF and a solid fiber of comparable precursor density could be oxidized and compared more accurately for evaluation of rate of oxidation. Taken further, the use of multiple spinnerets of varying dimensions could allow for the production of HF with more ideal varying percent open area (for example, 10%, 20%, 30%, etc.) with the same outer diameter under the same draw conditions. Again, this would allow more direct comparison of oxidation rate without the current confounding variables of draw, etc. but would require immense process control.

5.6 References

1. Rahaman, M.S.A., A.F. Ismail, and A. Mustafa, *A review of heat treatment on polyacrylonitrile fiber.* Polymer Degradation and Stability, 2007. **92**(8): p. 1421-1432.
2. Warner, S.B., L.H. Peebles, and D.R. Uhlmann, *Oxidative stabilization of acrylic fibres.* Journal of Materials Science, 1979. **14**(3): p. 556-564.
3. Blanco, C., S. Lu, S. Appleyard, and B. Rand, *The stabilisation of carbon fibres studied by micro-thermal analysis.* Carbon, 2003. **41**(1): p. 165-171.
4. Kikuma, J., T. Warwick, H.-J. Shin, J. Zhang, and B.P. Tonner, *Chemical state analysis of heat-treated polyacrylonitrile fiber using soft X-ray spectromicroscopy.* Journal of electron spectroscopy and related phenomena, 1998. **94**(3): p. 271-278.
5. Choi, J., S.-S. Kim, Y.-S. Chung, and S. Lee, *Evolution of structural inhomogeneity in polyacrylonitrile fibers by oxidative stabilization.* Carbon, 2020.

6. Karacan, I. and G. Erdoğan, *A study on structural characterization of thermal stabilization stage of polyacrylonitrile fibers prior to carbonization.* Fibers and Polymers, 2012. **13**(3): p. 329-338.
7. Jagtoyen, M., F. Derbyshire, S. Rimmer, and R. Rathbone, *Relationship between reflectance and structure of high surface area carbons.* Fuel, 1995. **74**(4): p. 610-614.
8. Nunna, S., M. Setty, and M. Naebe, *Formation of skin-core in carbon fibre processing: A defect or an effect?* Express Polymer Letters, 2019. **13**(2): p. 146-158.
9. Morgan, P., *Carbon fibers and their composites*. 2005, Boca Raton, LA: Taylor & Francis Group.
10. Ogawa, H. and K. Saito, *Oxidation behavior of polyacrylonitrile fibers evaluated by new stabilization index.* Carbon, 1995. **33**(6): p. 783-788.
11. Jain, M.K. and A.S. Abhiraman, *Conversion of acrylonitrile-based precursor fibres to carbon fibres.* Journal of Materials Science, 1987. **22**(1): p. 278-300.
12. Gupta, A.K., D.K. Paliwal, and P. Bajaj, *Acrylic Precursors for Carbon Fibers.* Polymer Reviews, 1991. **31**(1): p. 1-89.
13. Damodaran, S., P. Desai, and A.S. Abhiraman, *Chemical and physical aspects of the formation of carbon fibres from PAN-based precursors.* The Journal of The Textile Institute, 2008. **81**(4): p. 384-420.
14. Lv, M.-Y., H.-Y. Ge, and J. Chen, *Study on the chemical structure and skin-core structure of polyacrylonitrile-based fibers during stabilization.* Journal of Polymer Research, 2008. **16**(5): p. 513-517.
15. Takaku, A., T. Hashimoto, and T. Miyoshi, *Tensile properties of carbon fibers from acrylic fibers stabilized under isothermal conditions.* Journal of Applied Polymer Science, 1985. **30**(4): p. 1565-1571.
16. Sun, T., Y. Hou, and H. Wang, *Mass DSC/TG and IR ascertained structure and color change of polyacrylonitrile fibers in air/nitrogen during thermal stabilization.* Journal of Applied Polymer Science, 2010. **118**(1): p. 462-468.
17. Ge, Y., Z. Fu, Y. Deng, M. Zhang, and H. Zhang, *The effects of chemical reaction on the microstructure and mechanical properties of polyacrylonitrile (PAN) precursor fibers.* Journal of Materials Science, 2019. **54**(19): p. 12592-12604.
18. Kong, L., H. Liu, W. Cao, and L. Xu, *PAN fiber diameter effect on the structure of PAN-based carbon fibers.* Fibers and Polymers, 2015. **15**(12): p. 2480-2488.
19. Turner, W. and F. Johnson, *The pyrolysis of acrylic fiber in inert atmosphere. I. Reactions up to 400° C.* Journal of Applied Polymer Science, 1969. **13**(10): p. 2073-2084.
20. Thorne, D. and J. Marjoram, *Optical properties and orientation of thermally treated acrylic fibers.* Journal of Applied Polymer Science, 1972. **16**(6): p. 1357-1366.
21. Liu, J., Z. Yue, and H. Fong, *Continuous nanoscale carbon fibers with superior mechanical strength.* Small, 2009. **5**(5): p. 536-42.
22. Liu, F., H. Wang, L. Xue, L. Fan, and Z. Zhu, *Effect of microstructure on the mechanical properties of PAN-based carbon fibers during high-temperature graphitization.* Journal of Materials Science, 2008. **43**(12): p. 4316-4322.

23. Morris, E.A., M.C. Weisenberger, M.G. Abdallah, F. Vautard, H. Grappe, S. Ozcan, F.L. Paulauskas, C. Eberle, D. Jackson, S.J. Mecham, and A.K. Naskar, *High performance carbon fibers from very high molecular weight polyacrylonitrile precursors.* Carbon, 2016. **101**: p. 245-252.
24. Watt, W. and W. Johnson, *Mechanism of oxidisation of polyacrylonitrile fibres.* Nature, 1975. **257**(5523): p. 210-212.
25. Liu, X., C. Zhu, J. Guo, Q. Liu, H. Dong, Y. Gu, R. Liu, N. Zhao, Z. Zhang, and J. Xu, *Nanoscale dynamic mechanical imaging of the skin–core difference: From PAN precursors to carbon fibers.* Materials Letters, 2014. **128**: p. 417-420.
26. Sui, X., Z. Xu, C. Hu, L. Chen, L. Liu, L. Kuang, M. Ma, L. Zhao, J. Li, and H. Deng, *Microstructure evolution in γ-irradiated carbon fibers revealed by a hierarchical model and Raman spectra from fiber section.* Composites Science and Technology, 2016. **130**: p. 46-52.
27. Grobe, V. and K. Meyer, Faserforschung und Textiltechnik, 1959. **10**: p. 214-224.
28. Yu, M.-J., C.-G. Wang, Y.-J. Bai, M.-X. Ji, and Y. Xu, *SEM and OM study on the microstructure of oxidative stabilized polyacrylonitrile fibers.* Polymer Bulletin, 2007. **58**(5-6): p. 933-940.
29. Sun, T., Y. Hou, and H. Wang, *Effect of atmospheres on stabilization of polyacrylonitrile fibers.* Journal of Macromolecular Science, Part A, 2009. **46**(8): p. 807-815.
30. Layden, G., *Retrograde core formation during oxidation of polyacrylonitrile filaments.* Carbon, 1972. **10**(1): p. 59-63.
31. Morris, E.A., R. Sarabia-Riquelme, N. Hochstrasser, J. Burgess, A.E. Oberlink, D.L. Eaton, and M.C. Weisenberger, *Early development of multifilament polyacrylonitrile-derived structural hollow carbon fibers from a segmented arc spinneret.* Carbon, 2021. **178**: p. 223-232.
32. Nunna, S., C. Creighton, N. Hameed, M. Naebe, L.C. Henderson, M. Setty, and B.L. Fox, *Radial structure and property relationship in the thermal stabilization of PAN precursor fibres.* Polymer Testing, 2017. **59**: p. 203-211.
33. Gulgunje, P.V., B.A. Newcomb, K. Gupta, H.G. Chae, T.K. Tsotsis, and S. Kumar, *Low-density and high-modulus carbon fibers from polyacrylonitrile with honeycomb structure.* Carbon, 2015. **95**: p. 710-714.
34. Nunna, S., C. Creighton, B.L. Fox, M. Naebe, M. Maghe, M.J. Tobin, K. Bambery, J. Vongsvivut, and N. Hameed, *The effect of thermally induced chemical transformations on the structure and properties of carbon fibre precursors.* Journal of materials chemistry A, 2017. **5**(16): p. 7372-7382.
35. Sha, Y., W. Liu, Y. Li, and W. Cao, *Formation Mechanism of Skin-Core Chemical Structure within Stabilized Polyacrylonitrile Monofilaments.* Nanoscale Res Lett, 2019. **14**(1): p. 93.
36. Clarke, A. and J. Bailey, *Oxidation of acrylic fibres for carbon fibre formation.* Nature, 1973. **243**(5403): p. 146.
37. Gupta, A. and I. Harrison, *New aspects in the oxidative stabilization of PAN-based carbon fibers.* Carbon, 1996. **34**(11): p. 1427-1445.
38. Ouyang, Q., L. Cheng, H. Wang, and K. Li, *Mechanism and kinetics of the stabilization reactions of itaconic acid-modified polyacrylonitrile.* Polymer Degradation and Stability, 2008. **93**(8): p. 1415-1421.

39. Wang, P., *Aspects on prestretching of PAN precursor: Shrinkage and thermal behavior.* Journal of applied polymer science, 1998. **67**(7): p. 1185-1190.
40. Xiao, S., B. Wang, C. Zhao, L. Xu, and B. Chen, *Influence of oxygen on the stabilization reaction of polyacrylonitrile fibers.* Journal of applied polymer science, 2013. **127**(3): p. 2332-2338.
41. Pandey, G.C. and A. Kumar, *Determination of density of oxidized fiber by IR spectroscopy.* Polymer testing, 2002. **21**(4): p. 397-401.
42. Masson, J., *Acrylic fiber technology and applications*. 1995: CRC Press.
43. Frank, E., L.M. Steudle, D. Ingildeev, J.M. Spörl, and M.R. Buchmeiser, *Carbon fibers: precursor systems, processing, structure, and properties.* Angewandte Chemie International Edition, 2014. **53**(21): p. 5262-5298.

CHAPTER 6. THE CARBONIZATION OF HOLLOW PAN-DERIVED FIBERS AND THEIR COMPARISON WITH SOLID CARBON FIBERS

6.1 Introduction

Hollow carbon fibers (HCF) have the potential to improve on traditional solid CF properties by effectively reducing fiber density (resulting in higher specific strength and modulus) which can lead to lighter weight parts. In Chapter One, it was shown that high specific strength and modulus is a central driver of carbon fiber adoption over cheaper materials. HCF success is dependent on their ability to attain or exceed the specific effective tensile properties of the incumbent commercially available solid CF. In HCF it is the effective tensile properties (stress, modulus and density measurements that include the lumen area or volume) that contribute to the properties of the resulting composite structures into which they are incorporated. As reported previously, efforts toward the production of HCF utilizing PAN HF precursors solution spun with a segmented arc spinneret are few, with only three references located after extensive literature review. Of those three, only one produced HCF from the HF precursors, but as it is a patent, no characterization details regarding the process-property-structure relationships, or their development, is given. A better understanding of these relationships and their development is important to realize high tensile property HCF, particularly as they relate to the incumbent traditional solid CF.

The tensile properties of CF in general are highly influenced by defects. These defects can include misalignments in the crystalline structure, which tend to affect fiber modulus, or voids, inclusions, surface imperfections, and chemical structure defects, which are more likely to impact the tensile strength. The skin-core structure is found in most commercial CFs and is detrimental to both the CF tensile strength [1, 2] and modulus [3, 4]. It is hypothesized that the development of HCF, which includes their ability to oxidize from both the interior and exterior, will help to mitigate skin-core formation and will result in improved CF properties. Given that the core of CF is lower modulus than the skin, removing it is hypothesized to result in a true modulus higher than that of the baseline skin-core CF to which it is compared. The lower modulus core is simply increasingly removed with decreasing wall thickness. Here, **it is hypothesized that the true elastic modulus of the HCF will increase as a function of increasing percent open area (for a fixed outer**

diameter) due to the reduction in skin-core structure in the HCF. As described previously, the literature indicates that the majority of commercially available CF contain a skin-core structure, which results in the highly oriented, high modulus skin carrying much of the load [5, 6]. This suggests that the formation of a HCF would more efficiently exploit the oriented portion of the fiber.

In addition, one of the overarching goals of this research is to develop an understanding of how HCF properties compared to those of solid CF. **It is hypothesized that a HCF can conserve the tensile strength of a similar OD solid CF.** This is hypothesized based on findings from other researchers previously discussed in section 1.1.4.2, who found that surface flaws are a major limiting factor in CF tensile strength [1, 2], as the skin carries up to 10 times the stress compared to the core [7] and that reducing or eliminating the skin-core structure would allow for homogeneous stress distribution along the fiber cross section, leading to improved tensile properties [1, 2]. In addition, conservation of tensile strength for hollow glass fibers has already been demonstrated [8].

An investigation of these hypotheses, along with a comparison of the initially developed HCF in this work to literature and benchmark fibers was undertaken in this chapter, to better understand the HCF process-property-structure relationships.

6.2 Experimental

6.2.1 Materials

For the development of HCF, hollow PAN fiber precursors were selected from Table 5.1. For comparison, a high strength, standard modulus (solid) T700S CF (Toray Carbon Fibers America, Inc.) was utilized as a benchmark for several analyses [9].

6.2.2 Oxidation

The oxidation methods used in this chapter are described in section 5.2.2 and are referenced as needed.

6.2.3 Carbonization

For carbonization, a Thermal Technologies graphitization furnace (Thermal Technology LLC, Santa Rosa, CA) was used, capable of ambient to 2800 °C temperature profiles under an inert atmosphere. The graphite rack was designed to have one end fixed, while the other floating end was capable of sliding along graphite rods. A schematic of the carbonization system is shown in Figure 6.1. Six hoops (three on each side) of oxidized fiber were placed on this graphite rack, which was then placed within graphitization oven. The floating end of the graphite rack was attached via wire to a 100 g mass to apply strain to the fiber during carbonization. The wire passed through a septum in order to maintain separation of the inert atmosphere within the furnace and the lab atmosphere. A schematic of the carbonization system is shown in Figure 6.1. Fibers were heated in nitrogen from room temperature to 1300 °C at 5 °C/min and held isothermal at 1300 °C for 10 min., similar to [10].

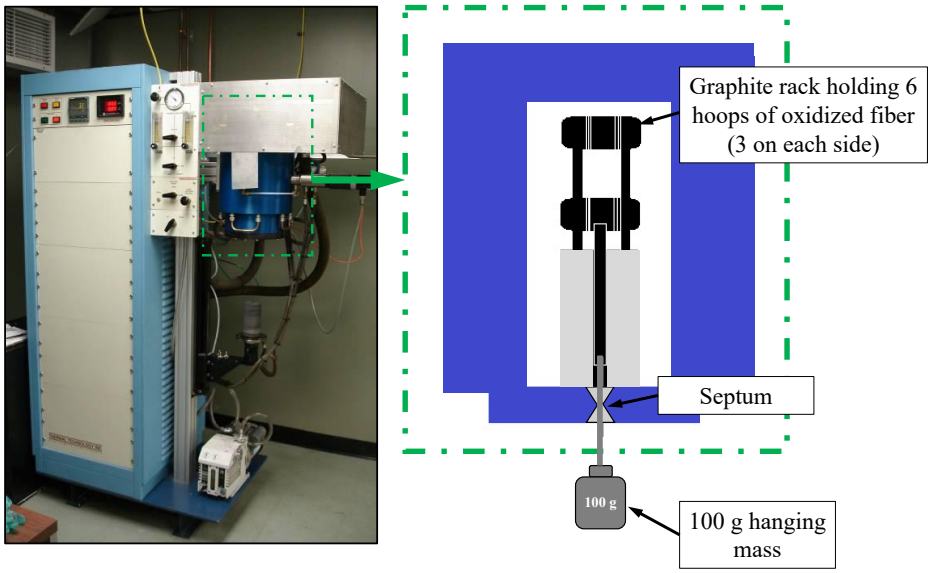

Figure 6.1. A schematic of the carbonization system used during the study, where oxidized fiber was placed on a graphite rack and subjected to a 100 g hanging mass during thermal conversion in an inert atmosphere.

6.3 Results and discussion

6.3.1 Initial analyses of hollow carbon fibers

An analysis of HCF was undertaken to examine their cross section structure, as well as their structural parameters, crystalline orientation, and tensile properties.

6.3.1.1 Morphology and dimensions

An initial analysis of HCF morphology was completed by carbonizing HF from run 497A, B, C, and D precursors, which were produced from the same spinning run with varying total draw ratios of 5x, 12x, 27x, and 32x, respectively. Following oxidation and carbonization, the resulting HCF did not collapse and remained hollow, as shown in Figure 6.2 below. The resulting outer diameters, inner diameters, and effective fiber densities are shown in Table 6.1.

The smallest HCF produced, 497D HCF, measured 35 μm outer diameter and 22 μm inner diameter (6.5 μm wall thickness), with an effective fiber density of 1.1 g/cc, as shown in Table 6.1. Reduced effective density (below the typical 1.8 g/cc for traditional solid CF) is beneficial for increasing the specific tensile properties of the HCF and could result in superior specific tensile properties of the HCF relative to solid CF.

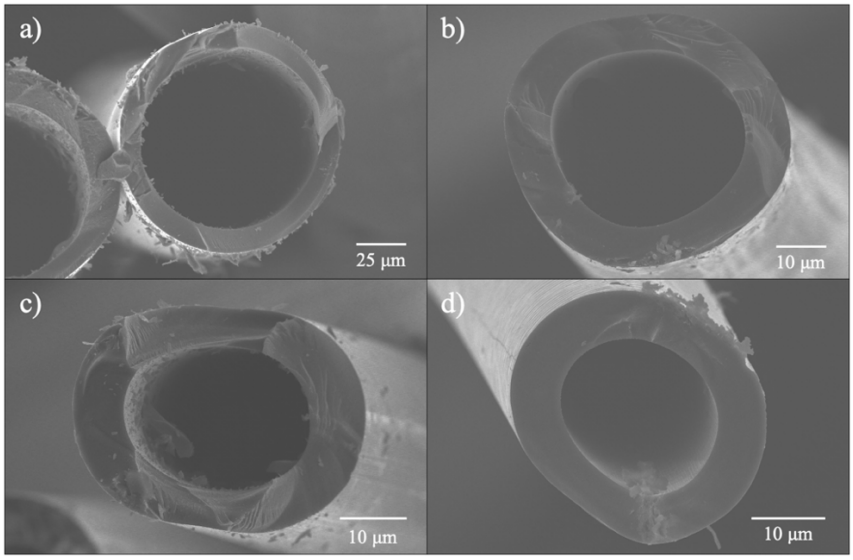

Figure 6.2. SEM micrographs of hollow carbon fiber (HCF) cross sections stemming from run 497 precursors. (a) 497A derived HCF; (b) 497B derived HCF; (c) 497C derived HCF; (d) 497D derived HCF. From the author's original work [11], reprinted with permission.

Table 6.1. Dimensions and effective densities of the HCF samples derived from 497A, B, C, and D precursors.

HCF Sample	Outer Diameter (µm)	Inner Diameter (µm)	Effective Density (g/cc)
497A	110	82	0.8
497B	59	39	1
497C	36	23	1.1
497D	35	22	1.1

6.3.1.2 Structural parameters and crystalline orientation

The resulting HCF structural parameters and crystalline orientation are shown in Table 6.2 and are compared to benchmark T700S carbon fiber properties. The carbonized fibers have two distinct peaks at 2θ ~26° and ~43°, corresponding to the (002) and (100) planes of the graphitic carbon structure, respectively. The results in Table 6.2 show that the average crystallite length $L_{a_{(100)}}$ and crystallite thickness $L_{c_{(002)}}$ both increased with increasing precursor draw ratio and decreasing HCF diameters. In addition, the d-spacing, $d_{(002)}$, was also found, in general, to decrease and the Herman's orientation factor, $f_{(002)}$ to increase with increasing precursor draw ratio. Each of these structural parameter trends

has been related to an increase in the tensile modulus of the resulting CF, where larger crystallites separated by a shorter distance between two successive layers ($d_{(002)}$) have been shown to contribute to higher modulus in the resulting CF. The increasing Herman's orientation factor signals a more pronounced orientation in the fiber axis direction [12]. These results indicate an increasing degree of anisotropy in the HCF with increasing precursor draw ratio. The 497D HCF crystallite sizes, d-spacing, and Herman's orientation factor were all higher compared to the T700S benchmark CF. Large, densely packed crystallites have been correlated to high tensile modulus and lower tensile strength [13, 14]. T700S CF is known to be a standard modulus, high strength CF and therefore the results presented here for the HCF may point toward the HCF prioritizing higher modulus over tensile strength. The tensile properties of the HCF are discussed in the following section.

Table 6.2. XRD structural parameters and crystalline orientation of 497A, B, C, and D hollow carbon fiber compared to T700S carbon fiber.

Carbon Fiber	$2\theta_{(002)}$ (°)	$2\theta_{(100)}$ (°)	$d_{(002)}$ (nm)	$L_{a(100)}$ (nm)	$L_{c(002)}$ (nm)	$f_{(002)}$ (°C)
497A HCF	25.36	43.67	0.3510	2.67	1.31	0.588
497B HCF	25.83	43.73	0.3447	2.70	1.32	0.704
497C HCF	25.55	43.47	0.3484	2.96	1.45	0.744
497D HCF	25.73	43.24	0.3460	2.96	1.45	0.799
T700S	25.85	43.49	0.3444	2.67	1.30	0.783

6.3.1.3 Tensile properties

The specific effective tensile properties for the HCF samples are shown in Figure 6.3 and Figure 6.4. (Note that effective tensile properties (non-specific) can be found in Table A - 1 in the Appendix). These HCF tensile properties were compared to large diameter solid carbon fibers found in the literature as well as to a commercial baseline of T700S CF [9]. Ideally, comparisons of tensile properties are completed on fibers with similar OD. With decreases in fiber diameter, there has been shown to be a corresponding increase in tensile strength [15]. A larger diameter filament allows more volume in which strength limiting defects can occur. The HCF here range from 110 to 35 μm OD, while traditional solid CF such as T700S have diameters of 7 μm. It is difficult to find references for large diameter solid CF in the literature, particularly for comparison with these large

diameter HCF. Large diameter CF are not commonly produced due to the inherent difficulty in their production as well as the difficulty in producing high tensile properties from large diameter fibers. However, references to two such fibers were found, with diameters of 16 μm (by Mitsubishi [16]) and 12 μm (by Chae et al. [17]). Still, these CF diameters are much smaller than the smallest HCF here, which had an outer diameter of 35 μm (497D HCF).

The specific effective tensile strength of the HCF increases with decreasing OD and ID, ultimately reaching an average specific effective strength of 0.54 N/tex (497D HCF). This specific strength remains lower than the 16 μm diameter CF by Mitsubishi (2.0 N/tex) and the 12 μm diameter CF by Chae (1.1 N/tex) and is significantly lower than the 2.7 N/tex for T700S CF, which measures 7 μm in diameter. As stated previously, with decreases in fiber diameter, there has been shown to be a corresponding increase in tensile strength [15], similar to what is observed here. A smaller diameter allows for less room for defects and the tensile strength of CF increases with decreasing diameter. The tensile strength of CF is known to be negatively impacted by the presence of defects and flaws, including foreign particles, voids, or other imperfections [18, 19]. This has been explained using the Griffith fracture theory where flaw density on/in the fiber gauge length decreases as the filament is drawn to a finer diameter. Therefore strength goes up. Here, drawn to its theoretical maximum, a single molecular chain would possess the highest strength because such a structure could tolerate no defects [20]. Highly drawn, finer filaments ultimately results in fewer defects per unit length.

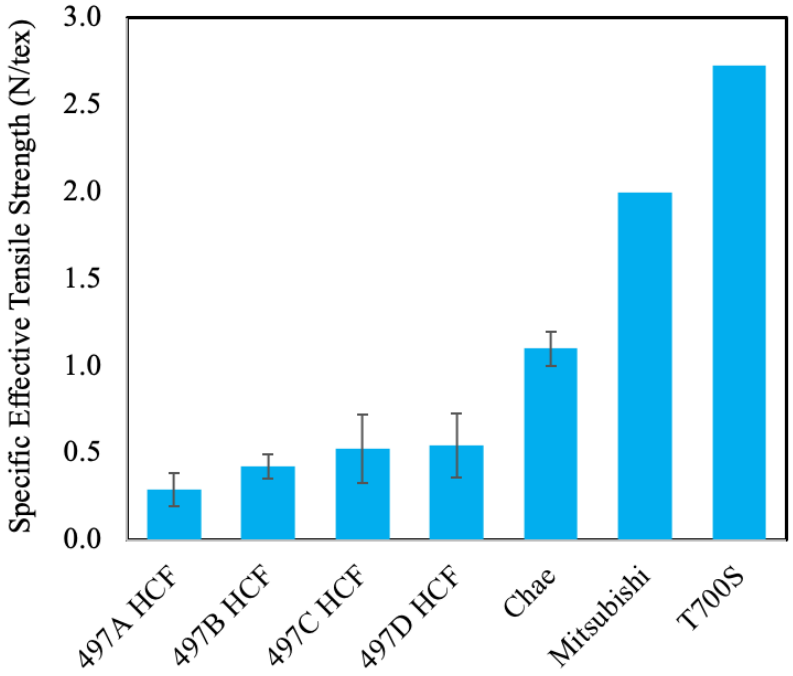

Figure 6.3. Specific effective tensile strength for HCF samples compared to large diameter carbon fibers and T700S carbon fiber. From the author's original work [11], reprinted with permission.

It is important to recall as well that macrovoid defects measuring 5-7 μm in diameter appeared occasionally in the walls of the HF precursors (see Figure 4.8c), which were hypothesized to stem from instantaneous de-mixing in the 100% water coagulation process. These defects greatly reduce the fiber tensile strength. On the contrary, the significantly higher strength T700S CF has been found to contain only very small 1-4 nm pores [4]. Also, recall from Figure 4.14 that run 497D precursor fiber contained 25.8 wt.% residual liquid content and that removal of residual liquid (and in particular residual solvent) is vital to the production of high tensile property CF as residual solvent acts as an impurity during thermal treatment and contributes to discontinuities in ladder formation [21], imperfect crystalline structure [22], and fiber breakage. The high residual liquid content in run 497D precursor (and assumed 497A, B, and C precursors as well) may have also had a detrimental impact during thermal treatment. Therefore, in addition to attenuation in diameter to reduce the available volume of material in which defects and voids can exist, significant reductions in void size are necessary in order to produce HCF

with tensile strength approaching or exceeding T700S properties, as is a reduction in residual solvent within the precursor,

Unlike tensile strength, the elastic modulus of CF is not as sensitive to void content but depends more upon the crystallographic orientation within the fiber. Orientation of CF crystallites is influenced by the molecular orientation of the precursor fibers (achieved by drawing) as well as strain experienced during the thermal conversion process. The resulting specific effective elastic modulus results for the HCF are shown in Figure 6.4. Recall that the draw ratios for the 497A, B, C, and D precursors were 5x, 12x, 27x, and 32x, respectively. In this case, the HCF modulus is observed to increase as the precursor draw ratio increases. The draw ratios for the 497C and 497D precursors were similar enough (27x and 32x) that the elastic moduli of the resulting HCF were also similar, although the 497C HCF specific effective elastic modulus was slightly higher, at 125 N/tex, compared to 120 N/tex for 497D HCF. Comparatively, the specific effective elastic moduli for the CF of Chae, Mitsubishi, and T700S were 147 N/tex, 129 N/tex, and 136 N/tex, respectively.

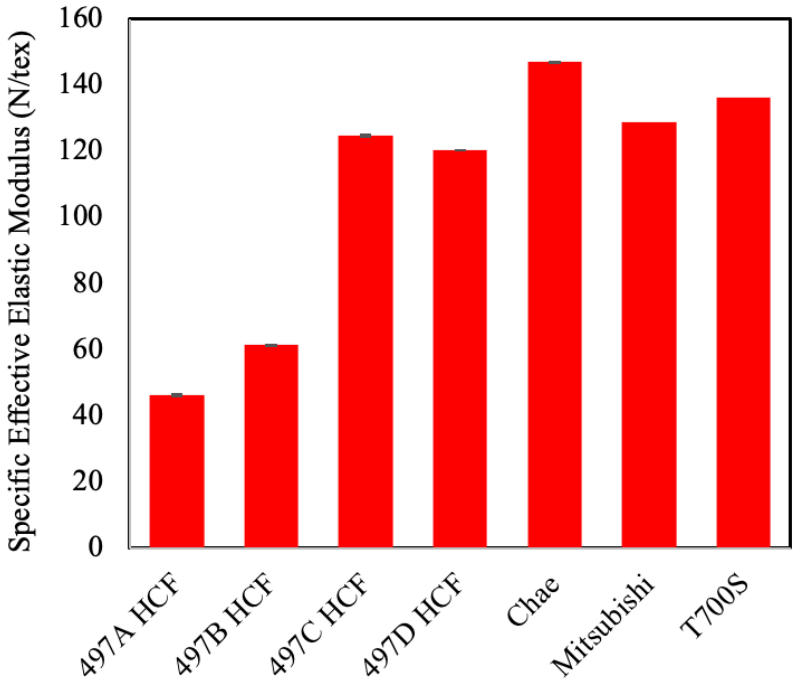

Figure 6.4. Specific effective elastic modulus for HCF samples compared to large diameter carbon fibers and T700S carbon fiber. From the author's original work [11], reprinted with permission.

These results indicate that the specific effective elastic modulus of the HCF is currently only 8% lower than that of T700S. In addition, it is important to remember that the HCF produced here utilized a batch thermal conversion method as opposed to the superior continuous oxidation and carbonization methods used to produce commercial CF such as T700S. The use of a continuous thermal process is important for applying varying degrees of strain which further enhance the crystalline alignment and positively impact the resulting modulus. Therefore, it is possible that the use of a continuous thermal conversion method in developing the HCF could result in HCF with specific effective elastic modulus much greater than T700S. However, as it stands, the current data supports the conservation of specific effective elastic modulus properties of commercial CF utilizing a HCF.

6.3.2 Impact of percent open area on HCF true elastic modulus

In section 5.3.3, it was found that the skin-core structure in the oxidized HF was generally reduced in fibers with higher percent open area of the HF. A higher percent open

area of the HF meant a larger lumen volume in which air was contained and therefore a corresponding large volume of oxygen available for oxidation from the interior of the HF. Improved oxidation from the interior of the HF resulted in a reduction in the skin-core structure within the oxidized HF wall. The reduction in skin-core structure, and in particular the core structure, is preferred, as it is known that the skin of PAN-based CF has been found to be higher modulus than the core [6, 23]. Therefore, removal of core material may result in increases in elastic modulus for the fiber. This leads to one of the overarching hypotheses of this work, which is that the **true elastic modulus of the HCF will increase as a function of increasing percent open area (for a fixed outer diameter) due to the reduction in skin-core structure in the HCF.** In this section, examination of the true elastic modulus of the HCF will be explored.

6.3.2.1 Fiber processing

To study the impact of increasing percent open area on the true elastic modulus in the resulting HCF, precursor HF with appropriate dimensions were selected from in-house spun HF. These are listed in Table 5.1. (Arbitrary OD/ID combinations were not possible given the spinning processing and current limitations thereof.) In an ideal case, HF with the same outer diameter and varying percent open area would be selected. However, due to the limited number of HF available for study, fibers with similar wall thickness and varying percent open area were chosen and are shown in Table 6.3. The fibers chosen, 506, 497C, and 490B had average open areas of 20, 33, and 39%, respectively, with wall thicknesses ranging from 12.1 to 12.7 μm. Scanning electron micrographs of the precursor cross sections are shown in Figure 6.5. As all these fibers under study were spun with TP1 into a 100% water bath, the fibers all contained some fraction of macrovoids. Fibers also show some evidence of fiber fusion. Following oxidation and carbonization, the resulting HCF tensile properties were analyzed.

Table 6.3. Precursor HF with varying percent open area and similar wall thickness selected for conversion to HCF for study of true elastic modulus. (N ≥ 7 for each fiber)

Precursor Fiber	Outer Diameter (μm)	Inner Diameter (μm)	Wall Thickness (μm)	Open Area (%)
506	46 ± 1	21 ± 2	12.7 ± 0.8	20 ± 3
497C	58 ± 1.5	33 ± 2	12.2 ± 0.6	33 ± 3
490B	64 ± 4	40 ± 4	12.1 ± 0.8	39 ± 5

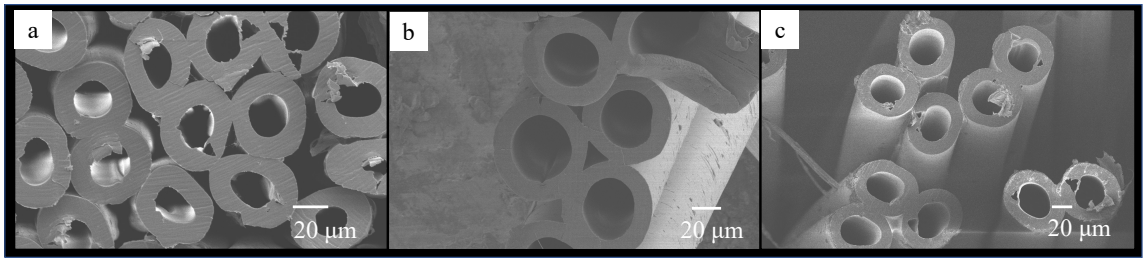

Figure 6.5. Scanning electron micrographs of precursor cross sections. (a) 506; (b) 490B; (c) 497C.

6.3.2.2 Hollow carbon fiber tensile properties

The resulting HCF tensile properties are shown in Table 6.4. The HF experienced a reduction in inner and outer diameter during thermal treatment, resulting in an increase in the average percent open area in the resulting HCF. Following carbonization, the resulting 497C and 490B HCF had similar dimensions, each being reduced to a 38 μm outer diameter and a 25 μm inner diameter, resulting in 42 and 43% open area, respectively. The 497C HCF and 490B HCF true elastic moduli were 89 and 91 GPa, respectively. Comparatively, the 506 HCF open area was 31% with a 113 GPa true elastic modulus. This result is contrary to the proposed hypothesis, which postulated that true modulus would increase with increasing percent open area.

Table 6.4. Tensile properties of selected hollow carbon fibers.

Hollow Carbon Fiber	Outer Diameter (μm)	Inner Diameter (μm)	Open Area (%)	Effective Tensile Strength (MPa)	Effective Modulus (GPa)	True Tensile Strength (MPa)	True Modulus (GPa)
506	29	16	31	755	78	1093	113
497C	38	25	42	379	52	650	89
490B	38	25	43	438	52	765	91

6.3.2.3 Evaluation of experimental parameters

While contrary to the proposed hypothesis, several factors should be considered when interpreting the above results. First, the hypothesis under examination postulated an increase in true elastic modulus with increasing percent open area *for a fixed outer diameter*. Currently, the spinning process is not yet matured to the point that it is possible to spin a HF with a targeted OD, much less a targeted OD *and* targeted percent open area. Therefore, selection of fibers for evaluation of the hypothesis relied on the HF listed in Table 5.1. It was difficult to find fiber combinations with the same outer diameter and significantly different percent open areas and therefore fibers with similar wall thicknesses and varying percent open area were chosen (490B, 497C, and 506 HF). For a set wall thickness (in this case 12.1 to 12.7 μm), it was hypothesized that the skin-core structure in the fiber wall would decrease from 506 HF to 497C HF to 490B HF as their respective percent open areas increased from 20 to 33 to 39%. In fact, this was previously found to be true for 506, 497C, and 490B HF in section 5.3.3, where the skin-core structure was reduced by improved oxidation from the interior of the HF with greater percent open area (see Figure 5.8 and Figure 5.9). The result of this decrease in skin-core structure was hypothesized to be evident in the elastic modulus of the resulting HCF.

A second complicating factor in the interpretation of the above results, and perhaps most importantly, is that the elastic modulus of precursor and CF is highly impacted by the draw the fibers experiences during spinning and thermal processing, as this impacts the alignment of the molecular and crystalline structures [24]. Looking back at the fiber spinning conditions for the precursors listed in Table 6.4, all were spun from the same HF-A spinneret but with varying draw ratios. Therefore, the modulus of the precursor fibers would be expected to be different based on draw ratio alone, which is then carried over to the resulting HCF.

In conclusion, optimal experimental design was hindered given the limitations of the current spinning process and the limited HF dimensions available, which complicated the ability to accurately test the hypothesis. To better evaluate the hypothesis, it is important to spin HF precursors utilizing the same draw ratios. And, in order to vary the percent open area while maintaining draw ratio and outer diameter, multiple spinnerets with varying

percent open area would need to be designed and machined. The generation of precursor fibers with the same outer diameter, draw ratio, and varying percent open area is in no way trivial and would require extensive development. If successful in their production, the HF precursors could then be thermally converted to HCF under the same conditions and their tensile properties analyzed. This would provide the most accurate test of the true elastic modulus vs percent open area hypothesis. Despite not having a clear answer with respect to the original hypothesis, it should be noted that HCF generated from this experiment had the highest tensile properties of any produced so far this study. The 506 HCF measured 29 μm outer diameter and 16 μm inner diameter, with a 31% open area and had an effective tensile strength of 755 MPa and an effective elastic modulus of 78 GPa. The previously produced HCF with the highest tensile properties was 497D HCF, with a 568 MPa effective tensile strength and 132 GPa effective elastic modulus (Table A - 1).

6.3.3 Comparison of hollow and solid carbon fibers

As part of the previous experiment, the tensile properties of the HCF generated from run 497 precursors were compared to "large" diameter solid carbon fibers found in the literature. The solid CF of Chae et al. measured 12 μm [17] and the solid CF by Mitsubishi measured 16 μm [16]. It is difficult to draw direct comparisons between these fibers and the HCF generated here when the smallest HCF produced from run 497D measured 35 μm in outer diameter, particularly knowing that fiber diameter has a significant impact on tensile strength [18, 19]. A more accurate comparison can be made between fibers of similar diameter which have undergone similar processing steps. In this section, the development of a HCF is compared to the development of a solid carbon fiber with similar diameter which has been exposed to similar processing steps.

6.3.3.1 Precursors

For this study, precursors from run 571A (hollow) and run 549A (solid) were utilized. Their dimensions are listed in Table 5.2. The outer diameters of both fibers were 78 μm. Scanning electron micrographs of the fibers are shown in Figure 6.6. The HF precursors from run 571A in Figure 6.6a are split along the fiber axis and some of the lumen are filled with residual matrix compound. Both are artifacts of the fiber sectioning process for fiber

imaging (see section 3.2) and are not found in the resulting oxidized or carbonized fibers. The HF macrovoid content may be slightly reduced as the fiber was spun into a 10 wt.% DMSO/water bath compared to the 100% water bath utilized for other HF. However, the void content was difficult to quantify, but negligible macrovoids were observed in the HF cross sections in Figure 6.6a.

The solid precursor fibers from run 549A are shown in Figure 6.6b and contained voids of varying dimension preferentially concentrated just inside the fiber perimeter. The true densities of the hollow and solid precursor fibers were measured to be 1.18 g/cc and 1.13 g/cc, respectively. This result indicated that the solid 549A precursor fibers contained a higher void content than did the 571A HF precursors.

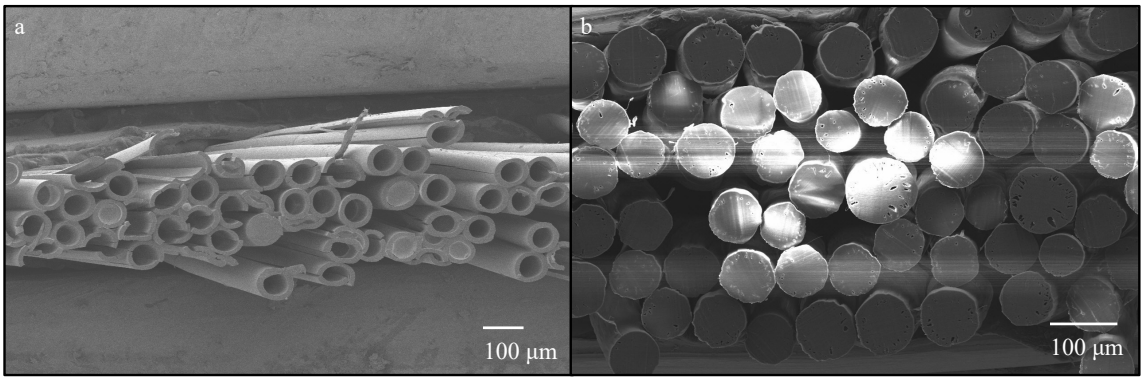

Figure 6.6. Scanning electron micrographs showing cross sections of 78 μm diameter hollow and solid precursor fibers. (a) Run 571A hollow precursors. (b) Run 549A solid precursors.

6.3.3.2 Oxidation

The hollow and solid precursors were oxidized and the resulting fibers embedded in epoxy and viewed using a 50x oil objective (500x magnification) in reflected white light. The optical micrographs are shown in Figure 6.7. In Figure 6.7a, the oxidized HF derived from run 571A are shown. The light blue skin regions were seen on both the interior and exterior, with a darker blue core seen in the center of the fiber wall. In some cases, the wall cores reflected a bright orange color. The oxidized solid fibers shown in Figure 6.7b also had a light blue skin about the fiber circumference but a very large portion of the cross

section was bright orange and/or darker blue. In addition, the oxidized fiber skin was not a consistent thickness about the cross section, as it was with the HF, but rather tended to increase in thickness as it followed the void structure of the fiber. It is hypothesized that the voids in this case contained air, which contributed to the oxidation of the solid fiber (as discussed previously in section 5.3.4). Magnified views of optical micrographs of oxidized 549A solid fiber in Figure 6.8 show isolated pores (white arrows) with an oxidized perimeter (shown in light blue) as a result of air trapped within the void, supporting this hypothesis.

Observation of the oxidized fiber surfaces using SEM revealed significant differences in morphology, as shown in Figure 6.9. The surfaces of the oxidized HF were smooth (Figure 6.9a) while the oxidized solid fibers were much more fibrillar in nature and showed some depressions on the surface, likely due to the high void content of the fiber.

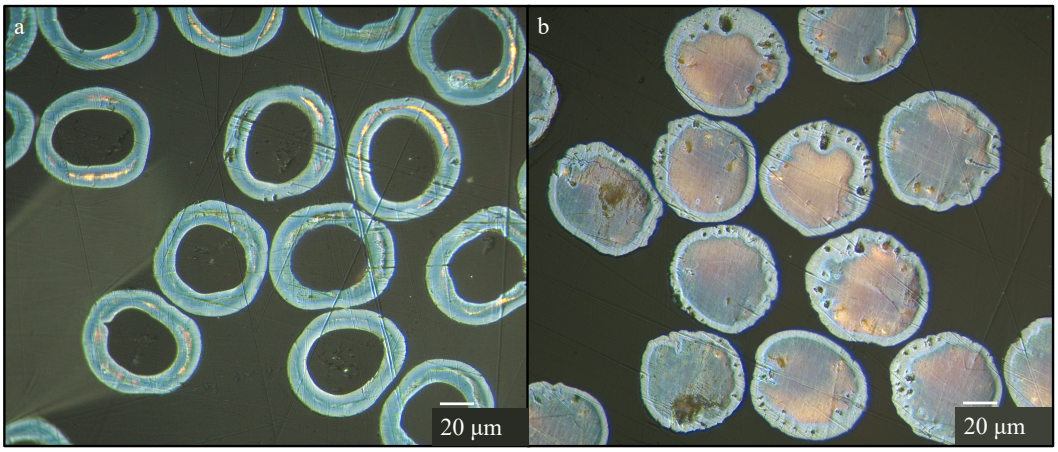

Figure 6.7. Optical micrographs (50x oil objective, 500x magnification) showing cross sections of oxidatively stabilized hollow and solid precursor fibers. (a) Run 571A hollow precursors. (b) Run 549A solid precursors.

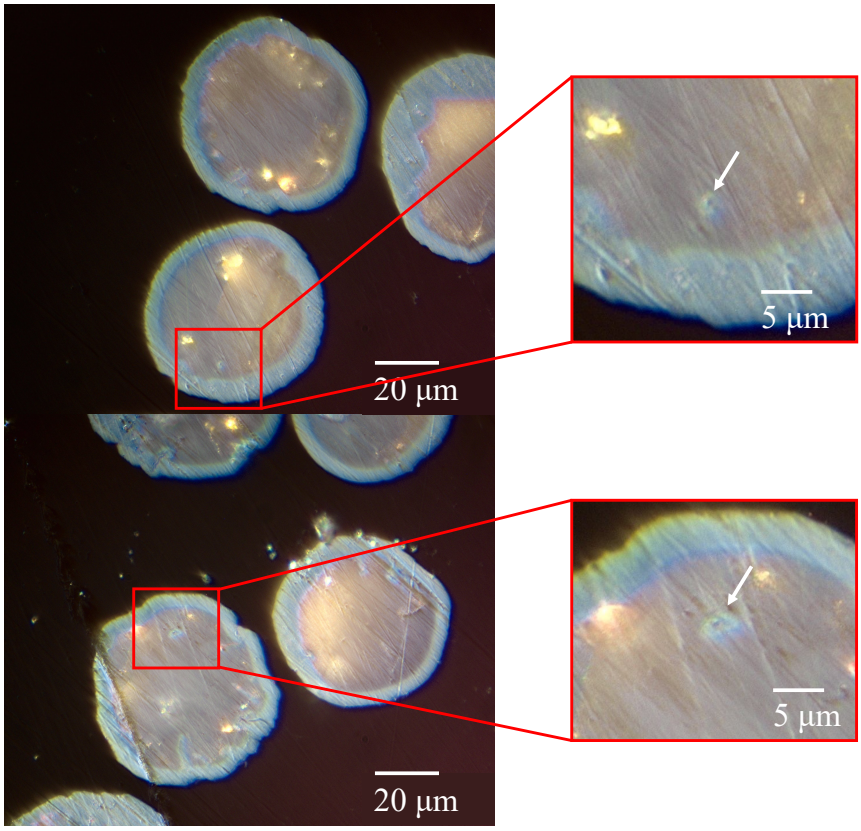

Figure 6.8. Optical micrographs of oxidized 549A solid cross sections showing magnified views of isolated pores (white arrows) with an oxidized perimeter (shown in light blue) as a result of air trapped within the void.

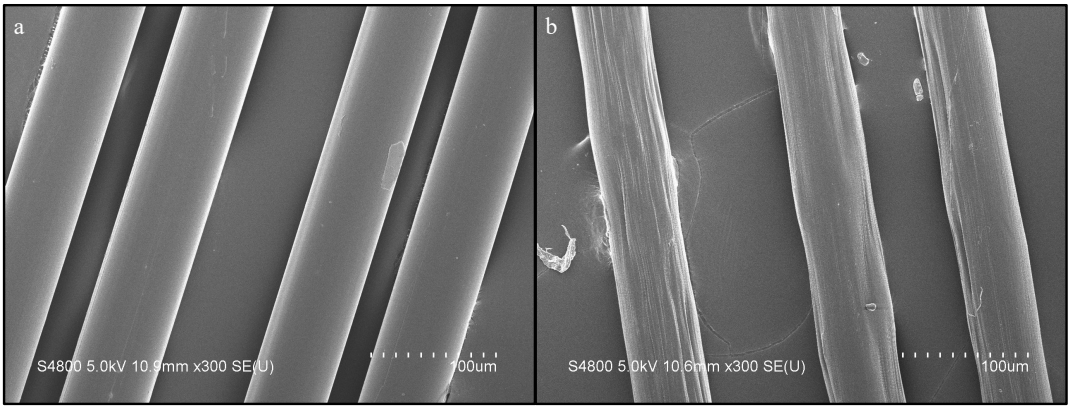

Figure 6.9. Scanning electron micrographs of the oxidatively stabilized hollow and solid precursor fiber surfaces. (a) Run 571A hollow precursors. (b) Run 549A solid precursors.

6.3.3.3 Carbonization

Following oxidation, carbonization of the fibers was attempted. However, the 549A solid fibers could not survive the carbonization process when subjected to the 100 g hanging mass typically used (see Figure 6.1). As a result, both the oxidized 571A HF and 549A solid fibers were cut from the graphite rack following oxidation, wrapped in graphite foil, and carbonized without tension. The resulting carbon fiber tensile properties are shown in Table 6.5. The effective tensile strength of the 571A HCF was 8x higher than the 549A solid CF, with an effective tensile strength of 532.9 ± 197.4 MPa. The effective elastic modulus and break strain were 2x and 4x higher for the 571A HCF, respectively. In general, the HCF greatly outperformed the solid fibers when their starting precursors were of the same outer diameter and subsequent thermal treatments were carried out simultaneously.

Table 6.5. Tensile properties of the carbonized 571A HCF and 549A solid CF.

Carbon Fiber	Effective Tensile Strength (MPa)	Stdev (MPa)	Effective Elastic Modulus (GPa)	Stdev (GPa)	Break Strain (%)	Stdev (%)
571A HCF	532.9	197.4	34.4	2.0	1.50	0.50
549A solid CF	66.3	42.6	17.4	8.5	0.37	0.11

Of interest, however, were the observations made regarding the morphology of the carbonized filaments. Examples of 571A HCF cross sections are shown in Figure 6.10. The HCF were quite circular with consistent wall thickness. Examination of the cross sections of the solid CF derived from run 549A in Figure 6.11 revealed a significant increase in macrovoid size and concentration. The oxidized solid fibers shown in Figure 6.7b contained voids, but those void diameters are on the 100s of nanometers scale, with perhaps a few on the 1s of micron scale. They were also concentrated heavily around the periphery of the fiber diameter. However, following carbonization, the carbonized solid fibers in Figure 6.11 contained macrovoids on the order of 10s of microns in diameter, with many of the largest voids reaching the fiber center.

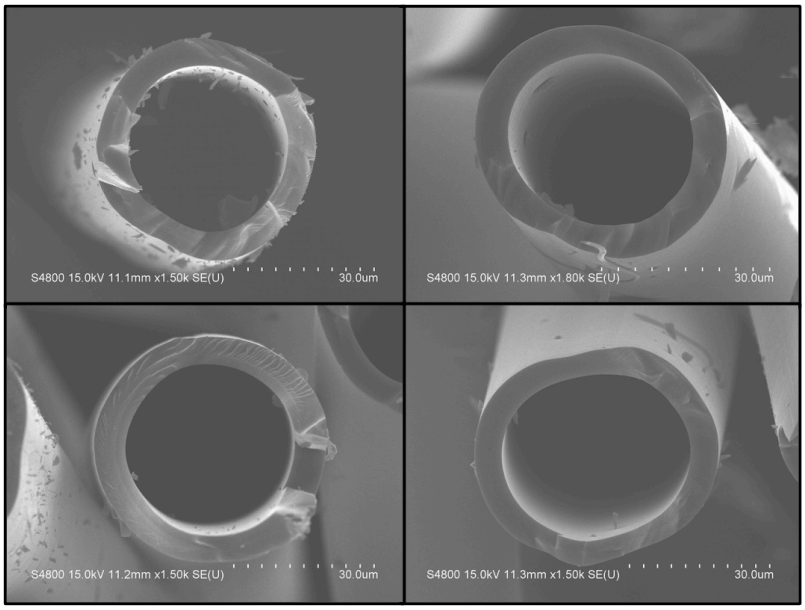

Figure 6.10. Scanning electron micrographs of HCF cross sections derived from run 571A HF.

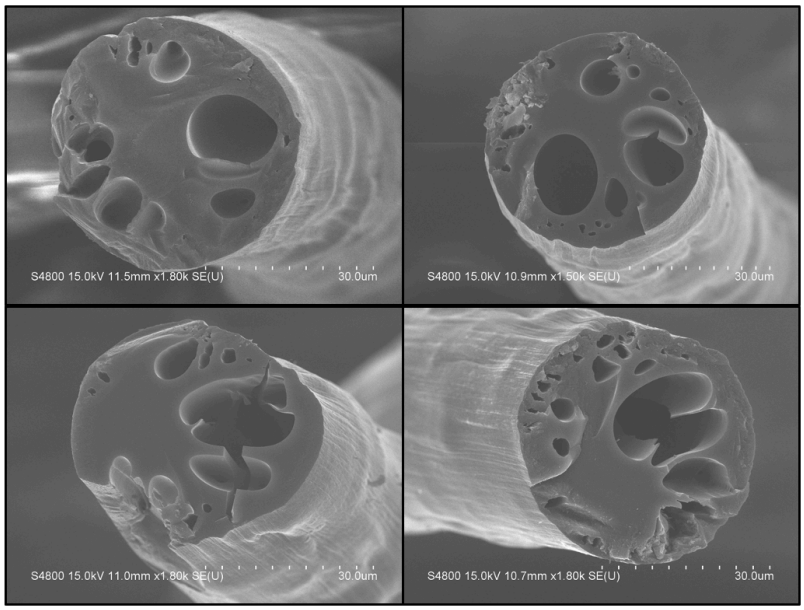

Figure 6.11. Scanning electron micrographs of solid CF cross sections derived from run 549A solid fiber.

Further observation of the solid carbon fiber surfaces in Figure 6.12 revealed the startling realization that significant damage to the fibers had occurred. The solid carbon fibers shown in Figure 6.12 were missing large portions of material, so much so that the

core of the fiber was visible in some instances. Based on this observation, it was hypothesized that during carbonization, the core material was vaporized, resulting in violent bursting of the fiber skin as the volatized material attempted to escape the fiber. Core vaporization has been shown to occur for fibers with highly under-oxidized cores [1, 25]. This resulted in the damage seen in Figure 6.12. It is clear that this type of extensive damage would significantly reduce the tensile properties of the resulting CF, as has been shown in Table 6.5.

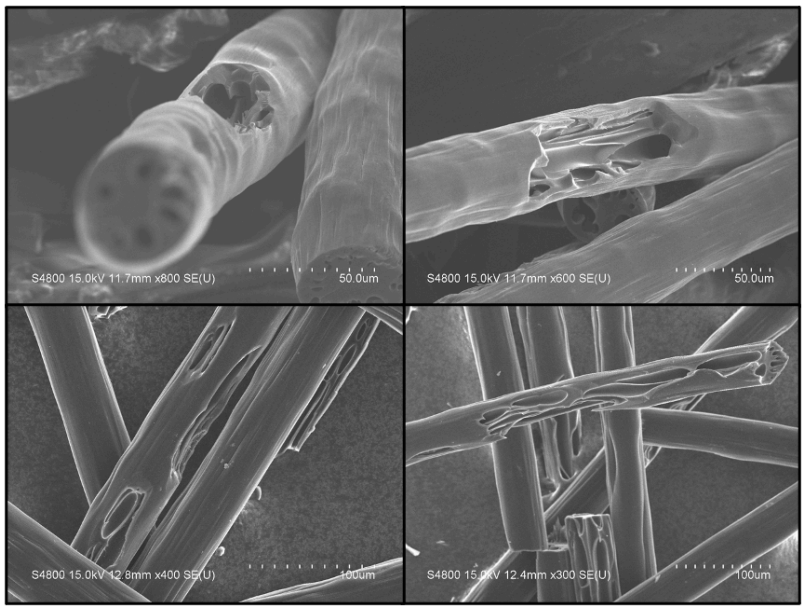

Figure 6.12. Scanning electron micrographs of solid CF surfaces derived from run 549A solid fiber.

In summary, the comparison of HF and solid fiber of the same outer diameter yielded interesting results. First, the difficulty in spinning a large diameter solid precursor fiber (78 μm) was noted. The resulting solid fiber was of lower true density (1.13 g/cc) compared to the HF precursor true density (1.18 g/cc). The difference in densities was attributed to the presence of voids concentrated around the fiber perimeter. These voids were the result of inadequate drawing and void collapse, which was avoided during spinning to keep the fiber large. Second, when oxidized, the HF oxidized from both the interior and exterior, resulting in a slight skin-core structure within the wall. However, the solid fiber displayed a significant skin-core structure with what was later found to be a highly under-oxidized

core. The large diameter of the solid fiber likely hindered the ability of oxygen to diffuse to the fiber core. Third, the resulting solid CF experienced significant damage during carbonization. Here, vaporization of the under-oxidized core burst through the fiber walls in sections. Meanwhile, the resulting HCF had concentric, round annular cross sections with comparatively fewer visible flaws. As a result, the HCF effective tensile strength and effective tensile modulus were 8x and 2x higher than the solid CF. In this case, the HF demonstrated significant advantages over the solid, primarily due to its ability to oxidize from both the interior and exterior.

It is hypothesized that the magnitude of difference between tensile properties may decrease with decreasing fiber outer diameter. In other words, as the solid fiber diameter decreases, the solid fiber skin-core structure will be reduced and vaporization of the interior core material less likely to occur. With vaporization less likely to occur, or not occurring, as in the case of more traditional solid precursor diameters (12-14 μm), tensile properties of the resulting solid CF will increase. Therefore, the difference in magnitude between tensile properties of the solid CF and HCF will be commensurately reduced. However, to what extent remains to be seen.

Additionally, the current effective tensile properties of the HCF are low relative to traditional solid CF, however, the large diameters of the HCF renders comparison between the two non-optimal. As HCF outer diameters and wall thicknesses are reduced in future work, the effective tensile properties are hypothesized to increase, similar to trends seen in the precursor HF (Figure 4.17). However, true evaluation of these hypotheses will require the production of smaller diameter HF precursors (and their corresponding solid counterparts), which will be the subject of future work.

6.4 Conclusions

Utilizing the precursors developed in Chapter 4 and the oxidation knowledge discussed in Chapter 5, HCF were produced and studied. Initial carbonization results revealed that the fiber retained their hollow structure following carbonization. The HCF possessed a larger crystallite length and thickness compared to T700S, with a slightly higher Herman's orientation factor and d-spacing. The impact of these structural and orientational parameters was seen in the resulting HCF specific effective elastic modulus

of 125 N/tex, which was similar to that of T700S at 136 N/tex. Tensile strength, however, was limited by the large fiber diameters and macrovoid content.

Further work was conducted in an attempt to determine if the true elastic modulus of the HCF would increase as a function of increasing percent open area (for a fixed outer diameter) due to the reduction in skin-core structure in the HCF. Unfortunately, limitations in the availability of precursor fibers with appropriate outer diameter, percent open area, and draw ratios hindered the ability to accurately test the hypothesis. However, the best HCF produced (506 HCF) measured 29 μm OD and 16 μm ID, with 755 MPa effective tensile strength and an effective elastic modulus of 78 GPa and represented the best HCF produced in the study.

Finally, it was found that when HF was thermally processed with a similar large diameter solid fiber, the HF was able to oxidize from both the interior and exterior, resulting in a slight skin-core structure within the fiber wall. However, the core of the large diameter solid fiber was quite large. This resulted in vaporization of material during carbonization and drastically reduced the tensile properties of the solid CF. The HCF, on the contrary, was 8x higher in effective tensile strength and 2x higher in effective elastic modulus due to its ability to oxidize from both the interior and exterior. This result indicates that HF outperforms solid fiber when compared at the same outer diameter for relatively large outer diameters, potentially paving the way toward HCF with large OD over traditional solid fiber.

6.5 Future work

Improvement of the HCF effective tensile strength will encourage their widespread application. Their effective tensile strength should meet or exceed that of incumbent solid CF such as T700S to warrant its replacement in high performance composite structures. Currently, the effective elastic modulus is on par with T700S. But again, the real challenge is tensile strength. Tensile strength is known to increase with a decrease in fiber diameter as well as reductions in void and flaw content within the fiber. To date, the best HCF strength produced by these methods represents just 15% of the strength of T700S.

To further improve the resulting HCF properties, significant reductions in precursor HF outer diameter and wall thickness must be made. This could be achieved through improved drawing, but most likely will require spinneret redesigns to reduce the spinneret capillary dimensions (within machinable limits). Reduced wall thickness will result in a reduced skin-core structure, which will improve tensile properties. Work should also focus on modifying the coagulation process to mitigate the formation of macrovoids and reduce the amount of residual liquid (including residual solvent) within the precursor fiber. In general, judicious and tedious process engineering will be required to reduce flaw populations and severity in and on the fibers to achieve high tensile strength. In all, the above mentioned suggestions should result in significant increases in the tensile strengths of the HCF.

6.6 References

1. Liu, J., Z. Yue, and H. Fong, *Continuous nanoscale carbon fibers with superior mechanical strength.* Small, 2009. **5**(5): p. 536-42.
2. Liu, F., H. Wang, L. Xue, L. Fan, and Z. Zhu, *Effect of microstructure on the mechanical properties of PAN-based carbon fibers during high-temperature graphitization.* Journal of Materials Science, 2008. **43**(12): p. 4316-4322.
3. Chen, L., L. Hao, S. Liu, G. Ding, X. Sun, W. Zhang, F. Li, W. Jiao, F. Yang, Z. Xu, R. Wang, and X. He, *Modulus distribution in polyacrylonitrile-based carbon fiber monofilaments.* Carbon, 2020. **157**: p. 47-54.
4. Morris, E.A., M.C. Weisenberger, M.G. Abdallah, F. Vautard, H. Grappe, S. Ozcan, F.L. Paulauskas, C. Eberle, D. Jackson, S.J. Mecham, and A.K. Naskar, *High performance carbon fibers from very high molecular weight polyacrylonitrile precursors.* Carbon, 2016. **101**: p. 245-252.
5. Huang, Y. and R.J. Young, *Effect of Fibre Microstructure Upon the Modulus of PAN- and Pitch-Based Carbon Fibres.* Carbon, 1995. **33**(2): p. 91-107.
6. Liu, X., C. Zhu, J. Guo, Q. Liu, H. Dong, Y. Gu, R. Liu, N. Zhao, Z. Zhang, and J. Xu, *Nanoscale dynamic mechanical imaging of the skin–core difference: From PAN precursors to carbon fibers.* Materials Letters, 2014. **128**: p. 417-420.
7. Kobayashi, T., K. Sumiya, Y. Fujii, M. Fujie, T. Takahagi, and K. Tashiro, *Stress concentration in carbon fiber revealed by the quantitative analysis of X-ray crystallite modulus and Raman peak shift evaluated for the variously-treated monofilaments under constant tensile forces.* Carbon, 2013. **53**: p. 29-37.
8. Kling, S. and T. Czigany, *A comparative analysis of hollow and solid glass fibers.* Textile Research Journal, 2013. **83**(16): p. 1764-1772.
9. Toray Composite Materials America Inc. *T700S standard modulus carbon fiber*. 2020 [cited 2020 November 19]; Available from: https://www.toraycma.com/wp-content/uploads/T700S-Technical-Data-Sheet-1.pdf.pdf.

10. Gulgunje, P.V., B.A. Newcomb, K. Gupta, H.G. Chae, T.K. Tsotsis, and S. Kumar, *Low-density and high-modulus carbon fibers from polyacrylonitrile with honeycomb structure.* Carbon, 2015. **95**: p. 710-714.
11. Morris, E.A., R. Sarabia-Riquelme, N. Hochstrasser, J. Burgess, A.E. Oberlink, D.L. Eaton, and M.C. Weisenberger, *Early development of multifilament polyacrylonitrile-derived structural hollow carbon fibers from a segmented arc spinneret.* Carbon, 2021. **178**: p. 223-232.
12. Sauder, C., J. Lamon, and R. Pailler, *The tensile behavior of carbon fibers at high temperatures up to 2400 C.* Carbon, 2004. **42**(4): p. 715-725.
13. Jang, D., M.E. Lee, J. Choi, S.Y. Cho, and S. Lee, *Strategies for the production of PAN-Based carbon fibers with high tensile strength.* Carbon, 2021.
14. Lu, J., W. Li, H. Kang, L. Feng, J. Xu, and R. Liu, *Microstructure and properties of polyacrylonitrile based carbon fibers.* Polymer Testing, 2020. **81**: p. 106267.
15. Morgan, P., *Carbon fibers and their composites*. 2005, Boca Raton, LA: Taylor & Francis Group.
16. Shinmen, Y., N. Hirota, and T. Nii, Carbon-fiber-precursor fiber bundle, carbon fiber bundle, and uses thereof. U.S. Patent 10,233,569. March 19, 2019.
17. Chae, H.G., M.L. Minus, A. Rasheed, and S. Kumar, *Stabilization and carbonization of gel spun polyacrylonitrile/single wall carbon nanotube composite fibers.* Polymer, 2007. **48**(13): p. 3781-3789.
18. Moreton, R., W. Watt, and W. Johnson, *Carbon fibres of high strength and high breaking strain.* Nature, 1967. **213**(5077): p. 690-691.
19. Cooper, G.A. and R.M. Mayer, *The strength of carbon fibres.* Journal of Materials Science, 1971. **6**(1): p. 60-67.
20. Griffith, A.A., *The Phenomena of Rupture and Flow in Solids.* Philosophical Transactions of the Royal Society of London, Series A: Physical Sciences and Engineering, 1921. **221**: p. 163 - 198.
21. Rajalingam, P. and G. Radhakrishxan, *Polyacrylonitrile Precursor for Carbon Fibers.* Journal of Macromolecular Science, Part C: Polymer Reviews, 1991. **31**(2-3): p. 301-310.
22. Wang, M., Y. Xiao, W. Cao, N. Jiao, W. Chen, and L. Xu, *SAXS and WAXD study of periodical structure for polyacrylonitrile fiber during coagulation.* Polymers for Advanced Technologies, 2015. **26**(2): p. 136-141.
23. Gu, Y., M. Li, J. Wang, and Z. Zhang, *Characterization of the interphase in carbon fiber/polymer composites using a nanoscale dynamic mechanical imaging technique.* Carbon, 2010. **48**(11): p. 3229-3235.
24. Edrington, S., *The Limits & Effects of Draw on Properties and Morphology of Pan-Based Precursor and the Resultant Carbon Fibers.* 2017.
25. Balasubramanian, M., M.K. Jain, and A.S. Abhiraman, *Evolution of structure and properties in contrinuous carbon fiber formation*, in *Biennial Conference on Carbon*. 1985: England. p. 312-313.

CHAPTER 7. CONCLUSIONS AND FUTURE WORK

7.1 Conclusions

In this dissertation, the development of HCF from precursor spun from a segmented arc spinneret was explored. This comprehensive study delved into the rationale behind the approach, including a thorough review of the literature and the potential advantages provided by HCF over traditional solid CF. Multiple hypotheses were formed as a result, which served as a guide for the research. The bulk of the dissertation focused upon the development of the precursor, oxidized, and carbonized HF. Several key process-structure-property relationships were investigated and the results of this research are summarized here.

In the beginning of the dissertation, an overview of CF was given, highlighting their unique utility in lightweight, high strength and modulus composite structures. The high specific tensile properties of CF over other traditional materials is key. Further advances in specific properties would herald in new capabilities in lightweight structures. The HCF concept would allow for more efficient utilization of the oriented carbon by avoiding the development of the skin-core structure commonly seen in commercial CF. Previous investigations into the development of HCF for structural applications were found to be few in number. Of the limited studies conducted on the development of structural HCF, their approaches relied on complex spinneret geometries, sacrificial polymers, or other technologies that would be inherently difficult to scale to the thousands of filaments scale needed for commercial production. Thus entered the proposed segmented arc spinneret approach, an inherently scalable technology. Traditionally used for melt or dry spinning, segmented arc spinnerets had, to the author's knowledge, only been investigated by three authors for the air-gap solution spinning of PAN HF. Of those three authors, only one (a patent) described the formation of HCF from the segmented arc spinneret. Therefore, not only did the use of a segmented arc spinneret in solution spinning PAN warrant further research, but the development of structural HCF from such a technology represented a vastly unexplored research area with great potential for advancing the field of carbon fiber.

Several overarching hypotheses were formed to guide the research presented in this dissertation. First, **it was hypothesized that a segmented arc spinneret could be used to produce HF precursors with dimensions and morphology appropriate to the production of high tensile property HCF.** In studying the development of HF PAN precursors from a segmented arc spinneret, many conclusions related to this hypothesis were made. A primary, and important finding in support of the HCF concept, was the ability to spin multifilament, hollow PAN precursors from the segmented arc spinneret. The resulting HF precursors were relatively small in outer diameter, with concentric inner diameters, and round cross sections, representing some of the best hollow PAN precursors ever produced. They retained their hollow structure through the spinning and later thermal processing steps.

Another important related finding was that hollow fibers spun into a 100% water coagulation bath unfortunately contained a high number of macrovoids. Macrovoids were reduced by utilizing a lower molecular weight polymer (TechPAN2) which enabled a higher solids content in the spinning solution compared to the higher molecular weight TechPAN1 polymer. Fibers spun utilizing a 20 wt.% TechPAN2/DMSO spinning solution had significantly reduced macrovoid content, smaller wall thicknesses (suggesting a denser structure), and greater percent open area. Additionally, it was found that a characteristic time-scale in the air gap existed which would produce a minimum fiber wall thickness. By increasing the initial godet speed and dope flow rate to keep a constant draw ratio, fibers were collected after varying residence times in the air gap, and results indicated that the healing of the 2Cs to produce a minimum wall thickness occurred at 0.33 s, independent of air gap (where a 6.5 and 8 mm air gap were studied).

As well as containing a high number of macrovoids, fibers spun into a 100% water coagulation bath were found to contain a high amount of residual liquid, most likely composed of the spinning solvent and non-solvent, DMSO and water. Liquid was visible in the HF precursors when viewed under optical microscopy. The amount of residual liquid within the fiber was found to decrease when the DMSO concentration in the coagulation bath increased, from a 100% water bath (0% DMSO/water) up to a 30 wt.% DMSO/water bath. It is hypothesized that further increases in coagulation bath solvent content would

decrease the amount of residual liquid in the fiber, but this has yet to be studied. Additionally, the removal of residual liquid from the fiber via water washing was not possible under washing times typical to fiber spinning (minutes), and residual liquid was only found to be removed when fiber was chopped into small ~ 1 mm lengths. This result suggested that the exchange of liquid was hindered by a rapidly formed cuticle on the HF spun into 100% water.

Finally, with regard to HF precursor development, it was found that both effective tensile strength and effective elastic modulus increased as a function of decreasing fiber outer diameter. The effective tensile properties trended toward those of a traditional solid precursor fiber, suggesting that with further reduction in precursor outer diameters, it is possible to meet or exceed the tensile properties of a corresponding solid fiber. This would be amplified when comparing fibers on a *specific* tensile property basis. Overall, the findings presented in this dissertation, including the formation of multifilament HF precursors with effective tensile properties approaching those of traditional solid precursors, support the hypothesis that a segmented arc spinneret could be used to produce HF precursors with dimensions and morphology appropriate to the production of high tensile property HCF.

As the study moved beyond HF precursor development and into oxidation studies, **it was hypothesized that with reduced wall thickness, one could arrive at an optimally oxidized fiber faster than traditional solid fiber via simultaneous oxidation from the exterior and interior of the HF.** In evaluating the oxidized HF, it was found that HF precursors were able to oxidize from the interior and exterior. The interior oxidized skin thickness of the oxidized HF increased with the fiber's percent open area (or lumen area). Results indicated that the ability to oxidize from the interior was limited to the amount of air (oxygen) contained within the lumen at the start of the oxidation process. The outer skin layer was found to consistently measure ~ 4 μm in thickness, while a percent open area of ~ 50 % or more was found to achieve a similar 4 μm interior oxidized skin thickness. It was hypothesized that the oxidation of a HF with a ≤ 8 μm wall thickness would produce a homogeneous (non-skin-core) cross section.

EDX analysis of an oxidized HF fiber cross section was completed and revealed both the interior and exterior oxidized skin of the fiber to contain a higher concentration of oxygen compared to the core. Interesting behavior was observed around the macrovoid present in the oxidized HF subjected to EDX in that the skin of the fiber followed the perimeter of the macrovoid. This suggested that the macrovoid contained air (oxygen) which allowed oxidation to proceed about the macrovoid. Complementing the EDX analysis, spatially mapped I_D/I_G ratios in the Raman analysis of the oxidized HF cross section revealed the skin was more highly ordered and contained more sp^2 hybridized carbon than the core structure. The skin persisted about the perimeter of fused filaments where direct air access occurred. Raman results were found to overlay with the optical image of the same fiber nearly perfectly. In all, the Raman data appeared to confirm the role of oxygen in the formation of polycyclic aromatic structures.

Finally, density analyses of HF precursors with similar OD and varying percent open area were compared to that of a similar OD solid fiber. It was found that the HF with 55% open area densified at a rate 12.7% faster compared to the baseline solid fiber during oxidation processing. This increase in densification rate was attributed to the ability of the HF to oxidize from both the interior and exterior simultaneously. In addition, the HF densification rate was likely an underestimation given the entrainment of air in the porous baseline solid fiber which is hypothesized to have accelerated its densification rate. These results supported the hypothesis that with reduced wall thickness, here achieved by holding OD constant and increasing percent open area, one could arrive at an optimally oxidized fiber faster than traditional solid fiber via simultaneous oxidation from the exterior and interior of the HF. This represented a significant finding and suggested that with reduced wall thickness (shorter diffusion lengths), this could significantly reduce the time necessary for fiber oxidation – a current bottleneck in CF manufacture.

The final sections of the dissertation focused on the development of HCF. An initial significant finding was that carbonization of oxidized HF resulted in HCF with small diameter, round cross section, and concentric wall thickness. No fiber collapse was observed. Effective densities for the resulting HCF were on the order of 1.1 g/cc, compared to 1.8 g/cc for traditional solid CF, nearly a 40% reduction. There were two primary

hypotheses guiding the HCF study, the first of which **hypothesized that the true elastic modulus of the HCF would increase as a function of increasing percent open area (for a fixed outer diameter) due to the reduction in skin-core structure in the HCF.** It was found that the spinning process had not yet matured to the point that it was possible to spin a HF with a targeted OD, much less a targeted OD *and* targeted percent open area. As a result, the next best option was to evaluate fibers with similar wall thicknesses and varying percent open area. It was shown earlier in the dissertation that skin-core structure was reduced with increasing percent open area. However, measurement of the true elastic modulus was complicated by differences in the draw ratios used to produce the HF precursors of varying dimensions. The draw the fiber experiences during spinning and thermal processing is highly impactful on the alignment of the molecular and crystalline structures, resulting in changes to elastic modulus in the precursor and resulting CF. Therefore, it was concluded that an optimal experimental design to test the hypothesis would require spinning HF precursors utilizing the same draw ratios, with the same targeted OD and varying percent open areas. It should be noted that separating fiber draw from final fiber dimensions is not trivial, as the two are largely interdependent. Increasing fiber draw leads to reduced fiber dimensions (diameters and/or percent open area) and vice versa. It is likely that multiple spinnerets with varying percent open area would need to be designed and machined and then extensive experimentation and process control developed to achieve HF precursors with same draw ratios, the same targeted OD and varying percent open areas. Evaluation of this hypothesis will become more possible as the spinning process continues to develop.

While it was difficult to determine the effect of reduced skin-core structure on true elastic modulus of the HCF, comparison of the HCF with solid CF was completed. **It was hypothesized that the resulting effective tensile strength of the HCF could conserve the tensile strength of a similar OD solid CF.** To accurately compare the tensile performance of HCF with solid CF, a solid precursor fiber was spun with the same diameter as that of the HF precursor (~ 80 μm). After oxidation, the HF possessed a much smaller ratio of skin to core structure compared to the solid fiber. Following carbonization, the tensile properties of the HCF were vastly superior to those of the solid CF. The effective tensile strength, effective elastic modulus, and break strain of the HCF were 8x, 2x, and 4x

higher, respectively, than the solid CF. Further examination of the solid CF cross-sections revealed a significant increase in macrovoid size and concentration over those of the precursor. When observing the solid CF surfaces, large portions of material were missing from the fibers. It was hypothesized that the large, likely highly under-oxidized, core of the solid fiber excessively vaporized during carbonization, resulting in significant damage to the solid CF surfaces and internal structure which significantly reduced the tensile properties. In this case, the HF demonstrated significant advantages over the solid fiber, primarily due to its ability to oxidize from both the interior and exterior. This result supported the hypothesis that HCF could conserve (and in this case, exceed) the tensile strength of a similar OD solid CF.

In conclusion, this dissertation has presented findings new to the field of carbon fiber. Multifilament PAN HF precursors were solution spun from a segmented arc spinneret. Fibers were round with concentric inner diameters. The effective tensile properties trended toward those of a traditional solid precursor fiber, suggesting that with further reduction in precursor outer diameters, it is possible to meet or exceed the tensile properties of a corresponding solid fiber. Oxidation of the HF precursors revealed their ability to oxidize from the interior and exterior. This increased oxidation ability allowed the HF to densify faster than a similar OD solid fiber. The data collected also supported the hypothesis that a ≥ 50 % open area HF with a ≤ 8 μm wall thickness would lead to an oxidized HF with a homogeneous (non-skin-core) morphology. Finally, a comparison of the HCF with a solid CF of the same outer diameter revealed the effective tensile strength, effective elastic modulus, and break strain of the HCF were 8x, 2x, and 4x higher, respectively, than the solid CF. In addition, the effective density of the HCF was 40% less than that of the solid CF. As a result, the specific effective properties of the HCF vastly outperformed those of the solid CF with the same outer diameter. In all, the hollow fibers produced in this study show great promise toward the improvement of carbon fiber specific tensile properties, and with further development could represent a new technological advancement in the carbon fiber field.

7.2 Future work

A central challenge to HCF progress is the reduction of fiber dimensions. As described previously, reduction in HF precursor OD and wall thickness are hypothesized to permit fast, homogeneous oxidation of the HF wall and to improve the effective tensile properties of the resulting HCF. While there may be room to further increase fiber draw to reduce dimensions, significant reductions are likely to come from the use of a 2C spinneret with reduced capillary dimensions (within machinable limits). Design and machining of spinnerets with reduced 2C dimensions is not trivial and may require several iterations.

Secondary to a reduction in fiber dimensions is the exploration of coagulation baths containing > 30 wt.% DMSO/water. It is hypothesized that increasing the solvent content in the coagulation bath toward a typical 70-80 wt.% DMSO/water concentration will reduce macrovoid formation and residual liquid content, which as a result, will improve tensile properties of the resulting HCF. Exploration of this hypothesis is more straightforward than the aforementioned dimension reduction as it can be performed utilizing existing spinnerets and requires only changing of the coagulation bath concentration. However, ensuring the formation of hollow filaments without collapse at high solvent bath concentrations may become more challenging as solvent contents increase.

Last but not least, the HF precursor, oxidation, and carbonization processes all require further investigation and optimization. The work performed in this study could serve a basis for further exploration. For example, the oxidation and carbonization processes have only been performed on a static basis, without optimization of the time-temperature-strain pathways. Significant advancements in flaw and defect mitigation and reduction must be undertaken to improve the HCF tensile properties. These are just a few examples of many, many experiments that may be undertaken to optimize the HCF concept.

In conclusion, this dissertation opens the door on the spinning, oxidation, and carbonization of multifilament PAN hollow fibers derived from a segmented arc spinneret. This work has sought to answer several fundamental questions regarding the ability of HCF to advance the field of CF and, in the process, has uncovered new questions primed for

exploration. As Helen Keller once wrote, “A well-educated mind will always have more questions than answers”.

APPENDIX

Table A - 1. Effective tensile strength, elastic modulus, and density for the HCF samples derived from 497A, B, C, and D, compared to literature values for large diameter CF from Chae et al., Mitsubishi, and standard diameter T700S CF.

Carbon Fiber	Effective Tensile Strength (MPa)	Effective Elastic Modulus (GPa)	Effective Density (g/cc)
497A HCF	233 ± 77	37 ± 4	0.8
497B HCF	422 ± 70	61 ± 9	1
497C HCF	568 ± 214	135 ± 20	1.1
497D HCF	594 ± 248	132 ± 21	1.1
Chae et al.	1980	265	1.8
Mitsubishi	3600	232	1.8
T700S	4900	245	1.8

BIBLIOGRAPHY

Arbab, S. and A. Zeinolebadi, A procedure for precise determination of thermal stabilization reactions in carbon fiber precursors. Polymer Degradation and Stability, 2013. 98(12): p. 2537-2545.

Bailey, J. and A. Clarke, Carbon fibre formation—the oxidation treatment. Nature, 1971. 234(5331): p. 529-531.

Balasubramanian, M., M.K. Jain, and A.S. Abhiraman, Evolution of structure and properties in contrinuous carbon fiber formation, in Biennial Conference on Carbon. 1985: England. p. 312-313.

Barnet, F.R. and M.K. Norr, A three-dimensional structural model for a high modulus pan-based carbon fibre. Composites, 1976. 7(2): p. 93-99.

Bennett, S.C., D.J. Johnson, and W. Johnson, Strength-structure relationships in PAN-based carbon fibres. Journal of Materials Science, 1983. 18(11): p. 3337-3347.

Bhat, G., Structure and properties of high-performance fibers. 2016: Woodhead Publishing.

Blanco, C., S. Lu, S. Appleyard, and B. Rand, The stabilisation of carbon fibres studied by micro-thermal analysis. Carbon, 2003. 41(1): p. 165-171.

Chae, H.G., M.L. Minus, A. Rasheed, and S. Kumar, Stabilization and carbonization of gel spun polyacrylonitrile/single wall carbon nanotube composite fibers. Polymer, 2007. 48(13): p. 3781-3789.

Chen, L., L. Hao, S. Liu, G. Ding, X. Sun, W. Zhang, F. Li, W. Jiao, F. Yang, Z. Xu, R. Wang, and X. He, Modulus distribution in polyacrylonitrile-based carbon fiber monofilaments. Carbon, 2020. 157: p. 47-54.

Choi, J., S.-S. Kim, Y.-S. Chung, and S. Lee, Evolution of structural inhomogeneity in polyacrylonitrile fibers by oxidative stabilization. Carbon, 2020.

Choi, Y.H., S. Han, and C.H. Choi, Preparation method for hollow carbon fiber. U.S. Patent 9,109,305. August 18, 2015.

Chuah, H.H. and B.T.A. Chang, Crystal orientation function of poly(trimethylene terephthalate) by wide-angle x-ray diffraction. Polymer Bulletin, 2001. 46(4): p. 307-313.

Clarke, A. and J. Bailey, Oxidation of acrylic fibres for carbon fibre formation. Nature, 1973. 243(5403): p. 146.

Colvin, B.G. and P. Storr, The crystal structure of polyacrylonitrile. European Polymer Journal, 1974. 10(4): p. 337-340.

Confidential carbon fiber consultant, Personal Communication. 2021.

Cooper, G.A. and R.M. Mayer, The strength of carbon fibres. Journal of Materials Science, 1971. 6(1): p. 60-67.

Craig, J.P., J.P. Knudsen, and V.F. Holland, Characterization of acrylic fiber structure. Textile Research Journal, 1962. 32(6): p. 435-448.

Damodaran, S., P. Desai, and A.S. Abhiraman, Chemical and physical aspects of the formation of carbon fibres from PAN-based precursors. The Journal of The Textile Institute, 2008. 81(4): p. 384-420.

Das, S., J. Warren, D. West, and S.M. Schexnayder, Global carbon fiber composites supply chain competitiveness analysis. 2016, Oak Ridge National Laboratory; The University of Tennessee, Knoxville.

De Rovere, A., B.P. Grady, and R.L. Shambaugh, The influence of processing parameters on the properties of melt-spun polypropylene hollow fibers. Journal of Applied Polymer Science, 2002. 83(8): p. 1759-1772.

Devasia, R., C.P.R. Nair, P. Sivadasan, B.K. Katherine, and K.N. Ninan, Cyclization reaction in poly(acrylonitrile/itaconic acid) copolymer: An isothermal differential scanning calorimetry kinetic study. Journal of Applied Polymer Science, 2003. 88(4): p. 915-920.

Edrington, S., The Limits & Effects of Draw on Properties and Morphology of Pan-Based Precursor and the Resultant Carbon Fibers. 2017.

Ferguson, J., Apparatus and method for spinning hollow polymeric fibres. U.S. Patent 6,143,411. November 7, 2000.

Fitzer, E. and W. Metzler, Hollow carbon fibres. 1990.

Frank, E., L.M. Steudle, D. Ingildeev, J.M. Spörl, and M.R. Buchmeiser, Carbon fibers: precursor systems, processing, structure, and properties. Angewandte Chemie International Edition, 2014. 53(21): p. 5262-5298.

Friedlander, H.N., L.H. Peebles, J. Brandrup, and J.R. Kirby, On the Chromophore of Polyacrylonitrile. VI. Mechanism of Color Formation in Polyacrylonitrile. Macromolecules, 1968. 1(1): p. 79-86.

Gandhi, S. and R.E. Lyon, Health hazards of combustion products from aircraft composite materials. 1998, Federal Aviation Administration Technical Center: Atlantic City, NJ. p. 1-29.

Ge, Y., Z. Fu, Y. Deng, M. Zhang, and H. Zhang, The effects of chemical reaction on the microstructure and mechanical properties of polyacrylonitrile (PAN) precursor fibers. Journal of Materials Science, 2019. 54(19): p. 12592-12604.

Griffith, A.A., The Phenomena of Rupture and Flow in Solids. Philosophical Transactions of the Royal Society of London, Series A: Physical Sciences and Engineering, 1921. 221: p. 163 - 198.

Grobe, V. and K. Meyer, Faserforschung und Textiltechnik, 1959. 10: p. 214-224.

Grove, D., P. Desai, and A.S. Abhiraman, Exploratory experiements in the conversion of plasticized melt spun PAN-based precursors to carbon fibers. Carbon, 1988. 26(3): p. 403 - 411.

Gu, Y., M. Li, J. Wang, and Z. Zhang, Characterization of the interphase in carbon fiber/polymer composites using a nanoscale dynamic mechanical imaging technique. Carbon, 2010. 48(11): p. 3229-3235.

Gulgunje, P.V., B.A. Newcomb, K. Gupta, H.G. Chae, T.K. Tsotsis, and S. Kumar, Low-density and high-modulus carbon fibers from polyacrylonitrile with honeycomb structure. Carbon, 2015. 95: p. 710-714.

Guo, X., Y. Cheng, Z. Fan, Z. Feng, L. He, R. Liu, and J. Xu, New insights into orientation distribution of high strength polyacrylonitrile-based carbon fibers with skin-core structure. Carbon, 2016. 109: p. 444-452.

Gupta, A. and I. Harrison, New aspects in the oxidative stabilization of PAN-based carbon fibers. Carbon, 1996. 34(11): p. 1427-1445.

Gupta, A.K., D.K. Paliwal, and P. Bajaj, Acrylic Precursors for Carbon Fibers. Polymer Reviews, 1991. 31(1): p. 1-89.

Hao, J.H., H. Dai, P. Yang, and Z. Wang, Spinning of cellulose acetate hollow fiber by dry-wet technique of 3C-shaped spinneret. Journal of Applied Polymer Science, 1996. 62(1): p. 129-133.

Hoffman, W., W. Hurley, P. Liu, and T. Owens, The surface topography of non-shear treated pitch and PAN carbon fibers as viewed by the STM. Journal of materials research, 1991. 6(8): p. 1685-1694.

Houtz, R., "Orlon" Acrylic Fiber: Chemistry and Properties. Textile Research Journal, 1950. 20(11): p. 786-801.

Huang, Y. and R.J. Young, Effect of Fibre Microstructure Upon the Modulus of PAN- and Pitch-Based Carbon Fibres. Carbon, 1995. 33(2): p. 91-107.

Jagtoyen, M., F. Derbyshire, S. Rimmer, and R. Rathbone, Relationship between reflectance and structure of high surface area carbons. Fuel, 1995. 74(4): p. 610-614.

Jain, M.K. and A.S. Abhiraman, Conversion of acrylonitrile-based precursor fibres to carbon fibres. Journal of Materials Science, 1987. 22(1): p. 278-300.

Jang, D., M.E. Lee, J. Choi, S.Y. Cho, and S. Lee, Strategies for the production of PAN-Based carbon fibers with high tensile strength. Carbon, 2021.

Johnson, D. and C. Tyson, The fine structure of graphitized fibres. Journal of Physics D: Applied Physics, 1969. 2(6): p. 787.

Johnson, J.W. and D.J. Thorne, Effect of internal polymer flaws on strength of carbon fibres prepared from an acrylic precursor. Carbon, 1969. 7(6): p. 659-661.

Jones, W. and J. Johnson, Intrinsic strength and non-Hookean behaviour of carbon fibres. Carbon, 1971. 9(5): p. 645-655.

Ju, A., S. Hou, Y. Pan, Y. Wang, Y. Zhu, and H. Chen, Preparation of hollow carbon submicro-fibers with controllable wall thicknesses from acrylonitrile copolymer. Textile Research Journal, 2017. 88(16): p. 1893-1901.

Karacan, I. and G. Erdoğan, A study on structural characterization of thermal stabilization stage of polyacrylonitrile fibers prior to carbonization. Fibers and Polymers, 2012. 13(3): p. 329-338.

Kaur, J., K. Millington, and S. Smith, Producing high-quality precursor polymer and fibers to achieve theoretical strength in carbon fibers: A review. Journal of Applied Polymer Science, 2016. 133(38).

Kikuma, J., T. Konishi, and T. Sekine, Polymer analysis by Auger electron spectroscopy using sectioning and cryogenic cooling. Journal of electron spectroscopy and related phenomena, 1994. 69(2): p. 141-147.

Kikuma, J., T. Warwick, H.-J. Shin, J. Zhang, and B.P. Tonner, Chemical state analysis of heat-treated polyacrylonitrile fiber using soft X-ray spectromicroscopy. Journal of electron spectroscopy and related phenomena, 1998. 94(3): p. 271-278.

Kim, P., L. Shi, A. Majumdar, and P.L. McEuen, Thermal transport measurements of individual multiwalled nanotubes. Phys Rev Lett, 2001. 87(21): p. 215502.

Kling, S. and T. Czigany, A comparative analysis of hollow and solid glass fibers. Textile Research Journal, 2013. 83(16): p. 1764-1772.

Knudsen, J.P., The influence of coagulation variables on the structure and physical properties of an acrylic fiber. Textile Research Journal, 1963. 33: p. 13.

Kobayashi, T., K. Sumiya, Y. Fujii, M. Fujie, T. Takahagi, and K. Tashiro, Stress concentration in carbon fiber revealed by the quantitative analysis of X-ray crystallite modulus and Raman peak shift evaluated for the variously-treated monofilaments under constant tensile forces. Carbon, 2013. 53: p. 29-37.

Kong, L., H. Liu, W. Cao, and L. Xu, PAN fiber diameter effect on the structure of PAN-based carbon fibers. Fibers and Polymers, 2015. 15(12): p. 2480-2488.

Kumar, S., D.P. Anderson, and A.S. Crasto, Carbon fibre compressive strength and its dependence on structure and morphology. Journal of Materials Science, 1993. 28(2): p. 423-439.

Law, S.J. and S.K. Mukhopadhyay, Investigation of Wet-Spun Acrylic Fiber Morphology by Membrane Technology Techniques. Journal of Applied Polymer Science, 1996. 62: p. 32-47.

Layden, G., Retrograde core formation during oxidation of polyacrylonitrile filaments. Carbon, 1972. 10(1): p. 59-63.

Lee, J.H., J.-U. Jin, S. Park, D. Choi, N.-H. You, Y. Chung, B.-C. Ku, and H. Yeo, Melt processable polyacrylonitrile copolymer precursors for carbon fibers: Rheological, thermal, and mechanical properties. Journal of Industrial and Engineering Chemistry, 2019. 71: p. 112-118.

Lee, M.S., T.H. Oh, S.Y. Kim, and H.J. Shim, Deformation kinetics of polypropylene hollow fibers in a continuous drawing process. Journal of Applied Polymer Science, 1999. 74(7): p. 1836-1845.

Liu, F., H. Wang, L. Xue, L. Fan, and Z. Zhu, Effect of microstructure on the mechanical properties of PAN-based carbon fibers during high-temperature graphitization. Journal of Materials Science, 2008. 43(12): p. 4316-4322.

Liu, J., Z. Yue, and H. Fong, Continuous nanoscale carbon fibers with superior mechanical strength. Small, 2009. 5(5): p. 536-42.

Liu, S., K. Han, L. Chen, Y. Zheng, and M. Yu, Structure and properties of partially cyclized polyacrylonitrile-based carbon fiber-precursor fiber prepared by melt-spun with ionic liquid as the medium of processing. Polymer Engineering & Science, 2015. 55(12): p. 2722-2728.

Liu, X., C. Zhu, J. Guo, Q. Liu, H. Dong, Y. Gu, R. Liu, N. Zhao, Z. Zhang, and J. Xu, Nanoscale dynamic mechanical imaging of the skin–core difference: From PAN precursors to carbon fibers. Materials Letters, 2014. 128: p. 417-420.

Liu, Y., H.G. Chae, Y.H. Choi, and S. Kumar, Preparation of low density hollow carbon fibers by bi-component gel-spinning method. Journal of Materials Science, 2015. 50(10): p. 3614-3621.

Loidl, D., O. Paris, H. Rennhofer, M. Müller, and H. Peterlik, Skin-core structure and bimodal Weibull distribution of the strength of carbon fibers. Carbon, 2007. 45(14): p. 2801-2805.

Longming, W., Y. Yang, and X. Lianghua, Formation mechanism of PAN hollow fiber prepared by wet spinning process. China Synthetic Fiber Industry, 2012. 35(1): p. 26-30.

Lu, J., W. Li, H. Kang, L. Feng, J. Xu, and R. Liu, Microstructure and properties of polyacrylonitrile based carbon fibers. Polymer Testing, 2020. 81: p. 106267.

Lv, M.-Y., H.-Y. Ge, and J. Chen, Study on the chemical structure and skin-core structure of polyacrylonitrile-based fibers during stabilization. Journal of Polymer Research, 2008. 16(5): p. 513-517.

Mahmood, S.F., B.L. Batchelor, M. Jung, K. Park, W.E. Voit, B.M. Novak, and D. Yang, Study of a melt processable polymer precursor for carbon fiber. Carbon Letters, 2019. 29(6): p. 605-612.

Masson, J., Acrylic fiber technology and applications. 1995: CRC Press.

Mikolajczyk, T., S. Rabiej, G. Szparaga, M. Boguń, A. Fraczek-Szczypta, and S. Błażewicz, Strength properties of polyacrylonitrile (PAN) fibres modified with carbon nanotubes with respect to their porous and supramolecular structure. Fibres & Textiles in Eastern Europe, 2009. 17(6): p. 13-20.

Minus, M. and S. Kumar, The processing, properties, and structure of carbon fibers. Jom, 2005. 57(2): p. 52-58.

Moreton, R., W. Watt, and W. Johnson, Carbon fibres of high strength and high breaking strain. Nature, 1967. 213(5077): p. 690-691.

Morgan, P., Carbon fibers and their composites. 2005, Boca Raton, LA: Taylor & Francis Group.

Morita, K., Y. Murata, A. Ishitani, K. Murayama, T. Ono, and A. Nakajima, Characterization of commercially available PAN (polyacrylonitri1e)-based carbon fibers. Pure and Applied Chemistry, 1986. 58(3): p. 455-468.

Morris, E.A., R. Sarabia-Riquelme, N. Hochstrasser, J. Burgess, A.E. Oberlink, D.L. Eaton, and M.C. Weisenberger, Early development of multifilament polyacrylonitrile-

derived structural hollow carbon fibers from a segmented arc spinneret. Carbon, 2021. 178: p. 223-232.

Morris, E.A. and M.C. Weisenberger, Solution Spinning of PAN-Based Polymers for Carbon Fiber Precursors, in Polymer Precursor-Derived Carbon, A.K. Naskar and W.P. Hoffman, Editors. 2014, ACS Books. p. 189-213.

Morris, E.A., M.C. Weisenberger, M.G. Abdallah, F. Vautard, H. Grappe, S. Ozcan, F.L. Paulauskas, C. Eberle, D. Jackson, S.J. Mecham, and A.K. Naskar, High performance carbon fibers from very high molecular weight polyacrylonitrile precursors. Carbon, 2016. 101: p. 245-252.

Morris, E.A., M.C. Weisenberger, and G.W. Rice, Properties of PAN fibers solution spun into a chilled coagulation bath at high solvent compositions. Fibers, 2015. 3(4): p. 560-574.

Noland, R.L. and T.D. O'Brien, Hollow carbon fibers. U.S. Patent 5,338,605. August 16, 1994.

Nunna, S., C. Creighton, B.L. Fox, M. Naebe, M. Maghe, M.J. Tobin, K. Bambery, J. Vongsvivut, and N. Hameed, The effect of thermally induced chemical transformations on the structure and properties of carbon fibre precursors. Journal of materials chemistry A, 2017. 5(16): p. 7372-7382.

Nunna, S., C. Creighton, N. Hameed, M. Naebe, L.C. Henderson, M. Setty, and B.L. Fox, Radial structure and property relationship in the thermal stabilization of PAN precursor fibres. Polymer Testing, 2017. 59: p. 203-211.

Nunna, S., M. Setty, and M. Naebe, Formation of skin-core in carbon fibre processing: A defect or an effect? Express Polymer Letters, 2019. 13(2): p. 146-158.

Ogawa, H. and K. Saito, Oxidation behavior of polyacrylonitrile fibers evaluated by new stabilization index. Carbon, 1995. 33(6): p. 783-788.

Ouyang, Q., L. Cheng, H. Wang, and K. Li, Mechanism and kinetics of the stabilization reactions of itaconic acid-modified polyacrylonitrile. Polymer Degradation and Stability, 2008. 93(8): p. 1415-1421.

Pandey, G.C. and A. Kumar, Determination of density of oxidized fiber by IR spectroscopy. Polymer testing, 2002. 21(4): p. 397-401.

Rahaman, M.S.A., A.F. Ismail, and A. Mustafa, A review of heat treatment on polyacrylonitrile fiber. Polymer Degradation and Stability, 2007. 92(8): p. 1421-1432.

Rajalingam, P. and G. Radhakrishxan, Polyacrylonitrile Precursor for Carbon Fibers. Journal of Macromolecular Science, Part C: Polymer Reviews, 1991. 31(2-3): p. 301-310.

Reynolds, W.N. and J.V. Sharp, Crystal shear limit to carbon fibre strength. Carbon, 1974. 12(2): p. 103-110.

Rizzo, P., F. Auriemma, G. Guerra, V. Petraccone, and P. Corradini, Conformational disorder in the pseudohexagonal form of atactic polyacrylonitrile. Macromolecules, 1996. 29(27): p. 8852-8861.

Rwei, S.-P., Formation of hollow fibers in the melt-spinning process. Journal of Applied Polymer Science, 2001. 82(12): p. 2896-2902.

Sauder, C., J. Lamon, and R. Pailler, Thermomechanical properties of carbon fibres at high temperatures (up to 2000 C). Composites Science and Technology, 2002. 62(4): p. 499-504.

Sauder, C., J. Lamon, and R. Pailler, The tensile behavior of carbon fibers at high temperatures up to 2400 C. Carbon, 2004. 42(4): p. 715-725.

Sha, Y., W. Liu, Y. Li, and W. Cao, Formation Mechanism of Skin-Core Chemical Structure within Stabilized Polyacrylonitrile Monofilaments. Nanoscale Res Lett, 2019. 14(1): p. 93.

Shim, H.B., J.I. Lee, H.S. Kim, Y.J. Choe, and B.S. Rhee. On hollow and C-type carbon fiber reinforced composite materials. in International Conference on Advanced Composite Materials (ICACM). 1993.

Shinmen, Y., N. Hirota, and T. Nii, Carbon-fiber-precursor fiber bundle, carbon fiber bundle, and uses thereof. U.S. Patent 10,233,569. March 19, 2019.

Sivek, J. Creative commons carbon allotropes. 2015 [cited 2021; CC BY-SA 4.0]. Available from: https://commons.wikimedia.org/wiki/File:Carbon_allotropes.svg.

Standage, A.E. and R. Prescott, High Elastic Modulus Carbon Fibre. Nature, 1966. 211(5045): p. 169-169.

Stoyanov, A., Influence of the content of polymer with different molecular weights in spinning solutions on properties of acrylic fibers. Journal of Applied Polymer Science, 1982. 27(1): p. 235-238.

Subbiah, T., G.S. Bhat, R.W. Tock, S. Parameswaran, and S.S. Ramkumar, Electrospinning of nanofibers. Journal of Applied Polymer Science, 2005. 96(2): p. 557-569.

Sui, X., Z. Xu, C. Hu, L. Chen, L. Liu, L. Kuang, M. Ma, L. Zhao, J. Li, and H. Deng, Microstructure evolution in γ-irradiated carbon fibers revealed by a hierarchical model and

Raman spectra from fiber section. Composites Science and Technology, 2016. 130: p. 46-52.

Sun, L., M. Li, L. Shang, L. Xiao, Y. Liu, M. Zhang, and Y. Ao, The influence of oxygen on skin-core structure of polyacrylonitrile-based precursor fibers. Polymer, 2020: p. 122516.

Sun, T., Y. Hou, and H. Wang, Effect of atmospheres on stabilization of polyacrylonitrile fibers. Journal of Macromolecular Science, Part A, 2009. 46(8): p. 807-815.

Sun, T., Y. Hou, and H. Wang, Mass DSC/TG and IR ascertained structure and color change of polyacrylonitrile fibers in air/nitrogen during thermal stabilization. Journal of Applied Polymer Science, 2010. 118(1): p. 462-468.

Takahashi, M., Y. Nukushina, and S. Kosugi, Effect of fiber-forming conditions on the microstructure of acrylic fiber. Textile research journal, 1964. 34(2): p. 87-97.

Takaku, A., T. Hashimoto, and T. Miyoshi, Tensile properties of carbon fibers from acrylic fibers stabilized under isothermal conditions. Journal of Applied Polymer Science, 1985. 30(4): p. 1565-1571.

Thewlis, R., The spinning of hollow polyacrylonitrile fibres as a precursor for the formation of hollow carbon fibres. 1998, University of Strathclyde.

Thorne, D. and J. Marjoram, Optical properties and orientation of thermally treated acrylic fibers. Journal of Applied Polymer Science, 1972. 16(6): p. 1357-1366.

Toray Composite Materials America Inc. *T700S standard modulus carbon fiber*. 2020 [cited 2020 November 19]; Available from: https://www.toraycma.com/wp-content/uploads/T700S-Technical-Data-Sheet-1.pdf.pdf.

Tsai, J.-S. and W.-C. Su, Control of cross-section shape for polyacrylonitrile fibre during wet-spinning. Journal of Materials Science Letters, 1991. 10(21): p. 1253-1256.

Turner, W. and F. Johnson, The pyrolysis of acrylic fiber in inert atmosphere. I. Reactions up to 400° C. Journal of Applied Polymer Science, 1969. 13(10): p. 2073-2084.

Wang, C.Y., M.W. Li, Y.L. Wu, and C.T. Guo, Preparation and microstructure of hollow mesophase pitch-based carbon fibers. Carbon, 1998. 36(12): p. 1749-1754.

Wang, M., Y. Xiao, W. Cao, N. Jiao, W. Chen, and L. Xu, SAXS and WAXD study of periodical structure for polyacrylonitrile fiber during coagulation. Polymers for Advanced Technologies, 2015. 26(2): p. 136-141.

Wang, P., Aspects on prestretching of PAN precursor: Shrinkage and thermal behavior. Journal of applied polymer science, 1998. 67(7): p. 1185-1190.

Warner, S.B., L.H. Peebles, and D.R. Uhlmann, Oxidative stabilization of acrylic fibres. Journal of Materials Science, 1979. 14(3): p. 556-564.

Watt, W., Pyrolysis of polyacrylonitrile. Nature, 1969. 222(5190): p. 265-266.

Watt, W. and W. Johnson, Mechanism of oxidisation of polyacrylonitrile fibres. Nature, 1975. 257(5523): p. 210-212.

Wei, H.Q., X.D. Suo, C.X. Lu, and Y.D. Liu, A comparison of coagulation and gelation on the structures and stabilization behaviors of polyacrylonitrile fibers. Journal of Applied Polymer Science, 2020. 137(19): p. 48671.

Weisenberger, M. and A. Morris. Precursor processing development for low cost, high strength carbon fiber for composite overwrapped pressure vessel applications. US Department of Energy 2018; Available from: https://www.hydrogen.energy.gov/pdfs/review18/st146_weisenberger_2018_p.pdf.

Xiao, S., B. Wang, C. Zhao, L. Xu, and B. Chen, Influence of oxygen on the stabilization reaction of polyacrylonitrile fibers. Journal of applied polymer science, 2013. 127(3): p. 2332-2338.

Xue, Y., J. Liu, F. Lian, and J. Liang, Effect of the oxygen-induced modification of polyacrylonitrile fibers during thermal-oxidative stabilization on the radial microcrystalline structure of the resulting carbon fibers. Polymer Degradation and Stability, 2013. 98(11): p. 2259-2267.

Yang, F., W. Liu, M. Yi, L. Ran, Y. Ge, and K. Peng, Effect of high temperature treatment on the microstructure and elastoplastic properties of polyacrylonitrile-based carbon fibers. Carbon, 2020. 158: p. 783-794.

Yu, M.-J., C.-G. Wang, Y.-J. Bai, M.-X. Ji, and Y. Xu, SEM and OM study on the microstructure of oxidative stabilized polyacrylonitrile fibers. Polymer Bulletin, 2007. 58(5-6): p. 933-940.

Yu, M.-J., C.-G. Wang, Y.-J. Bai, Y. Xu, and B. Zhu, Effect of oxygen uptake and aromatization on the skin–core morphology during the oxidative stabilization of polyacrylonitrile fibers. Journal of Applied Polymer Science, 2008. 107(3): p. 1939-1945.

Zhang, X., Y. Wen, Y. Yang, and L. Liu, Effect of air-gap distance on the formation and characterization of hollow polyacrylonitrile (PAN) nascent fibers. Journal of Macromolecular Science, Part B, 2008. 47(6): p. 1039-1049.

Zussman, E., X. Chen, W. Ding, L. Calabri, D.A. Dikin, J.P. Quintana, and R.S. Ruoff, Mechanical and structural characterization of electrospun PAN-derived carbon nanofibers. Carbon, 2005. 43(10): p. 2175-2185.

VITA
Elizabeth Ashley Morris

EDUCATION

M.Sc., Mechanical Engineering, University of Kentucky, Lexington, Kentucky, 2011.
Thesis: "*Bench-Scale, Multifilament Spinning Conditions Effect on the Structure and Properties of Polyacrylonitrile Precursor Fiber*", Advisor: Dr. Rodney Andrews.

B.Sc., Mechanical Engineering, University of Kentucky, Lexington, Kentucky, 2009.

SCHOLASTIC HONORS

University of Kentucky Presidential Scholarship (four years full tuition) awarded in 2004
University of Kentucky Graduate Research Assistantship (full tuition plus stipend) from 2009-2011

PROFFESSIONAL POSITIONS

2019-present Secretary-Treasurer, American Carbon Society

2016-present Principal Research Engineer, Center for Applied Energy Research, University of Kentucky

2015-2015 Interim Director of Fiber Development, Bolt Threads, Inc., Emeryville, CA

2014-2016 Senior Research Engineer, Center for Applied Energy Research, University of Kentucky

2011-2014 Engineer Associate II, Center for Applied Energy Research, University of Kentucky

PUBLICATIONS

1. **Morris, E.A.**, R. Sarabia-Riquelme, N. Hochstrasser, J. Burgess, A.E. Oberlink, D.L. Eaton, and M.C. Weisenberger, *Early development of multifilament polyacrylonitrile-derived structural hollow carbon fibers from a segmented arc spinneret.* Carbon, 2021. **178**: p. 223-232.
2. Salim, N.V., S.E. Edrington, **E.A. Morris**, and M.C. Weisenberger, *Analyses of closed porosity of carbon fiber precursors using a robust thermoporosimetric method.* Polymer Testing, 2018. **67**: p. 151-158.
3. Sarabia-Riquelme, R., J. Craddock, **E.A. Morris**, D. Eaton, R. Andrews, J. Anthony, and M.C. Weisenberger, *Simple, low-cost, water-processable n -type thermoelectric composite films from multiwall carbon nanotubes in polyvinylpyrrolidone.* Synthetic Metals, 2017. **225**: p. 86-92.
4. **Morris, E.A**., M.C. Weisenberger, M.G. Abdallah, F. Vautard, H. Grappe, S. Ozcan, F.L. Paulauskas, C. Eberle, D. Jackson, S.J. Mecham, and A.K. Naskar, *High performance carbon fibers from very high molecular weight polyacrylonitrile precursors.* Carbon, 2016. 101: p. 245-252.

5. **Morris, E.A.**, M.C. Weisenberger, and G.W. Rice, *Properties of PAN fibers solution spun into a chilled coagulation bath at high solvent compositions.* Fibers, 2015. **3**(4): p. 560-574.
6. **Morris, E.A.**, M.C. Weisenberger, S.B. Bradley, M.G. Abdallah, S.J. Mecham, P. Pisipati, and J.E. McGrath, *Synthesis, spinning, and properties of very high molecular weight poly(acrylonitrile-co-methyl acrylate) for high performance precursors for carbon fiber.* Polymer, 2014. 55(25): p. 6471-6482.

BOOK CHAPTERS

1. **Morris, E.A.** and M.C. Weisenberger, *Solution Spinning of PAN-Based Polymers for Carbon Fiber Precursors*, in *Polymer Precursor-Derived Carbon*, A.K. Naskar and W.P. Hoffman, Editors. 2014, ACS Books. p. 189-213.

PATENT APPLICATIONS

1. **Morris, E.A.**, Weisenberger, M.C., Rantell, T., Abdallah, M. Method for Hybrid Dry-Jet Gel Spinning and Fiber Produced by that Method. US Patent Application No. 13/653877 filed on Oct. 17, 2012.